



**MONASH** University

**Understanding Orographic Precipitation across the Australian  
Snowy Mountains**

by

Fahimeh Sarmadi

A Dissertation Submitted in Fulfilment of the

Requirements for the Degree of

DOCTOR OF PHILOSOPHY

School of Earth, Atmosphere and Environment

Monash University, Victoria, Australia

June 2018

## **Copyright notice**

© Fahimeh Sarmadi 2017

*I certify that I have made all reasonable efforts to secure copyright permissions for third-party content included in this thesis and have not knowingly added copyright content to my work without the owner's permission.*

# Abstract

*This thesis presents analyses of the historic wintertime (May-October) precipitation obtained from seven high-elevation gauges across the Snowy Mountains for a 21-yr period from 1995 to 2015. The Snowy Mountains, with peaks in excess of 2000m, are the tallest mountains in the Australian Alps and feed some of the major river systems of the Murray-Darling Basin. The frequency of rainy days ( $>0.25$  mm) is seen to follow a seasonal cycle with peaks being present in July and August. There is also a negative trend in the wintertime precipitation amount, with the value of  $-22.69$  mm yr<sup>-1</sup>, amounting to 476 mm over the analysis period.*

*A K-means clustering algorithm was employed to classify the daily meteorology. Cluster analysis of six synoptic indicators and the low-level stability (as measured non-dimensional mountain height  $\hat{H}^2$ ) from the nearest upwind sounding site of the BoM to the Snowy Mountains (Wagga Wagga) has identified four synoptic classes associated with precipitation in the Snowy Mountains during the cold seasons. The first cluster, C1, is the wettest cluster containing the majority of the heavy precipitation days, while the last cluster, C4, is the driest cluster containing the majority of the low precipitation days. The mean values of  $\hat{H}^2$  for the four clusters are increasing from C1 to C4, where higher values of  $\hat{H}^2$  indicate stronger blocking and, accordingly, less orographic precipitation. A deeper analysis of these data found that the relationship was primarily driven by extreme values with very large values of  $\hat{H}^2$  ( $>7.8$ ) being associated with suppressed rainfall and very heavy rainfalls ( $>28$  mm day<sup>-1</sup>) being associated with low values of  $\hat{H}^2$ . The frequency of rainy days and unblocked days ( $\hat{H}^2 < 1$ ) are decreasing from C1 to C4. These results, along with physical interpretation of composite maps for each synoptic indicator obtained from the ERA-Interim reanalysis dataset, show that each of the four clusters represents specific synoptic types. C1 was associated with frontal passages. C2 was also a wet cluster, being associated with post-frontal conditions. C3 and C4 were associated with suppressed (stable) conditions and being under the influence of anticyclone systems.*

*Building on these historical relationships, model output statistics (MOS) from a moderate resolution (12-km spatial resolution) operational forecast were used to develop stepwise regression models designed to improve the 24-h forecast of precipitation over the Snowy*

*Mountains. A single regression model for all days was found to reduce the RMSE by 7% and the bias by 75%. A class-based regression model was found to reduce the overall RMSE by 30% and the bias by 85%.*

*High-resolution numerical simulations with the WRF model have been used to better understand a typical wintertime storm associated with a cold frontal passage and its sensitivity to the dynamical and microphysical processes using weather station data and satellite observations in the Snowy Mountains. It is found that the maximum precipitation decreases, up to 70% over the mountains, leading to a reduction of about 27% on average, by reducing the elevation above 1000 m by 75%. Changing the microphysics schemes from the Thompson semi-double-moment 6-class scheme to the single-moment 5-class scheme (WSM5) leads to a change of spatial distribution of precipitation with a reduction of precipitation over the mountain peaks and enhanced precipitation over the windward and lee slopes. The domain-averaged precipitation accumulation is less sensitive to the choice of microphysics (about 6% increase) compared with its clear impact on the precipitation pattern. Orographic precipitation, however, shows much less sensitivity (only a slight reduction of about 4% in the area-average of the accumulated precipitation) to upscaling the horizontal resolution of the topography (1 km grid spacing replaced with 3 km).*

## **Declaration**

This thesis contains no material which has been accepted for the award of any other degree or diploma at any university or equivalent institution and that, to the best of my knowledge and belief, this thesis contains no material previously published or written by another person, except where due reference is made in the text of the thesis.

Signature:



Print Name: Fahimeh Sarmadi

Date: 28/06/2018

## Publications during enrolment

**Sarmadi, F.**, Huang, Y., Siems, S. T., Manton, M. J., 2017: Characteristics of wintertime daily precipitation over the Australian Snowy Mountains. *J. Hydrometeoro.*, 18, 2849-2867. DOI: 10.1175/JHM-D-17-0072.1

## Thesis including published works declaration

I hereby declare that this thesis contains no material which has been accepted for the award of any other degree or diploma at any university or equivalent institution and that, to the best of my knowledge and belief, this thesis contains no material previously published or written by another person, except where due reference is made in the text of the thesis.

This thesis includes 1 original papers published in peer reviewed journals. The core theme of the thesis is understanding the dynamical and microphysical processes of orographic enhancement over the Snowy Mountains of southeastern Australia. The ideas, development and writing up of all the papers in the thesis were the principal responsibility of myself, the student, working within the Monash University under the supervision of Steven Siems.

The inclusion of co-authors reflects the fact that the work came from active collaboration between researchers and acknowledges input into team-based research.

In the case of Chapter 2, 3, 4 and 5 my contribution to the work involved the following:

2,3	Characteristics of wintertime daily precipitation over the Australian Snowy Mountains	Published	70%. Concept and collecting data and writing first draft	1)Steven Seims 2)Yi Huang 3)Michael Manton	No

I have renumbered sections of submitted or published papers in order to generate a consistent presentation within the thesis.

**Student signature:**



**Date:** 28/06/2018

The undersigned hereby certify that the above declaration correctly reflects the nature and extent of the student's and co-authors' contributions to this work. In instances where I am not the responsible author I have consulted with the responsible author to agree on the respective contributions of the authors.

**Main Supervisor signature:**



**Date:** 28/06/2018

## **Acknowledgements**

*First and foremost, I would like to thank my main supervisor, Steven Siems, for his guidance and patience, and for being a most excellent supervisor. Thanks also go to my co-supervisors Michael Manton and Yi Huang who have also supported me and guided this project. This thesis certainly wouldn't have been possible without their insightful comments and suggestions along the way.*

*This thesis was dependent on the data sets that were generously provided by Snowy Hydro Ltd. I especially want to thank Thomas Chubb for his technical supports. Thanks also go to the Bureau of Meteorology for providing the ACCESS-R forecasts.*

*Thanks also go to my friends and colleagues here at Monash University for both the social and technical support.*

*I wish to deeply thank my family. Without your guidance, motivation and emotional support over the years, this would not have been possible.*

*And finally, mostly of all, my best friend and life partner, Mo. Thank you for your constant encouragement and belief in me. This thesis is dedicated to you.*

## Contents

<b>Abstract .....</b>	<b>iii</b>
<b>Declaration .....</b>	<b>v</b>
<b>Publications during enrolment .....</b>	<b>vi</b>
<b>Acknowledgements .....</b>	<b>viii</b>
<b>Contents.....</b>	<b>ix</b>
<b>List of Figures .....</b>	<b>xii</b>
<b>List of Tables.....</b>	<b>xvii</b>
<b>Table of abbreviations.....</b>	<b>xix</b>
<b>Chapter 1 .....</b>	<b>1</b>
1.1 Climatology .....	3
1.2 Synoptic Meteorology of Wintertime Precipitation in southeast Australia.....	6
1.3 Orographic Clouds and Precipitation .....	7
1.3.1 Dynamics over the Snowy Mountains:.....	9
1.3.2 Microphysical Structures of cold Cloud over the Snowy Mountains.....	9
1.4 State of the Art Research on Orographic Precipitation .....	11
1.4.1 Numerical Simulations .....	11
1.4.2 Statistical Approaches: .....	13
1.5 Summary of Aims of the Thesis .....	14
<b>Chapter 2.....</b>	<b>16</b>
2.1 Introduction .....	17
2.2 Winter precipitation characteristics .....	18
2.3 Datasets: .....	26
2.3.1 Ground-based wintertime precipitation dataset.....	26

2.3.2	Wagga Wagga sounding dataset.....	27
2.3.3	ERA-Interim reanalysis dataset.....	29
2.4	Methodology of cluster analysis.....	30
2.5	Results of synoptic classification .....	31
2.5.1	Classification using six indicators .....	31
2.5.2	Temporal variability of synoptic classes using six indicators .....	34
2.5.3	Classification using seven indicators.....	36
2.5.4	Synoptic conditions associated with each class.....	38
2.6	Conclusion:.....	45
<b>Chapter 3.....</b>		<b>47</b>
3.1	Introduction .....	48
3.2	Datasets: .....	49
3.3	Winter precipitation characteristics .....	50
3.4	Methodology of cluster analysis.....	51
3.5.	Relationships between independent variables and observed precipitation.....	52
3.6.	Results of Daily winter precipitation forecasting.....	57
3.6.1	Precipitation estimations by ACCESS-R .....	57
3.6.2	MODEL 1: SINGLE REGRESSION MODEL.....	59
3.6.3	Model-2: Cluster-based regression model.....	61
3.7	Conclusion:.....	63
<b>Chapter 4.....</b>		<b>65</b>
4.1	Introduction .....	66
4.2	Datasets: .....	67
4.2.1	High density ground-based observation: .....	67
4.2.2	Satellite imagery .....	68
4.3	The meteorological conditions of the case study .....	68
4.4	Model configuration .....	70

4.5	Sensitivity studies .....	73
4.5.1	Microphysics run (MP).....	73
4.5.2	Topography run (TOPO) .....	73
4.5.3	Resolution run (RES) .....	74
4.6	Evaluation of Control Run.....	75
4.6.1	Upper Air Profile .....	75
4.6.2	Surface Precipitation and Temperature Evaluation:.....	77
4.7	Sensitivity Study:.....	81
4.8	Summary and Conclusion.....	95
<b>Chapter 5</b>	.....	<b>98</b>
5.1	A climatology of wintertime precipitation over the Australian Snowy Mountains	99
5.2	Adjustment to the ACCESS_R forecast of daily wintertime precipitation over the Australian Snowy Mountains .....	101
5.3	Sensitivity Analysis of orographic precipitation using WRF Model .....	102
5.4	Future directions .....	104
<b>References</b>	.....	<b>106</b>

## List of Figures

Figure 1.1 Australian map of topography (color shaded), showing the Murray-Darling Basin (hatched area). .....	2
Figure 1.2 Rainfall decile at the peak of the Millennium Drought (2001 to 2009).....	4
Figure 1.1 Schematic representation of the dominant Australian climate influences_ .....	6
Figure 2.1 May–Oct total monthly precipitation for the period 1995–2015 (top plot). May–Oct total precipitation in the high elevations of the Snowy Mountains. The linear fit has slope of $-22.69 \text{ mm yr}^{-1}$ (bottom plot). .....	19
Figure 2.2 May-Oct cycle of monthly mean intensity (hPa) and subtropical ridge position ( $^{\circ}\text{S}$ ) for the long-term 1890–2015 climatology (blue curve) with its six month average (blue dot) and for the period 1995-2015 (red curve) with its six month average (red diamond).....	20
Figure 2.3 Time series of monthly-mean precipitation in the Snowy Mountains (blue barbs), with time series (red line) of climate drivers (top) STR_I, (middle) STR_P and (bottom) Atmospheric blocking Index (ABI). .....	24
Figure 2.4 Time series of monthly-mean precipitation in the Snowy Mountains (blue barbs), with time series (red line) of climate drivers (top) IOD, (middle) SOI and (bottom) SAM. ....	25
Figure 2.5 a) Map of the Snowy Mountains analysis region (red box) in southeastern Australia showing the closest upper-wind site of the BoM to the Snowy Mountains (Wagga Wagga). b) Location of the seven alpine rain gauges used in this study.....	26
Figure 2.6 Probability distribution of daily winter rainfall over the period 1995-2015 based on six large-scale synoptic indicators. ....	31
Figure 2.7 Probability distribution of $\hat{H}^2$ for next 24 hours after sounding measurements over the period 1995-2015 based on six large-scale synoptic indicators. ....	32

Figure 2.8 Box plot of synoptic indicators for four clusters with outliers removed. Upper and lower whiskers calculated based on the quartile method. ....	34
Figure 2.9 Seasonal variability of synoptic classes during 1995-2015. ....	35
Figure 2.10 Interannual variability of synoptic classes during 1995-2015 .....	35
Figure 2.11 Cumulative distribution of precipitation (right) and $\hat{H}^2$ (left) for next 24 hours after sounding measurements over the period 1995-2015 based on seven large-scale synoptic indicators. ....	36
Figure 2.12 a-d) Distribution of $\hat{H}^2$ for each cluster, e) stacked histograms of $\hat{H}^2$ variable for different clusters, f) the $\hat{H}^2$ distribution for No-Rain days and Rain days.....	38
Figure 2.13 Upper-air sounding at Wagga Wagga weather station and MSLP chart for the days closest to the center of each class.....	40
Figure 2.14 Composite charts of MSLP in hPa (Top) and TW in <i>hPa.s2m</i> (bottom), showing total moisture up to 250-hPa, for the four classes.....	42
Figure 2.15 As in Figure 2.14, but showing QV and QU (westerly and southerly moisture flux up to 250-hPa) for the four classes.....	43
Figure 2.16 As in Figure 2.14, but showing total totals index (TT) in °C and root-mean-square wind shear between 850 and 500 hPa (SH) in 1/s. ....	44
Figure 3.1 ACCESS system APS1 configuration.....	50
Figure 3.2. A) Histogram and scatter plot of precipitation and $\hat{H}^2$ , B & C) the marginal CDF distributions of precipitation and $\hat{H}^2$ . D) Joint frequency using the Frank PDF copula. ....	56
Figure 3.3. Histograms of goodness-of-fit criteria (RMSE, $r^2$ , and Bias) based on normalized values for Model-2_C1 derived from cross-validations with 10000 simulations.. ....	63

Figure 4.1 Mean Sea-Level Pressure (MSLP) analyses for May case at (a) 12 UTC 8th, (b) 00 UTC 9th, (c) 12 UTC 9th and (d) 00 UTC 10<sup>th</sup>. Himawari-8 true color imagery for (e) 00 UTC on 9th and (f) 10th May 2016 are presented at the bottom ..... 70

Figure 4.2 (Top) Topography map of Australia (color shaded) and the WRF three nested domains (red boxes) used in this study. (Bottom) Zoomed-in view of the two inner domains with the location of two alpine rain gauges (Cabramurra and Guthega Dam).. ..... 72

Figure 4.3 The model topography map (CTRL-run, left), the reduced-mountain topography map (TOPO-run, Middle) where rise above 1 km is reduced by 75%, and the upscaled topography map (RES-run, right) where the orography of d02 (3 km) replaces that d03 (1 km).. ..... 74

Figure 4.4 Comparison of the observed upper air soundings from the Wagga Wagga weather station (black lines) alongside 1 km WRF simulations from the nearest grid point to Wagga Wagga station (red lines) on 9 of May, 2016 at 00:00 UTC (a) and 11 of May, 2016 at 00:00 UTC (b). ..... 76

Figure 4.5 Time series of the observed surface accumulated precipitation (top panels, solid blue lines), 2-m temperature (bottom panels, solid blue lines) measurements of Cabramurra and Guthega Dam with the WRF d01 (9 km, dashed red lines), d02 (3 km, dotted brown lines) and d03 (1 km, solid green lines) outputs from the nearest grid point to the sites. ... 78

Figure 4.6 The 69-hr accumulated simulated precipitation amounts (in mm) from 1km resolution with CTRL-run (Thompson MP), overlaid with the model topography (black contours from 400 to 2400 m by 250m-interval). ..... 79

Figure 4.7 A Taylor diagram based on the 69-hr precipitation at the 51 stations for d01 (black circle), d02 (black square), d03 (black diamond) CTRL-run simulations, along with the observations marked as a star for reference. The TOPO-run, MP-run and RES-run from the 1 km simulations marked as blue, brown and green diamonds. .... 80

Figure 4.8 (a) Comparison of total accumulated observed and simulated precipitation averaged at all SHL rain gauge sites. (b) Boxplots of the total observed and simulated accumulated precipitation at the rain gauge sites for a 69-hour period. Time series of the

observed surface accumulated precipitation measurements of (c) an upwind site of Pinnacle Mountain and (d) and a downwind site of Island bend. ....	82
Figure 4.9 The 69-hr accumulated simulated precipitation amounts from 1km resolution with (a) CTRL-run (Thompson MP) (b) MP-run (WSM5 MP) c) TOPO-run, and (d) RES-run, overlaid with the model topography (black contours from 400 to 2400 m by 250m-interval).....	84
Figure 4.10 Differences in accumulated precipitation (mm, shaded) overlaid with the model topography (black contours from 800 to 2200 m by 400m-interval), between the WRF 1-km for a 69-hour period (0009 UTC 8 May to 0006 UTC 11 May 2016) for (a) CTRL-MP run; (b) CTRL-TOPO run; (c) CTRL-RES run. The maximum and domain-averaged precipitation differences are shown on top of the individual panels. Bottom panels show the ratio of the precipitation amounts from the CTRL-run to that from (d) MP-run, (e) TOPO-run and (f) RES-run. ....	86
Figure 4.11 Time-distance diagrams showing half-hourly precipitation for (a) CTRL-run and differences rates in mm for a 72-hour period (0006 UTC 8 May to 0006 UTC 11 May 2016) through latitude 36.4°S for (b) CTRL-MP run; (c) CTRL-TOPO run; (d) CTRL-RES run. The vertical cross-sections are taken at a time during the post-frontal period, as indicated inside the red box.....	87
Figure 4.12 Vertical cross-sections of the simulated (a) liquid (shaded) with rain (red lines with 0.3 g/kg interval), (b) with small ice particles (shaded) with total big ice hydrometeors (red line with 0.3 g/kg interval) for (a-b) CTRL-run, (c-d) MP-run, and (e-f) TOPO-run through latitude 36.4°S at 18:30 UTC, overlaid with the simulated temperatures (left panels, green contours, thick line indicates freezing level with 5°C interval), potential temperature (right panels, orange contours with 5°C interval) and wind vectors (20vertical wind ×N-S wind).....	90
Figure 4.13 Cloud top temperature (left panels) and cloud top phase (right panels) from Himawari-8 (a-b) at 1740UTC 9 May 2016, CTRL-run (c-d) and MP-run (e-f) at 1830UTC 9 May 2016.....	92

Figure 4.14 Histograms showing the relative frequencies of CTP decomposed into 5°C temperature bins. Top plots: The observation from Himawarri-8 at 1740 UTC 9 May 2016 (left), CTRL-run (middle) and MP-run (right) at 1830UTC 9 May 2016. The simulated cloud top is defined at 0.5 cloud optical thickness from the top of the model domain. Bottom plots: same a top plots, showing the relative frequencies of CTP but over a period of 69 hours. 94

## List of Tables

Table 2.1 Main statistical characteristics of daily winter precipitation in mm for rainy days .....	19
Table 2.2 The Pearson correlation coefficients of monthly winter precipitation and large-scale drivers of rainfall across the Snowy over the period 1995-2015.....	22
Table 2.3 Cross-correlation coefficients between six large-scale drivers of rainfall across the Snowy over the period 1995-2015. Statistical significant at the 0.01 confidence level.....	23
Table 2.4 Properties of precipitation gauges sites at high altitudes in the Snowy Mountains. The mean winter precipitation values are calculated over the period 1995-2015. ....	27
Table 2.5 Summary of six synoptic indicators used to represent large-scale environment.	28
Table 2.6 Main statistical characteristics of daily winter rainfall and $\hat{H}^2$ across synoptic clusters based on six-variable clustering .....	32
Table 2.7 Main statistical characteristics of daily winter rainfall and $\hat{H}^2$ across synoptic clusters based on seven-variable clustering.....	37
Table 2.8 Values of seven indicators along with their daily precipitation for days closest to each cluster centroid. ....	39
Table 3.1. Main statistical characteristics of daily winter precipitation in mm for rainy days (>0.25mm) for a 2-yr period (2014-2015). Numbers shown in the brackets are the ACCESS-R results. ....	51
Table 3.2. Cross-correlation coefficients between seven synoptic indicators. *Bold numbers are significant correlation at significance level of 1%. ....	53
Table 3.3. Linear (Pearson) and Rank correlation coefficients between seven synoptic indicators and observed precipitation over the period of 1995-2015 (Classification results based on 7-variable clustering). *Bold numbers are significant correlation at significant level of 5%. No Class: no classification process has been implemented. ....	54

Table 3.4 Summary of verification scores/metrics used to evaluate the ACCESS-R forecasts in this study.....	57
Table 3.5. Performance of ACCESS-R precipitation estimation of observed precipitations over the period of 2014-15 with a value of 0.25 mm for the rain-day threshold. ....	58
Table 3.6 Leading predictors in regression equations for different models. ....	60
Table 3.7. Goodness-of-fit criteria for different models for estimating daily winter precipitations over 2014-15 based on ACCESS-R rainy days .....	62
Table 4.1 A list of configuration settings for numerical study.....	72

## Table of abbreviations

ACCESS	Australian Community Climate and Earth-System Simulator
AWAP	Australian Water Availability Project
CTP	Cloud Top Phase
CTT	Cloud Top Temperature
DMI	dipole mode index
ECMWF	European Centre for Medium Range Weather Forecasts
ETS	Equitable Threat Score
FBS	Frequency Bias Score
GP	Surface pressure at Wagga Wagga
$\hat{H}$	Non-dimensional mountain height
IOD	Indian Ocean Dipole
MODIS	Moderate Resolution Imaging Spectroradiometer
MSLP	Mean Sea Level Pressure
MOS	Model Output Statistics
NCEP–NCAR	National Centers Environmental Prediction–National Center for Atmospheric
NWP	Numerical Weather Prediction
PBL	Planetary Boundary Layer
PDF	Probability Density Function
QPF	Quantitative Precipitation Forecasts
QU	Westerly moisture flux up to 250hPa
QV	Southerly moisture flux up to 250hPa
SAM	Southern Annular Mode
SH	Root-mean-square wind shear between 850 500hPa
SHL	Snowy Hydro Ltd.
SLW	Supercooled Liquid Water
SOI	Southern Oscillation Index
SPERP	Snowy Precipitation Enhancement Research Project
STR	Subtropical Ridge
TT	Total Totals Index
TW	Total moisture up to 250hPa
UTC	Coordinated Universal Time
WRF	Weather Research/Forecasting Model
YSU	Yonsei University

# Chapter 1

## Introduction

Water is one of the world's most vital resources; over seven billion people across the planet rely on it daily. Ever increasing demands make the world leaders increasingly concerned about water scarcity and the potential of a global water crisis. Efficient drought mitigation planning and development of more effective management plans of available water resources are keys to aid water suppliers in survival under extreme conditions. Water availability and management have also become a serious challenge in Australia due to its large variability and an increasing demand with the rise in population.

The Murray-Darling Basin contains the longest river system in Australia with the large inland river basin (Figure 1.1). The basin covers 1,061,469 km<sup>2</sup> land mass (13.8% of the continent) including most of New South Wales, Victoria, and parts of Queensland and South Australia, and all of the Australian Capital Territory. This Basin is named after its two major water courses, the Murray and Darling rivers, and is mostly arid or semi-arid, with great variability in annual rainfall. It is home to over 2 million people and best known as the food bowl of Australia. This region produces around one-third of the national food supply (Pittock and Connell 2010) with an annual value exceeding A\$14 billion (Pittock and Connell 2010). The irrigated land (only 2%) uses 90% of the diverted waters. The irrigated agricultural land in the Basin produces around 70% of the continent irrigated agricultural yield, contributing AUD\$7 billion per year to the total value of Australian agricultural production (ABS et al. 2009). The critical role of the Murray-Darling Basin in the Australian economy gives rise to the higher demand for better water resources management and an in-depth investigation of the nature of wintertime precipitation, which plays a decisive role in the water cycle over the region.

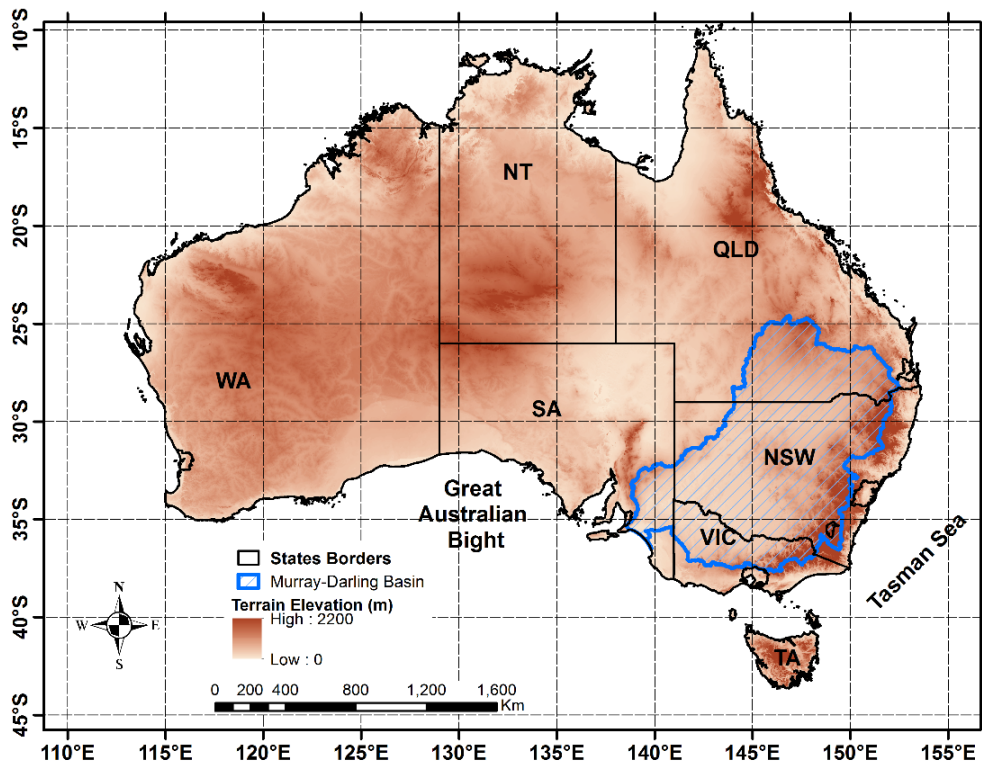


Figure 1.1 Australian map of topography (color shaded), showing the Murray-Darling Basin (hatched area).

The Australian Alps are the highest part of the continental divide along the eastern seaboard, known as the Great Dividing Range, and play a crucial role in the weather across the densely populated southeastern seaboard. The Great Dividing Range forms the headwaters of many of the major rivers in the Murray–Darling basin and underpin many unique natural ecosystems of the high mountain catchments (e.g. the Snowy, Murray and Murrumbidgee Rivers) with some of the richest biodiversity areas on the mainland. The Alpine water account for 29% of the annual average inflow yield of the Murray-Darling Basin (Worboys and Good 2011). The Snowy Mountains, with peaks in excess of 2000m, are the tallest mountains in the Australian Alps and feed some of the major river systems of the Murray-Darling Basin. Precipitation to the west and north of these Mountains naturally flows inland into the Murray and Murrumbidgee Rivers, ultimately reaching the Great Australian Bight, while precipitation to the east naturally flows into the Snowy River reaching the Tasman Sea. This water is of immediate economic value for the generation of hydroelectric power and is of further value for downstream consumption, particularly for agriculture across the

semi-arid Murray–Darling Basin. For this reason, water is routinely diverted through a series of tunnels, aqueducts, and pumps from the Snowy River basin across the divide into the inland catchments by the Snowy Mountains scheme. The construction of the scheme, the largest hydro-electric scheme in Australia consisting of 16 major dams (to better capture, store and divert the water and also improve flood resilience) and 7 power plants, began in late 1940's following a series of intense droughts in the region.

The day-to-day management of this water resource requires accurate quantitative precipitation estimates and reliable short-term quantitative precipitation forecasts (QPF) over the mountains. These QPFs have a strong impact on day-to-day decisions in governmental and business activities (e.g., agricultural operations, utility companies, snowpack-augmentation in ski resorts, transportation companies and even the efficiency of commodities markets, etc.) (Fritsch et al. 1998). Reliable QPF of hydrologic extreme events (such as flash flooding) is also central to water resources management.

The importance of the water resources over the Snowy Mountains region justified the operational and experimental winter orographic cloud seeding projects. The Snowy Precipitation Enhancement Research Project (SPERP) proposed by Snowy Hydro Limited and was initiated from May 2005 to June 2009 by dispersing silver iodide from ground-based generators and statistical analysis showed a positive impact of seeding (Manton and Warren 2011). The operation cloud seeding program offers yet another reason to study the orographic precipitation over the Snowy Mountains.

### **1.1 Climatology of southeast Australia**

Two prolonged periods of dry conditions (major droughts) were experienced in southeastern Australia (south of 33.5 °S and east of 135.5 °E) in the past 100 years. An 11-year (1935-1945) and an 13-year (1997-2009) period both had rainfall deficits of above 10%. Figure 1.2 shows that much of southwest and southeast Australia underwent below-average to record-low rainfall during the peak of the Millennium Drought, which is defined by van Dijk et al. (2013) as the period 2001–2009: the longest consecutive series of years with below median rainfall in southeast Australia since at least 1900. The Millennium drought

had a significant impact on the Australian economy and led to the largest declines in agricultural employment (about 100,000 jobs were lost) and rural exports (around 13% fall) during 2002-03 (Lu and Hedlry 2004). Nicholls (2005) reported a decreasing trend in both maximum and spring snow depth in the Snowy Mountains over a 40-year period beginning in 1962. A decline of about 10% was observed in the maximum snow depth. A much stronger decrease in spring snow depth (about 40%) was found, mostly attributed to the melting of the snow due to the strong warming during July-September.

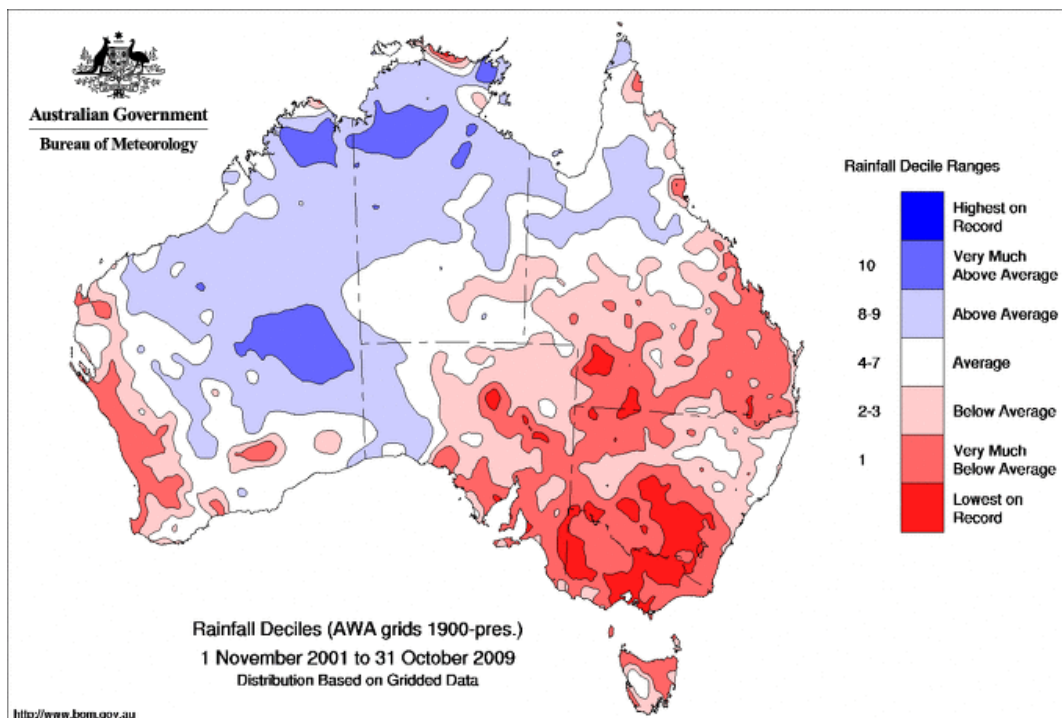


Figure 1.2 Rainfall decile at the peak of the Millennium Drought (2001 to 2009). Copyright of the Australian Bureau of Meteorology.

Australia's climate is generally driven by several large-scale atmospheric features with varying levels of spatial and temporal impact. Figure 1.3 represents the main drivers of rainfall variability in the Australian region. Previous studies suggest that precipitation in southeast Australia is generally governed by large-scale climate drivers, such as the ENSO Index (Wang and Hendon 2007), Southern Annular Mode (SAM; Meneghini et al. 2007), Indian Ocean Dipole (IOD; Saji et al. 1999), the Atmospheric Blocking Index at the location

of 140°E (Risbey et al. 2009), and the Subtropical Ridge position and intensity (Timbal and Drosowsky 2013).

Precipitation across southeast Australia has been directly related to the strength and latitude of the subtropical ridge (STR), which is defined by a belt of high pressure that encircles the globe in the middle latitudes. In Australia, the STR is positioned to the southern part of the mainland during the summer months and is often associated with stable high pressures over southern Australia. During the winter months, the STR moves northward. The strong decline in wintertime rainfall peaked during the Millennium Drought and is possibly associated with the observed trends in the STR, which has been intensifying and moving further south (Timbal and Drosowsky 2013), presumably as part of a changing climate (Williams and Stone 2008). Variations in the SAM, as another synoptic-scale regulator, appear to be linked to the variations in winter rainfall over southern Australia (Meneghini et al. 2007). The decline in cool season (April–October) rainfall has been also been linked to the positive phase of SAM, which shifted the belt of strong westerly winds poleward, whereby diminishing the mid-latitude westerly (hence cold fronts) on the western slopes of the Alps (Hendon et al. 2007). A similar relationship is also suggested by Nicholls (2010), causing a decline of about 15% over the period 1958–2007 in cool season precipitation over southeast Australia. The IOD, defined as the difference in SST anomaly between the tropical western Indian Ocean and the tropical southeastern Indian Ocean has also been shown to modulate rainfall in southeastern Australia (Ashok et al. 2003). This phenomenon is negatively correlated to rainfall in this region and tends to peak in June–October (Risbey et al. 2009). The Southern Oscillation Index (SOI), the difference between the anomalous pressures at Tahiti and Darwin, is commonly used to characterize ENSO. The negative SOI values (El Nino conditions) are found to generally decline the mean rainfall in this region in the winter and spring months (Murphy and Timbal 2008; Nicholls 2010).

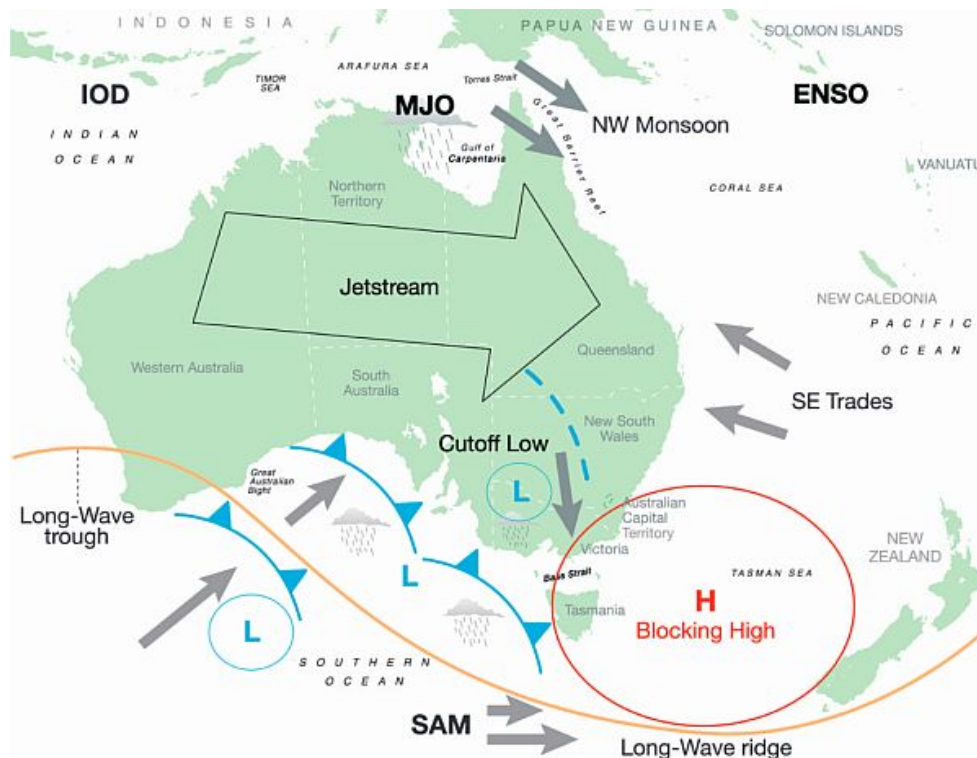


Figure 1.3 Schematic representation of the dominant Australian climate influences. SOURCE: Risbey et al 2008

## 1.2 Synoptic Meteorology of Wintertime Precipitation in southeast Australia

The Australian Alpine water resource has experienced a decline in high-elevation wintertime precipitation in excess of the general decline in southeastern Australia during 1990–2009 (Chubb et al. 2011; Fiddes et al. 2015). This decline was stronger to the west of the divide and in the high elevations. This decline has driven interest into understanding the cool-season synoptic circulation and the broader meteorology that underpins it. Different synoptic classifications of wintertime precipitation in this region have been developed, suggesting that this precipitation is mostly sourced from mid-latitude, cyclonic large-scale weather systems (cutoff and embedded lows) and their associated westerly cold fronts and to a lesser extent from cloudbands stretching from northwestern Australia (Pook et al. 2006; Landvogt et al. 2008; Risbey et al. 2009; Chubb et al. 2011; Dai et al. 2014; Murphy and Timbal 2008). Chubb et al. (2011) also discussed a northern moisture corridor from the coast of Queensland accounts for heavy precipitation events. Cutoff lows are isolated low pressure systems which have detached from the midlatitude westerly airstream (Low centred between longitudes

135°E-150°E, and north of 45°S). A climatology of daily wintertime precipitation has been categorized into distinct three and five synoptic types based on different methods and variables. The cool-season synoptic circulation (June–September, 1971-1982) over the state of Victoria has been classified into five major synoptic types (interacting and non-interacting fronts, cold and warm cyclonic lows, and post-frontal) by Wright (1989). Later, Landvogt et al. (2008) categorized daily precipitation over northeast Victoria into three synoptic classes (prefrontal, postfrontal, and cutoff). Pook et al. (2006) documented three different synoptic weather types (cutoff lows, Cold-frontal systems, and others) associated with daily rainfall throughout the growing season (April–October, 1970–2002) in Western Victoria. They found that about half of precipitation cutoff lows found to contribute to at least 50% of all precipitation. Synoptic weather systems are the dominant mechanisms responsible to force moist air parcels to ascend and eventually generate precipitation, particularly during the cold seasons in the mid-latitudes. Chubb et al. (2011) performed a synoptic decomposition of wintertime precipitation (a 20-yr period beginning in 1990) over the Snowy Mountains region. This analysis found that cutoff lows (with and without fronts) are responsible for 57% of total precipitation and 79% of precipitation were associated with the passage of a cold front over the region. They also performed a back-trajectory analysis and found two dominant moisture corridors, arriving from the west-northwest and northeast, responsible for heavy precipitation events across this region. Dai et al. (2014) defined four distinct synoptic regimes as observed by the physical soundings from the Wagga Wagga station that is the nearest radiosonde site to the Snowy Mountains during the cold seasons. Their wettest regime, the least frequent one (only 10%), made up 40% of winter precipitation and was associated with a frontal passage with a dominant north-westerly flow which brought deep moisture fluxes. In contrast, the driest regime was under the influence of high-pressure systems and responsible for only 5% of total wintertime precipitation.

### **1.3 Orographic Clouds and Precipitation**

Apart from the nature of storms, precipitation is commonly influenced by surface orography. The orographic influences on precipitation are clearly visible when a pre-existing weather disturbance moves into alpine areas. Precipitation is commonly amplified (reduced) on the windward slopes (lee-side) with elevation, leading to strong gradients in alpine regions (Roe 2005). Orographic precipitation, commonly defined as precipitation arising from the lifting

of moist air in response to the presence of mountains, is known to be sensitive to small variations in ambient conditions, the evolution of the moisture fields, and the geometry of the barrier (e.g. Smith 1989; Colle 2004; Watson and Lane 2014). The impact of orography on precipitation intensity and distribution has been widely studied. Smith (1979) reviewed the complex interaction between precipitation and the terrain, noting the differences in orographic precipitation mechanisms over small hills and mountains as well as the distribution of moisture and static stability in the lower atmosphere.

From a dynamical viewpoint, the precipitation distribution is found to be sensitive to a variety of parameters. Sinclair et al. (1997) noted enhanced spillover effect is linked to strong wind speed and low static stability, temperature, and freezing level. The response of the approaching airflow to a barrier can be determined by the ratio of a buoyancy force to fluid's inertia, commonly referred to as the nondimensional mountain height ( $\hat{H}$ ) (Pierrehumbert and Wyman 1985; Baines 1987). Smith (1989) developed a regime diagram for hydrostatic flow over a mountain to illustrate the stagnation onset as a function of the spanwise-to-streamwise horizontal aspect ratio of the topography and  $\hat{H}$ . Two common scenarios are defined by the value of  $\hat{H}$ : blocked and unblocked. In a blocked scenario (i.e. large nondimensional mountain height) the approaching airflow is unable to ascend over the terrain and is dammed or diverted laterally around the barrier. Such blocking mechanisms can have an impact on both convective storms and frontal systems. In contrast, in an unblocked scenario (i.e. small nondimensional mountain height) the oncoming airflow has enough kinetic energy to rise over the terrain (Durran 1990; Hughes et al. 2009). An unblocked scenario is commonly featured by heavier precipitation events as a consequence of getting more uplift which cools the air to saturation, leading to water vapour condensation and ultimately precipitation. (e.g., Colle 2004; Wang et al. 2016). This effect is also captured in a study over the Australian Snowy Mountain region by Huang et al. (2018), where the less frequent unblocked scenario (31% of the time for the two year, 2014–2015; May–September), contributed 50–70% of the relative precipitation to the total amount over the high elevations (>1400 m).

Twelve different mechanisms of orographic effects on precipitation are detailed by Houze (2012), ranging from the dynamics (e.g. blocking) to thermodynamics (e.g. diurnal heating driven convection), to microphysics (e.g. a seeder-feeder mechanism). Misrepresentation of

these various mechanisms in the model by which precipitation forms in mountainous regions may give rise to errors in precipitation forecast (Jiang 2003; Richard et al. 2007; Huang et al. 2018).

### **1.3.1 Dynamics over the Snowy Mountains:**

Much of the interest in precipitation and clouds across the Snowy Mountains has focused on the climatology, but relatively little has focused on the actual dynamic processes of orographic enhancement in comparison to other mountainous regions in the US (e.g. Stoelinga et al. 2003; Liu et al. 2011), and Europe (e.g. Panziera 2010; Smith et al. 2015). Chubb et al. (2011) found that the precipitation over the Great Dividing Range was at least a factor of four times that for the upwind plains of western Victoria in wintertime. Watson and Lane (2012, 2014) investigated the underlying dynamics of the important orographic precipitation events in the Australian Alps to examine the influence of ridge geometry (straight, concave and convex ridge) along with upstream thermodynamic and wind conditions variations. They showed that the distribution of precipitation is strongly influenced by the shape of the mountain ranges and environmental parameters (especially the Froude number) in idealized conditions. Chubb et al. (2012) detailed two typical wintertime precipitation events featured by a strongly dynamic cut-off low and a weaker, less well-organised system with a complex of frontal bands over the Brindabella Ranges. The Brindabella Ranges are located on the western border of New South Wales and the Australian Capital Territory and the north east of the Snowy Mountains, where a clear orographic signal was detected. In both case studies, orographic precipitation was observed over the 24-h period after the frontal passage and found to have SLW. More in-depth research is needed to better resolve the interactions between the orography and the flow associated with the passage of winter fronts.

### **1.3.2 Microphysical Structures of cold Cloud over the Snowy Mountains**

A saturated air parcel will not necessarily glaciate when the temperature drops below freezing. Cloud droplets that remain as liquid even at temperature below 0°C are called “supercooled liquid water”. One of the unique factors of wintertime precipitation across the Snowy Mountains is the common occurrence of clouds composed of supercooled liquid

water (SLW) (Morrison et al. 2013; Osburn et al. 2016). This unique environment of this region, distinguishes itself from other mountainous regions of the world such as the Sierra Nevada in the western United States (Morrison et al. 2013) in terms of the associated microphysical processes, the precipitation type and efficiency.

Osburn et al. (2016) reported a high frequency of occurrence of SLW (53% of the time between April and September) over the Snowy Mountains from a surface-based radiometer located on the upwind slope (Cabramurra, 1480 m). These observations were qualitatively consistent with those from the Moderate Resolution Imaging Spectroradiometer (MODIS) satellite product (both Aqua and Terra).

Ice crystal formation can occur through both homogeneous nucleation (the phase change occurs spontaneously from a pure water droplet in the absence of nuclei) and heterogeneous nucleation (the phase change requires an ice nucleus). For homogeneous nucleation to occur a drop with a radius of  $1\mu\text{m}$  ( $100\mu\text{m}$ ) requires a temperature of  $-41^\circ\text{C}$  ( $-35^\circ\text{C}$ ) (Pruppacher and Klett 1997), which indicates that this process commonly occurs in high clouds in which some SLW exist. Heterogeneous ice nucleation processes take place at much warmer temperatures (between  $-40$  and  $0^\circ\text{C}$ ) through four distinct modes of ice formation (deposition, condensation freezing, contact freezing and immersion freezing).

As ice nuclei are scarce (several orders of magnitude less abundant than cloud condensation nuclei), a secondary process can amplify the amount of precipitation. For example, after ice crystal formation, ice multiplication can happen through the Hallett–Mossop process as a secondary ice production during riming in the range of temperature  $-3^\circ$  to  $-8^\circ\text{C}$  (Mossop and Hallett 1974). Rogers and Vali (1987) showed that ice crystals may also be generated from interaction with snow-covered terrain in clouds composed of supercooled liquid water. They found over 100 times higher ice crystal concentration at the surface than the main body of the clouds in the range of temperature  $-5^\circ$  to  $-23^\circ\text{C}$ .

The unstable composition of supercooled clouds initiates the rapid phase change to mixed or ice crystal clouds. In mixed-phase clouds SLW interacts with ice crystals and as a result, ice crystals grow while SLW droplets shrink. This preferential growth of ice crystals in the expense of SLW droplets is called Wegner-Bergeron-Findeisen process (Bergeron, 1935; Findeisen, 1938), which has been suggested to tend to be faster in higher concentration of

ice particles. Cloud thermodynamic phase has an immediate impact on the microphysical processes (Pruppacher and Klett 1997) and the precipitation type and efficiency (e.g. Storelvmo et al. 2011), where smaller water droplets in liquid-phase clouds could have delayed freezing process, leading to longer cloud lifetime and lower precipitation rates, compared to ice clouds (Rauber and Grant 1987).

#### **1.4 State of the Art Research on Orographic Precipitation**

Objective forecasting method is typically carried out using either numerical or statistical solution techniques (Glahn and Lowry 1972). Numerical methods that are much more computationally demanding might have their own limitations. The possible inherent limitations of numerical methods in representing some variables have led scientists to employ some combination of both approaches in practical forecasting to reach a better result (e.g. Garric et al. 2002; Dai et al. 2014).

##### **1.4.1 Numerical Simulations**

Forecasting orographic precipitation with a numerical weather prediction (NWP) model remains challenging due not only to the difficulties of representing the variety of complex physical mechanisms but also to the limited resolution of a simulation to resolve the complex surface geometry (e.g., Panziera 2010). Despite the significant progress in the implementation of increasingly sophisticated numerical models, it continues to be a challenge. These forecasts are vital for extreme weather event prediction and hydrological applications (e.g. Dai et al. 2014; Fritsch et al. 1998).

The evaluation of precipitation forecasts is a further challenge given the high spatial variability of precipitation across a complex terrain and the limited number of surface sites available that can be used to rigorously evaluate the simulations. The Murray River catchment and the Snowy River catchment received an estimated 18% (419 GL) and 9% (146 GL) less precipitation in the Australian Water Availability Project (AWAP, Jones et al. 2009) analyses than in a Barnes successive correction scheme (Koch et al. 1983), respectively, (Chubb et al. 2016) based on an independent network of high-elevation surface sites. Chubb et al. (2015) showed that Bureau of Meteorology (BoM) underestimates the winter precipitation in high elevations by 15% due to the lack of heated tipping-bucket

gauges and wind fences. Recently, Huang et al. (2018) evaluated the estimation-forecast skill of Australian Community Climate and Earth-System Simulator (ACCESS) over the region of interest (2014-15), using the high-density precipitation gauge network of Chubb et al. (2016). They showed that the main shortcomings of the model are likely rooted in misrepresenting the fine-resolution dynamics and microphysical processes in the large-scale precipitation parameterization.

Over the past decade, there has been a sharp improvement in the understanding of orographic precipitation and physical/dynamical processes in atmospheric models. Progress has been made through the application of higher resolution mesoscale NWP and selection of subgrid parameterizations (e.g., cloud microphysics, land surface models, planetary boundary layer (PBL), and radiation transfer schemes), and as a consequence, more accurate and reliable quantitative precipitation estimates and forecasts have been demonstrated (e.g., Hong et al. 2004; Thompson et al. 2008; Morrison et al. 2009; Liu et al. 2011; Rasmussen et al. 2011; Huang et al. 2014; Morrison and Milbrandt 2015).

Microphysical processes that are not fully resolved in most of the NWP models continue to be a bottleneck issue. Spectral (bin) microphysics models predict particle size distributions explicitly and therefore provide more comprehensive solutions, but they are much too expensive for operational use. Bulk microphysical parameterizations are less computationally demanding, but they represent particle size distributions of a given hydrometeor class with an empirical function. Bin schemes make no prior assumption about the shape of the particle size distribution but are computationally expensive. Due to the inherent limitations, detailed in situ observations are often required to rigorously evaluate the microphysical parameterizations and to better understand the orographic processes. Further, an accurate representation of processes in SLW favorable environments, such as the Snowy Mountains, in NWP models remains challenging. In response to this need, a number of field campaigns designed to better understand mesoscale orographic flows over complex terrain (e.g. Stoelinga et al. 2003; Woods et al. 2005) provide a basis for evaluating the widely used bulk microphysical parameterizations and to reduce the uncertainties and deficiencies related to the complexity of orographic precipitation.

Several studies have documented the sensitivity of simulated orographic precipitation to model horizontal resolution (e.g. Colle and Mass 2000; Grubišić et al. 2005; Colle et al.

2005; Rasmussen et al. 2011; Smith et al. 2015; Pontoppidan et al. 2017). It is found that finer horizontal resolution orography generally improves model skill until the orographic features are satisfactorily resolved. Any further increase in horizontal resolution does not necessarily cause major additional enhancement in model skill; however, this sensitivity is also subject to the detailed orography characteristics of the area being studied. These findings suggest that the fine model resolution alone is not adequate to acquire skillful simulations of topographic precipitation.

#### **1.4.2 Statistical Approaches:**

Statistical approaches are widely used to improve aspects of NWP forecasts, which are far more computationally demanding. Two types of classical statistical methods can generally be utilized to either estimate of parameters or improve the NWP outputs: the Perfect Prog (Klein et al. 1959) and Model Output Statistics (MOS). The perfect prognosis (“perfect prog”) approach is a simultaneous statistical relationship built between observed atmospheric variables and observations of the predictand without NWP information (Klein et al. 1959). The predictand will be then forecast by inserting the NWP information of predictors into the built statistical relationship (Wilks 2006). The perfect prog systems take NWP model forecasts for a future atmosphere, assuming them to be perfect. Since the potential predictors used in regression equations are not always well forecasted by the NWP models, the basic assumption does not account for model biases and this is a major drawback of the perfect prog scheme. On the other hand, as the built regression in the perfect prog scheme is not dependent of the NWP information, it is not required to be updated by any changes in the NWP, which can be considered as the major advantage of this method. Following the stability of the built equations in the perfect prog scheme, Shafer and Fuelberg (2008) applied this scheme to improve forecasts of Cloud-to-ground warm-season lightning over Florida.

An alternative to the perfect prog is a MOS method, which is an objective postprocessing technique in which a statistical relationship is developed to relate a single or an ensemble NWP model output to different projections into the future (Glahn and Lowry 1972). Since the MOS equations are built with NWP information, redevelopment is required to take into account changes in the NWP model. In this method, systematic errors in the NWP and local

climatology are accounted (Brunet et al. 1988). This postprocessing method is widely used on results from a NWP model to test the potential for improving the accuracy of forecasts such as precipitation (Sokol and Řezáčová 2000, Dai et al. 2014), wind speed over complex terrain (Schicker et al. 2017), global horizontal irradiance and clear-sky index (Mejia et al. 2018).

### **1.5 Summary of Aims of the Thesis**

The aims of the thesis follow:

1. Investigate interactions between the large-scale environment and the low-level atmospheric stability to daily winter precipitation across the Snowy.
2. Examine the sensitivity of the wintertime precipitation over the Snowy Mountains of southeast Australia to changes in the low-level atmospheric stability as seen through the non-dimensional mountain height index and understand the relationship between the low-level stability and the synoptic meteorology, if any.
3. Evaluate the skill of cluster analysis coupled with a MOS methodology to develop stepwise regression models to improve the accuracy of ACCESS\_R daily wintertime precipitation forecast.
4. Use the Weather Research and Forecasting Model (WRF) to understand the impact of the dynamical, microphysical processes and model resolution on precipitation over the Snowy Mountains.

Aims of this study are summarized by the following listed chapters in this dissertation:

Chapter 2: *Characteristics of Wintertime Daily Precipitation over the Australian Snowy Mountains*

The relationship between orographic precipitation, low-level thermodynamic stability, and the synoptic meteorology is explored for the Snowy Mountains of southeast Australia. A 21-yr dataset (May–October, 1995–2015) of upper-air soundings from an upwind site is used to define synoptic indicators and the low-level stability. A K-means clustering algorithm was employed to classify the daily meteorology into four synoptic classes.

### Chapter 3: *Prediction of wintertime daily precipitation over the Snowy Mountains*

Building on these historical relationships, model output statistics (MOS) from a moderate resolution (12-km spatial resolution) operational forecast were used to develop stepwise regression models designed to improve the 24-h forecast of precipitation over the Snowy Mountains. A single regression model for all days was found to reduce the RMSE by 7% and the bias by 75%. A class-based regression model was found to reduce the overall RMSE by 30% and the bias by 85%.

### Chapter 4: *Simulations of orographic precipitation in the Snowy Mountains of Southeastern Australia*

In Chapter 4 we evaluate the Weather Research and Forecasting (WRFV3.8.1) NWP model in simulating the precipitation and clouds using high density ground based and satellite observations. A case study of a heavy precipitation event in late autumn (May 2016) is presented to better understand a typical wintertime storm associated with a cold frontal passage in the Snowy Mountains of southeastern Australia. A suite of carefully designed sensitivity simulations are undertaken to investigate the impact of the dynamical and microphysical processes on orographic precipitation over the Snowy Mountains.

### Chapter 5: Conclusions

## **Chapter 2**

### **Characteristics of Wintertime Daily Precipitation over the Australian Snowy Mountains**

## 2.1 Introduction

Distinct from daily forecasts and estimates, the climatology of precipitation in southeastern Australia has been of great interest, particularly over the last decade. For instance, Landvogt et al. (2008) produced a climatology of wintertime precipitation in the Australian Alpine regions, in which daily precipitation was categorized into synoptic clusters consisting of “prefrontal”, “postfrontal”, and “cutoff” classes. Chubb et al. (2011) studied a 20-yr period beginning in 1990, which included most of the “millennium drought”, one of the most severe droughts in the past century (Timbal 2009). Through this period, a 43% decline in wintertime precipitation at high elevations (greater than 1000m) was observed. Local weather systems were classified into three major synoptic types (embedded lows, cutoff lows, and other) based on the synoptic mean sea level pressure (MSLP) and the 500-hPa geopotential height. Fiddes et al. (2015) employed a set of circulation dynamics indices to show that there has been a continuing decline in western high-elevation wintertime precipitation of the Australian Alps and a relatively stable rainfall trend in eastern parts of this region. These distinct phenomena are hypothesized to be caused by the likely presence of complex relationships between the amount of precipitation and large-scale climate patterns over this region, especially for extreme events (Theobald et al. 2015).

K-means cluster analyses have been widely used on a variety of meteorological observations to generate the main synoptic types. For example, Wilson et al. (2013) employed k-means clustering method on upper-air data in south-eastern Queensland and found eight dominant weather regimes. Half of the identified weather regimes were associated with moist conditions, contributing 77% of the annual rainfall while occurring only 35% of the time and more frequently during the summer. The remaining four regimes, were associated with less than 23% of the mean total annual rainfall, despite of their high frequency of occurrence (65%). Dai et al. (2014, hereafter D14) assigned the daily synoptic meteorology into one of four classes over the Australian Snowy Mountains, using a K-means clustering algorithm with the upwind upper-air sounding. They found that the two wet clusters accounted for 30% of all days and 70% of the total wintertime precipitation. These two wet classes were associated with fronts (both embedded and cutoff) and postfrontal conditions, respectively. Theobald et al. (2015) provided eleven distinct synoptic circulation types that brought greater than 10 mm surface precipitation to the Snowy Mountains, using k-means clustering

method. Synoptic circulation was developed by combining 21, equally-weighted meteorological variables throughout the tropospheric column.

## **2.2 Winter precipitation characteristics**

Following Chubb et al. (2011), a rainy day is defined at precipitation (including solid precipitation) threshold of  $0.25 \text{ mm day}^{-1}$  for the average Snowy Hydro Ltd. (SHL) surface observations (see details in section 2.3). A basic summary of the winter precipitation is provided in Table 2.1. The frequency of rainy days is seen to follow a seasonal cycle with peaks being present in July and August. The intensity, however, is not found to present such a cycle; an overall mean intensity of  $10.4 \text{ mm day}^{-1}$  is observed for rainy days, with a standard deviation of  $13 \text{ mm day}^{-1}$ . The mean intensity can be broken down into quartiles, which again do not display any strong seasonal cycle over the course of winter; however this seasonal cycle is apparent in the boxplot of the mean monthly accumulated precipitation (Figure 2.1, top plot). Average monthly accumulated precipitation over 21-yr on rain days indicates lower values in the transition months of May and October with an overall wintertime mean precipitation (the winter mean monthly precipitation) of about 167 mm. There is also high interannual variability; for example, the June monthly precipitation has varied from 42 mm in 2015 to 300 mm in the next year. Looking at the May-Oct accumulated precipitation, we can see winter precipitation in this region, as one of Australia's wettest regions, seems to be highly variable from about 400 to 1400 mm in 2006 and 1996 respectively (Figure 2.1). There is also a negative trend in the wintertime precipitation amount, with the value of  $-22.69 \text{ mm yr}^{-1}$ , amounting to 476 mm over the analysis period (1995-2015). Chubb et al. (2011) found slightly stronger negative trend ( $-26 \text{ mm yr}^{-1}$ ) in the May–September precipitation amount for the period 1990–2009 over the high elevations of the Snowy Mountain.

Table 2.1 Main statistical characteristics of daily winter precipitation in mm for rainy days (>0.25mm).

Observations for 1995-2015						
Month	Rainy days' Frequency	Average Monthly (mm)	Mean Intensity (mm/day)	1 <sup>st</sup> Quartile (mm/day)	2 <sup>nd</sup> Quartile (mm/day)	3 <sup>rd</sup> Quartile (mm/day)
May	41%	122.5	9.5	6.7	9.8	12.8
June	56%	171.5	10.6	5.7	10.6	14.2
July	63%	179.6	9.7	8.3	9.5	11.7
August	60%	193.1	10.9	9.0	10.6	13.4
September	53%	192.1	11.6	10.0	11.7	13.0
October	44%	143.3	10.0	6.4	9.1	13.1
May-Oct	52%	166.7	10.4	7.7	10.2	13

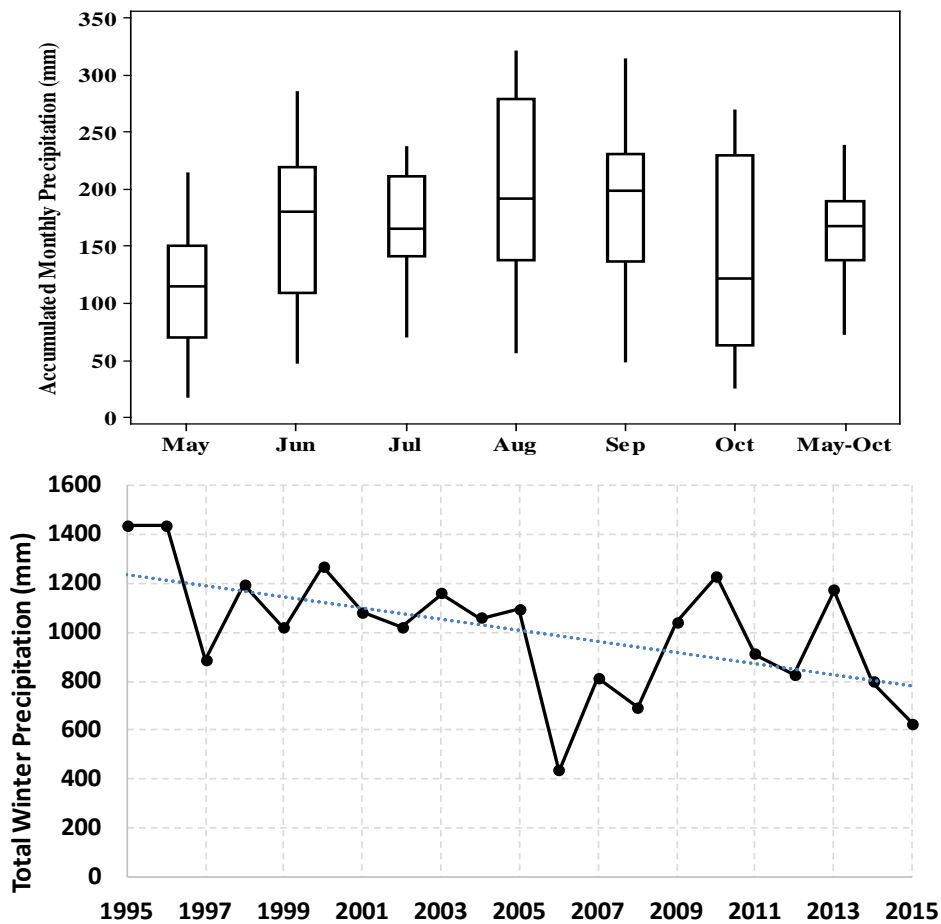


Figure 2.1 May–Oct total monthly precipitation for the period 1995–2015 (top plot). May–Oct total precipitation in the high elevations of the Snowy Mountains. The linear fit has slope of  $-22.69 \text{ mm yr}^{-1}$  (bottom plot).

Previous studies suggest that precipitation in southeast Australia is generally governed by large-scale climate drivers (Risbey et al. 2009). Risbey et al. (2009) showed that the relationships between the remote drivers and the Australian rainfall, vary spatially and with season and are not sensitive to the choice of index representing the drivers. For example, they reported the IOD was mostly related to rainfall in the south and west of the continent during June–October, while a correlation between the SAM and rainfall existed in all seasons in southwest and southeast parts of the continent. Here the relationships between the wintertime precipitation in the high elevations of the Snowy Mountains and the main climate drivers are also explored. Table 2.2 illustrates the correlations between monthly wintertime precipitation in the Snowy Mountains and the climate drivers over the period of 1995-2015.

The SOI index, measuring the anomaly of pressure difference between Tahiti and Darwin, indicates the atmospheric circulation across the Pacific which has significant positive correlation with rainfall over the southern Australia during the late winter and early spring (Risbey et al. 2009). This driver is found to be significantly strongly correlated ( $r \approx -0.5$ ) with precipitation in the high elevations of the Snowy Mountains in early spring (Sep-Oct, see Table 2.2). The Indian Ocean Dipole (IOD) shows the sea surface temperature anomaly difference between the tropical western and southeastern Indian Ocean reflects a negative relationship with values  $r = -0.74$ ; showing a consistent interannual variability with the southeast Australia (Risbey et al. 2009).

Negative correlations are found between rainfall and the two components of the subtropical ridge, position of the subtropical ridge (STR\_P) and the intensity of the subtropical ridge (STR\_I), over the winter. These correlations tends to peak in August. No statistically significant relationships are shown during the transition months (May and Oct). STR\_I and STR\_P are found to have the highest correlations with precipitation in July-Sep ( $r = -0.68$  on average) and in June-Sep ( $r = -0.60$  on average), respectively (see Table 2.2). In addition, there is a stronger relationship between STR\_P and the rainfall ( $r = -0.54$  for the whole winter) than with STR\_I ( $r = -0.29$  for the whole winter), implying that the ridge position may suppress the rainfall over the Snowy Mountains more efficiently than the intensity. The May-Oct cycle of the STR\_P (x-axis) and STR\_I (y-axis) averaged across the periods of this study (1995-2015) is compared with the long-term (1890–2015) climatology of Timbal and

Drosowsky (2013) in Figure 2.2. The monthly mean subtropical ridge over the 21-yr period from 1995 to 2015 shows a very noticeable anomaly towards greater intensity and more southerly location. This feature can also be seen from the positive slope of the linear trend of these data over 21-yr (see Figure 2.2).

The Southern Annular Mode (SAM) reflects the poleward contraction of the westerly belt that circles Antarctica and is found to be a dominant mode of atmospheric variability in the mid/high latitudes in the Southern Hemisphere (Thompson and Solomon 2002). Marshall (2003) calculated this index using the mean MSLP observations from six stations as a proxy of zonal mean at both 40° and 65 °S from 1958 to present. Looking at Table 2.2, for the entire winter period (May-Oct, 1995-2015), statistically significant correlations are found between mean rainfall and all the climate drivers except SAM. The positive phase of SAM shifts the belt of strong westerly poleward, whereby diminishing westerly over the southeast Australia during winter (Hendon et al. 2007). The observed significant negative correlations between SAM and the rainfall during June and July may be a result of poleward shift of the mid-latitude westerly (hence cold fronts) due to the positive SAM, which leads to the suppression of the orographic precipitation over the Snowy Mountains. Chubb et al. (2011) also reported about 30% less wintertime precipitation amount during a positive phase of SAM in the high-elevation gauges over the Snowy Mountains.

The Atmospheric Blocking Index is also another regional synoptic feature of the winter circulation in the southern hemisphere. It depends on the zonal components of the mean 500-hPa wind at several latitudes. The mathematical expression of this index is

$$\text{Atmospheric Blocking Index} = 0.5(U_{25} + U_{30} + U_{55} + U_{60} - U_{40} - U_{50} - 2U_{45}) \quad (2)$$

where  $U_L$  represents the zonal component of the mean 500-hPa wind at latitude L (Pook and Gibson 1999). Following Risbey et al. (2009), wind data from the National Centers Environmental Prediction–National Center for Atmospheric Research (NCEP–NCAR reanalysis dataset) are utilized at 140°E (a typical longitude for Atmospheric Blocking in the Australian). The relationship is not statistically significant for the Atmospheric Blocking index at 140°E for the entire winter period average (May-Oct, 1995-2015, see Table 2.2). Atmospheric Blocking at 140°E is often linked to extended dry periods in southern Australia during winters; however, the resulting cut-off low systems moving equatorward neutralize

the influence of Blocking; and consequently favor rainfall events across southeast Australia (Pook et al. 2006), leading to the significant positive correlation ( $r = 0.29$ ) between precipitation and the Atmospheric Blocking Index in July (Table 2.2).

Table 2.2 The Pearson correlation coefficients of monthly winter precipitation and large-scale drivers of rainfall across the Snowy over the period 1995-2015. Statistical significant at the 0.05 confidence level (2-tailed) is indicated by one asterisk. ABI: Atmospheric Blocking Index

Month	SOI	IOD	SRT_I	STR_P	SAM	ABI
May	0.11	-0.15	-0.11	-0.36	0.16	0.12
June	0.02	-0.44*	-0.27	-0.42*	-0.55*	0.18
July	0.33	-0.26	-0.52*	-0.63*	-0.63*	0.29*
August	0.27	-0.29	-0.81*	-0.68*	-0.21	0.23
Sep.	0.5*	-0.44*	-0.70*	-0.67*	0.29	0.22
October	0.51*	-0.74*	-0.39	-0.17	0.40	0.24
Winter	0.31*	-0.36*	-0.29*	-0.54*	-0.15	0.15

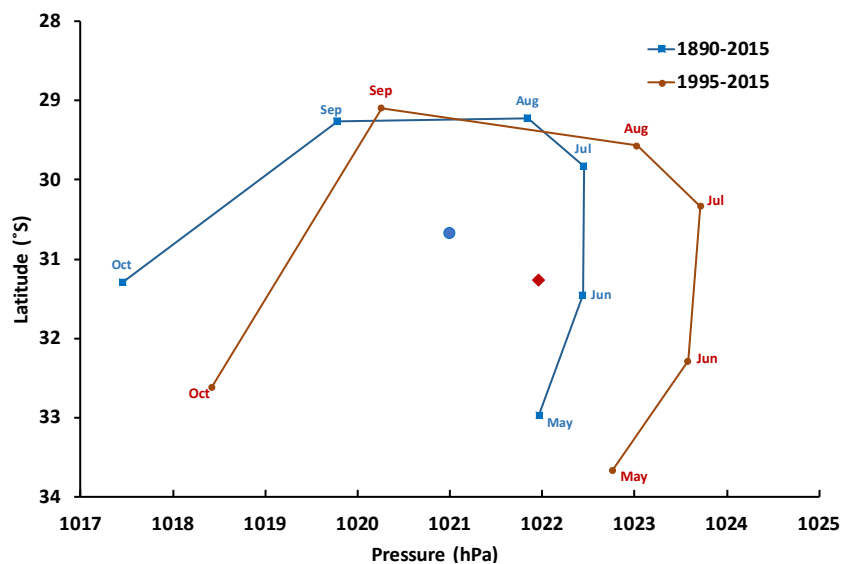


Figure 2.2 May-October cycle of monthly mean intensity (hPa) and subtropical ridge position ( $^{\circ}$ S) for the long-term 1890–2015 climatology (blue curve) with its six month average (blue dot) and for the period 1995-2015 (red curve) with its six month average (red diamond).

Table 2.3 illustrates the cross-correlations between these large-scale climate drivers at the 0.01 significant level, showing that the drivers are dependent of one another. The strongest significant correlations are between SAM-STR\_P (0.38) and SOI-IOD (-0.36); while, the lowest significance is for SOI-STR\_I (-0.28). STR\_P-STR\_I (0.34) and STR\_I-SAM (0.33) also indicate significant linear correlations. Timbal and Drosdowsky (2013), also found significant correlation between the two STR series from April to December (1890–2009). Due to the observed interaction between drivers, characterizing their impact on rainfall independently of one another is hard to detect and caution is needed to interpret such relationships. Risbey et al. (2009) used partial correlation techniques to account for this influence.

Table 2.3 Cross-correlation coefficients between six large-scale drivers of rainfall across the Snowy over the period 1995-2015. Statistical significant at the 0.01 confidence level (2-tailed) is indicated in bold. ABI: Atmospheric Blocking Index

	SOI	IOD	SRT_I	STR_P	SAM	ABI
SOI		<b>-0.36</b>	<b>-0.28</b>	-0.14	0.03	0.09
IOD			0.08	0.07	-0.06	0.11
SRT_I				<b>0.34</b>	<b>0.33</b>	0.11
STR_P					<b>0.38</b>	0.01
SAM						0.13
ABI						

Figure 2.3 and 2.4 show the time series of accumulated monthly precipitation in the high elevations of the Snowy Mountains, along with the time series of large-scale drives. There is also a negative trend in the total monthly precipitation amount, with the value of  $-0.58 \text{ mm month}^{-1}$ , over the analysis period (1995-2015). The two STR series show an increasing trend over the analysis period toward higher intensity and a more southerly location, while the Atmospheric Blocking Index and SAM show a very weak linear trend that is consistent with their weak relationship with precipitation (Table 2.2). The sea surface temperature anomaly difference between the tropical western and southeastern Indian Ocean (IOD) exhibits positive trend, indicating negative correlation with precipitation.

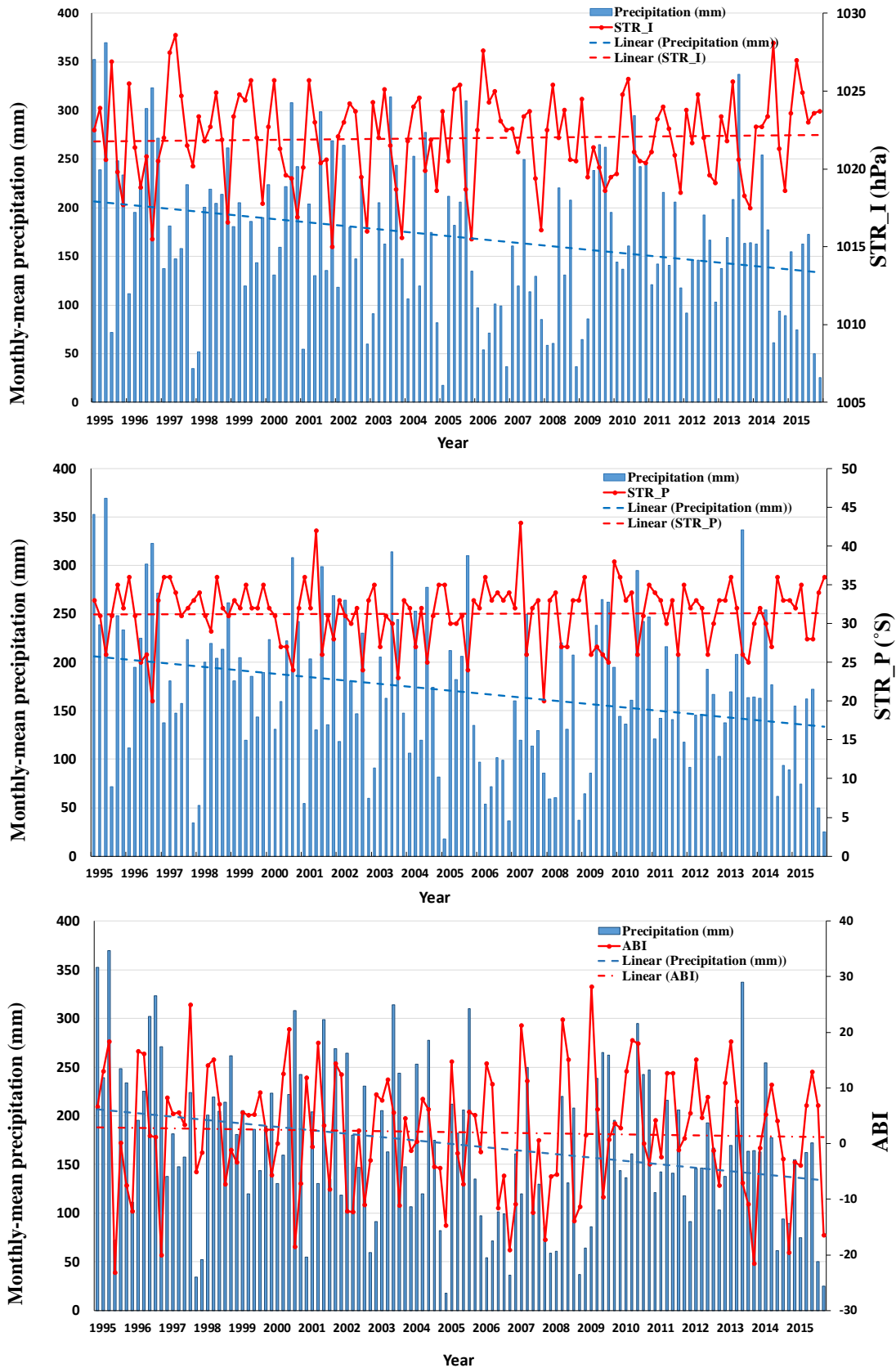


Figure 2.3 Time series of monthly-mean precipitation in the Snowy Mountains (blue bars), with time series (red line) of climate drivers (top) STR\_I, (middle) STR\_P and (bottom) Atmospheric blocking Index (ABI).

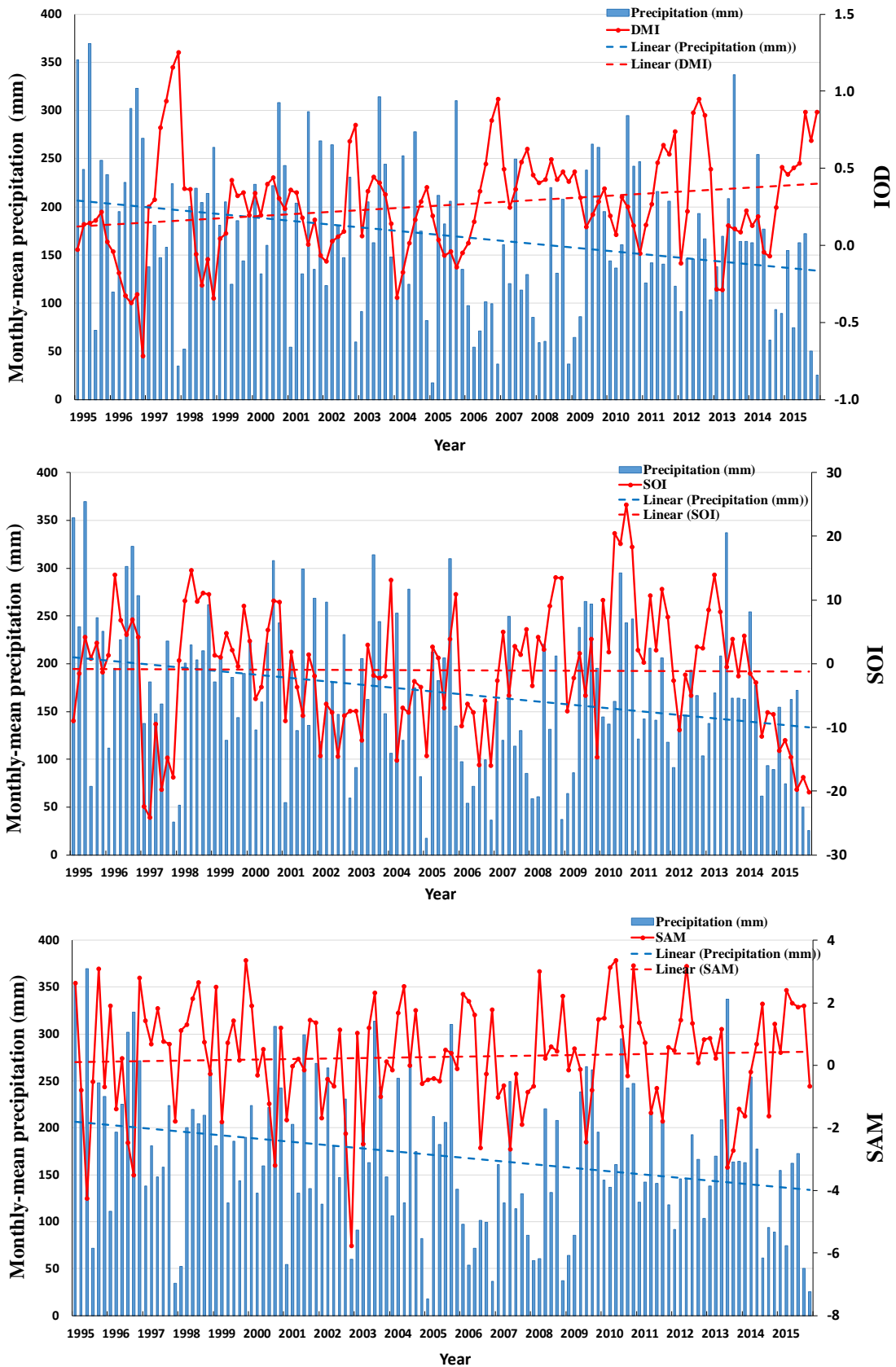


Figure 2.4 Time series of monthly-mean precipitation in the Snowy Mountains (blue barbs), with time series (red line) of climate drivers (top) IOD, (middle) SOI and (bottom) SAM.

## 2.3 Datasets:

### 2.3.1 Ground-based wintertime precipitation dataset

Half-hourly precipitation is obtained from seven weather stations above 1100m across the Snowy Mountains for a 21-yr period from 1995 to 2015. These high-elevation gauges, operated by Snowy Hydro Ltd. (SHL), utilize well-maintained heated tipping buckets for precipitation measurements. For consistency with the soundings, daily precipitation is obtained by aggregating the half-hourly precipitation from 1000 local time (0000 UTC) to the same time of the next day. Chubb et al. (2011, 2016) have evaluated the quality of the precipitation gauge data, finding appropriate accuracy and reliability of these measurements for climatological studies. The locations, elevations, operating year of the gauges and their fairly uniform long-term mean wintertime precipitation (May–October) are shown in Figure 2.5 and Table 2.4, respectively. For the 21-yr period considered, a full daily record (no missing data) of all stations was available for approximately 60% of the time. When data from one or more sites was either completely missing or its quality was flagged, the area-average daily precipitation was taken to be the mean of the remaining valid observations. No systematic bias in missing or flagged data has previously been noted. For the winter period 2014–15, 92% of all days have at least five stations that had valid data contributing to the mean value.

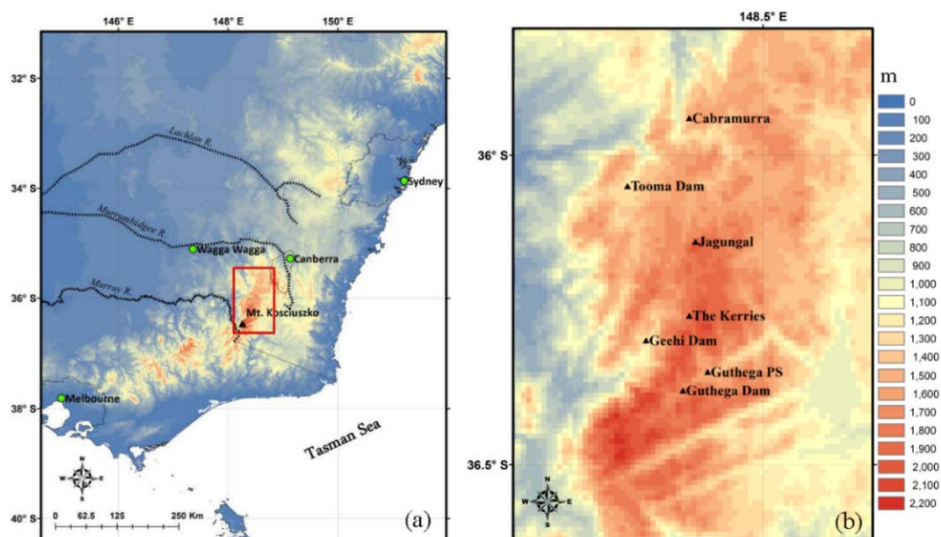


Figure 2.5 a) Map of the Snowy Mountains analysis region (red box) in southeastern Australia showing the closest upper-wind site of the BoM to the Snowy Mountains (Wagga Wagga). b) Location of the seven alpine rain gauges used in this study (enlarged red box).

Table 2.4 Properties of precipitation gauges sites at high altitudes in the Snowy Mountains. The mean winter precipitation values are calculated over the period 1995-2015.

<b>Site</b>	<b>Start Year</b>	<b>Longitude (°)</b>	<b>Latitude (°)</b>	<b>Elevation (m)</b>	<b>Mean winter Precipitation (mm)</b>
<b>Tooma Dam</b>	1992	148.28	-36.05	1221	1156.96
<b>Geehi Dam</b>	1992	148.31	-36.30	1175	1054.92
<b>Jagungal</b>	1990	148.39	-36.14	1659	1104.37
<b>The Kerries</b>	1995	148.38	-36.26	1740	1027.27
<b>Guthega Dam</b>	1992	148.37	-36.38	1558	881.84
<b>Guthega Power Station</b>	1994	148.41	-36.35	1320	963.30
<b>Cabramurra</b>	1955	148.38	-35.94	1482	857.69

### 2.3.2 Wagga Wagga sounding dataset

The nearest upwind sounding site to the Snowy Mountains is at Wagga Wagga, located about 180km to the northwest (Figure 2.5). Both Chubb et al. (2011) and D14 successfully employed these soundings to define the synoptic meteorology during the cold seasons. For the winter period of 1995–2015, the 0000 UTC sounding data were obtained from the database of University of Wyoming (<http://weather.uwyo.edu/upperair/sounding.html>). Soundings were available for 75% of the days (2897 out of 3843). Following D14, as a first step we employ a cluster analysis with six synoptic indicators calculated from the Wagga Wagga soundings to investigate interactions between the large-scale environment and daily winter precipitation across the Snowy Mountains. The synoptic indicators chosen are detailed in Table 2.5. Briefly, the three indicators TW, QV, and QU represent the available amount of water for the formation of precipitation, while TT and SH are considered to be simple estimates of the static stability of the atmosphere (e.g. Henry 2000).

Table 2.5 Summary of six synoptic indicators used to represent large-scale environment

Variables	Abbreviation	Formula	Unit
Surface pressure at Wagga Wagga	GP	Non-Applicable	<i>hPa</i>
Southerly moisture flux up to 250 hP	QV	$\frac{1}{g} \int qV dp$	$Kg s^{-1} m^{-1}$
Westerly moisture flux up to 250 hP:	QU	$\frac{1}{g} \int qU dp$	$Kg s^{-1} m^{-1}$
Total moisture up to 250 hPa	TW	$\frac{1}{g} \int q dp$	$hPa. s^2. m^{-1}$
Root-mean-square wind shear between 850 and 500 hPa	SH	$\sqrt{\left(\frac{\Delta U}{\Delta z}\right)^2 + \left(\frac{\Delta V}{\Delta z}\right)^2}$	$s^{-1}$
Total totals index	TT	$T(850) - 2T(500) + T_d(850)$	$^{\circ}C$

Expanding on the framework of D14, the low-level atmospheric stability, i.e. the non-dimensional mountain height ( $\hat{H}$ ), is added as a seventh predictor. TT and SH are defined between the levels of 850 and 500 hPa; whereas  $\hat{H}^2$  is defined to a height of 1000 m. The mathematical expression of the non-dimensional mountain height is

$$\hat{H} = \frac{1}{Fr} = \frac{Nh}{U}, \quad (1)$$

where  $U$  is the cross-mountain wind speed (m/s) and  $h$  is the mountain height ( $h=1$  km representing the mean elevation of the region (e.g. Chubb et al. 2011)).  $N$  is the Brunt–Väisälä frequency ( $s^{-1}$ ). Here the average  $U$  and  $N$  from 200 MSL up to 1200 MSL are used for the calculations. The Brunt–Väisälä frequency shows of the strength of the buoyancy force. It depends on whether the air impinging on the mountain is saturated. Following Hughes et al. (2009), the moist Brunt–Väisälä frequency (Durrán and Klemp 1982) is employed when the relative humidity is greater than 90% (i.e. saturated conditions), otherwise the dry Brunt–Väisälä frequency is adopted. As the value of  $N$  is imaginary when the atmosphere is conditionally unstable, so is the value of  $\hat{H}$ . In order to account for conditionally unstable events, which occur about 11% of the time, we employ the square of the  $\hat{H}$  values ( $\hat{H}^2$ ) for all analysis (e.g. Reinecke and Durrán 2008). Negative values of  $\hat{H}^2$  indicate conditional instability. Hughes et al. (2009) showed that the large square Froude number values have similar behaviour as the negative ones (known also as conditionally unstable).

For small  $\hat{H}^2$  values, the low-level atmospheric conditions are generally referred to as being unstable to orographic lifting, implying that the airflow can readily pass over the terrain and mountain waves will be generated. For large  $\hat{H}^2$  values, the flow can be stagnated or diverted laterally around the barrier instead of being lifted over the terrain. In this scenario, stable or blocked conditions (hereafter “blocked days”) are generally observed (e.g. Watson and Lane 2014; Miao and Geerts 2013; Wang et al. 2016). Following the literature, we use  $\hat{H}^2$  equal to 1 as the threshold to distinguish stable and unstable conditions. In practice, however, the transition is not precise, especially as we use only a fixed estimate for the mountain height,  $h$ . As discussed, the spatial distribution, magnitude and frequency of orographic precipitation has commonly been found to be sensitive to  $\hat{H}^2$ . When  $\hat{H}^2 < 1$  (unblocked days here), heavier precipitation events can be expected (e.g. Miglietta and Buzzi 2001; Colle 2004; Wang et al. 2016). By inspecting the coastal winds of California, Hughes et al. (2009) showed that the spatial distribution of precipitation became more homogenous for blocked cases, while for unblocked flows local orographic precipitation was strongly dependent on the slope of topography.

### 2.3.3 ERA-Interim reanalysis dataset

Following Theobald et al. (2015), we employ the ERA-Interim reanalysis products (Dee et al. 2011) provided by the European Centre for Medium-Range Weather Forecasts (ECMWF) to derive composite synoptic charts that correspond to the clusters. The ERA-Interim data we employ are from 1995 onwards and at a spatial resolution of  $0.75^\circ \times 0.75^\circ$ . As the soundings at Wagga Wagga were not available at all time, the six synoptic indicators and  $\hat{H}^2$  obtained from the ERA-Interim reanalysis dataset are used to fill in missing physical soundings for days in 2014-15 (physical soundings were only available for the 154 days during the analysis period). Comparisons of the in-situ Wagga Wagga soundings and the corresponding ERA-Interim reanalysis soundings for common days over the 21-year winter period show strong correlations for all synoptic indicators (GP: 0.99, SH: 0.90, TT: 0.92, TW: 0.97, Qv: 0.98, Qu: 0.97). Therefore, we consider using the ERA-Interim reanalysis soundings as a surrogate is appropriate. We note that as the Wagga Wagga soundings are likely employed in the data assimilation for ERA-Interim, the two sets of soundings may not be completely independent. The ERA-Interim soundings may be less skilled when the physical soundings are not available.

## 2.4 Methodology of cluster analysis

The weather systems in southeastern Australia can be classified using a simple clustering methodology such as *K*-means (Hartigan and Wong 1979). This methodology follows an iterative refinement approach that assigns each observation to cluster that minimizes the overall Euclidean distance to cluster centroids. The number of clusters chosen, 'k', is arbitrary, although numerous criteria have been developed (e.g. Rossow et al. 2005; Pope et al. 2009).

Pope et al. (2009b) examined the variability of 49 wet seasons (September–April) for north Australia by performing the k-mean cluster analysis using the mean wind and thermodynamic information from sounding data observed at Darwin. The five distinct regimes are found to be significantly different in their synoptic environment, cloud patterns, and rainfall distributions. The mesoscale convective systems in northern Australia have also been grouped into four classes, based on some physical properties (Pope et al. 2009a). Recent studies by Wilson et al. (2013) and D14 show that winter days in Australia can be categorized into unique synoptic regimes by utilizing six synoptic indicators as independent variables for the clustering procedure. Accordingly we have chosen these variables, too. In addition to these six indicators,  $\hat{H}^2$  is also employed to account for the low-level local atmospheric stability.

Determining the optimal number of clusters using the *K*-means algorithm is challenging given the opposite relationship between the number of clusters and their variances. Following D14, the optimal number of clusters is determined when the probability distributions of the daily rainfall for different clusters can be separated distinctively. Given that a relationship between orographic precipitation and  $\hat{H}^2$  is expected (Colle 2004), it is also worthwhile to appreciate the probability distributions of  $\hat{H}^2$  for each cluster when only the original six indicators are employed for the cluster analysis. A two-sample Kolmogorov-Smirnov (KS) test is applied to insure the distinctiveness of the distributions.

## 2.5 Results of synoptic classification

### 2.5.1 Classification using six indicators

The K-means clustering technique was applied to the Wagga Wagga soundings data (complemented with ERA-I soundings for days when the physical soundings were unavailable) for winter days for the 21-year period 1995-2015 using the six indicators. When employing the original six sounding variables (TT, SH, QU, QV, GP & TW), the new analysis was consistent with that of D14; four clusters were the minimum number found to produce distinct daily rainfall probability distributions (Figure 2.6), passing the KS test at the 5% significance level. Moving from a four-cluster to five-cluster analysis, the KS test fails to produce distinct precipitation distributions. Thus, four clusters with significantly different distributions are chosen for this analysis. As a major objective of this research is to better understand the nature of the low-level stability,  $\hat{H}^2$ , over the Snowy Mountains, and its value as a predictor of orographic precipitation, daily  $\hat{H}^2$  probability distributions are also produced (Figure 2.7). As with the daily precipitation, four clusters lead to distinct distributions of  $\hat{H}^2$ , suggesting that the low-level stability is reflected in the broader synoptic meteorology.

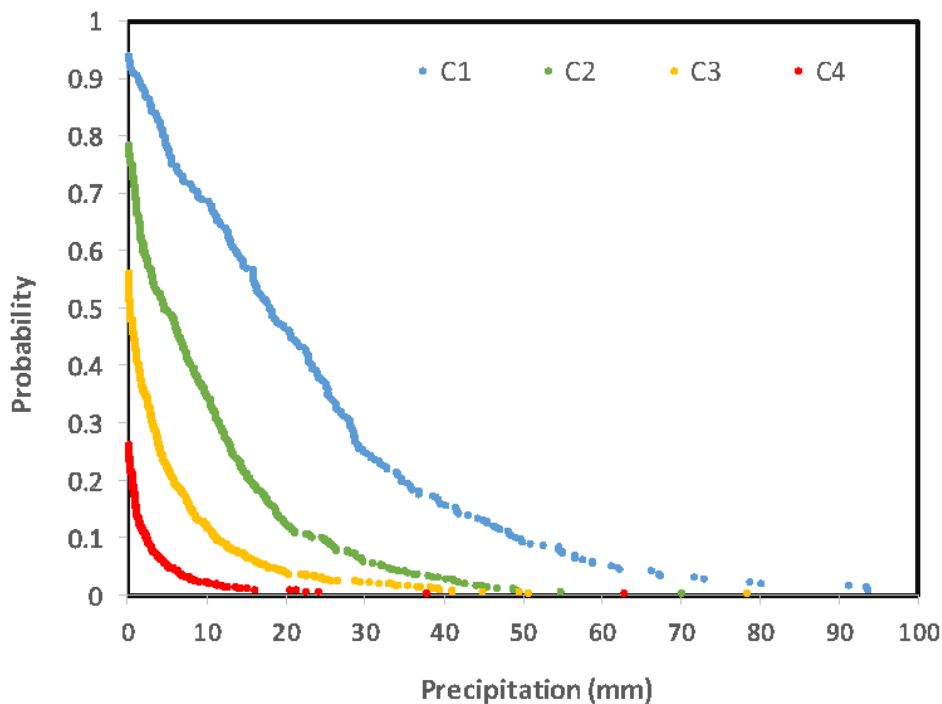


Figure 2.6 Probability distribution of daily winter rainfall over the period 1995-2015 based on six large-scale synoptic indicators.

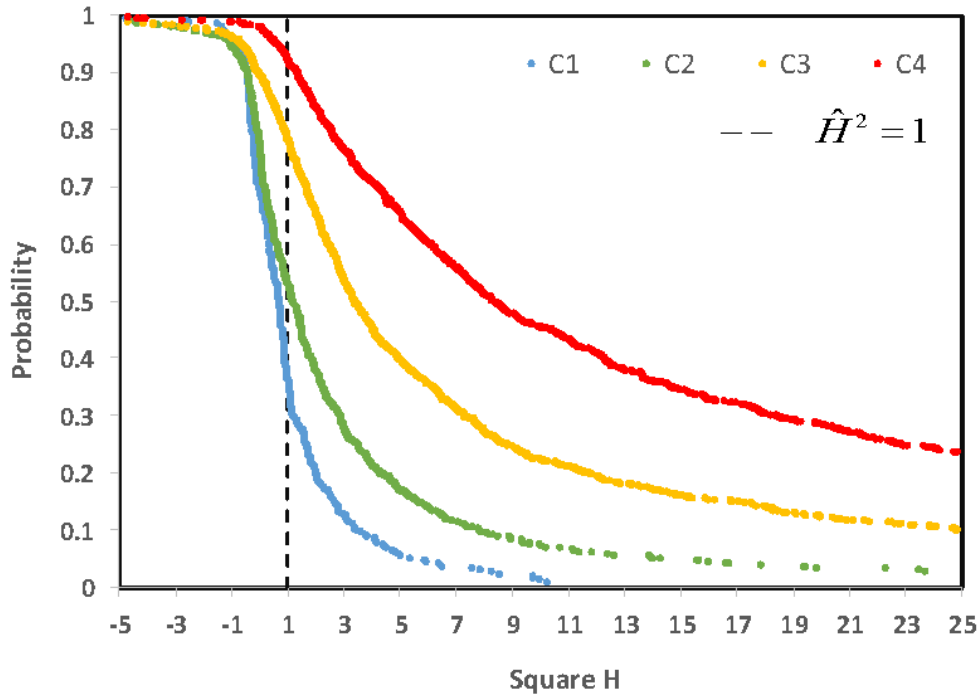


Figure 2.7 Probability distribution of  $\hat{H}^2$  for next 24 hours after sounding measurements over the period 1995-2015 based on six large-scale synoptic indicators.

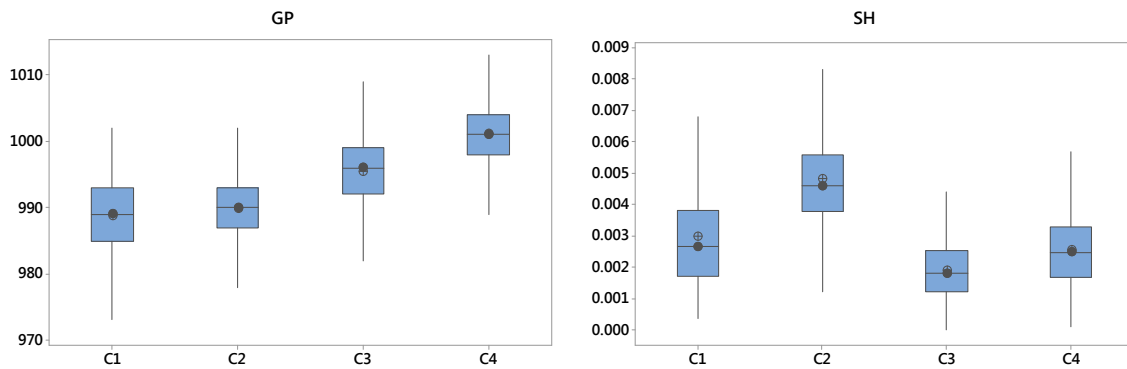
A brief summary of the main statistical characteristics of each class is given in Table 2.6. The first cluster, C1, is the wettest cluster containing the majority of the heavy precipitation days, while the last cluster, C4, is the driest cluster containing the majority of the low precipitation days. Clusters C1 (frequency of rainy days: 94%, median: 18.97 mm day<sup>-1</sup>) and C2 (frequency of rainy days: 78%, median: 8.10 mm day<sup>-1</sup>) represent the wettest groups while C3 (frequency of rainy days: 55%, median: 3.79 mm day<sup>-1</sup>) and C4 (frequency of rainy days: 26%, median: 1.46 mm day<sup>-1</sup>) capture the driest weather. There are fewer days of C1 and C2 than C3 and C4. The frequency of rainy days and the intensity are decreasing from C1 to C4. The mean values of  $\hat{H}^2$  for the four clusters are -1.37, 3.11, 7.08 and 15.77, respectively. Higher values of  $\hat{H}^2$  indicate stronger blocking and, accordingly, less orographic precipitation. The fraction of unblocked days ( $\hat{H}^2 < 1$ ) is decreasing from 62% for C1 to 8% for C4. This fraction is slightly higher on rain days.

Table 2.6 Main statistical characteristics of daily winter rainfall and  $\hat{H}^2$  across synoptic clusters based on six-variable clustering

	Frequency			Mean	1 <sup>st</sup> Quartile	2 <sup>nd</sup> Quartile	3 <sup>rd</sup> Quartile			
	All days %	Rain days %	Unblocked* All (rainy days) %	Rainfall (rainy days) mm	Rainfall mm	$\hat{H}^2$	Rainfall mm	$\hat{H}^2$	Rainfall mm	$\hat{H}^2$
<b>C1</b>	9.8	94	62 (65)	23.14	8.19	0.03	18.97	0.66	30.75	1.58
<b>C2</b>	19.7	78	48 (57)	11.09	2.47	-0.05	8.10	0.68	15.32	2.34
<b>C3</b>	37.2	55	22 (32)	6.68	1.24	0.58	3.79	2.19	8.49	4.96
<b>C4</b>	33.3	26	8 (18)	3.41	0.77	1.52	1.46	3.72	3.91	9.78

\*Unblocked cases: days with  $\hat{H}^2 < 1$ .

In terms of synoptic indicators, Figure 2.8 shows box plots for each clusters. The values and trends amongst different groups are similar to the work of Chubb et al. (2011) and D14. The C1 has the lowest surface pressure (GP) with a mean value of 988.5 hPa, increasing towards C4 to a mean value of 1001.3 hPa. Looking at southerly moisture fluxes (QV), C1 is the only class that is mostly under the influence of northerly flux. The amount of westerly moisture flux (QU) drops when moving from C1 to C4. Considering QV, GP and QU patterns, C1 and C4 can be considered as two extreme classes. The variability of TT and TW is to some extent similar, with C1 (C4) having the highest (lowest) values, and C3 is slightly larger than C2 for both synoptic indicators. C2 has the highest mean shear with moderate static instability (as expressed by TT)



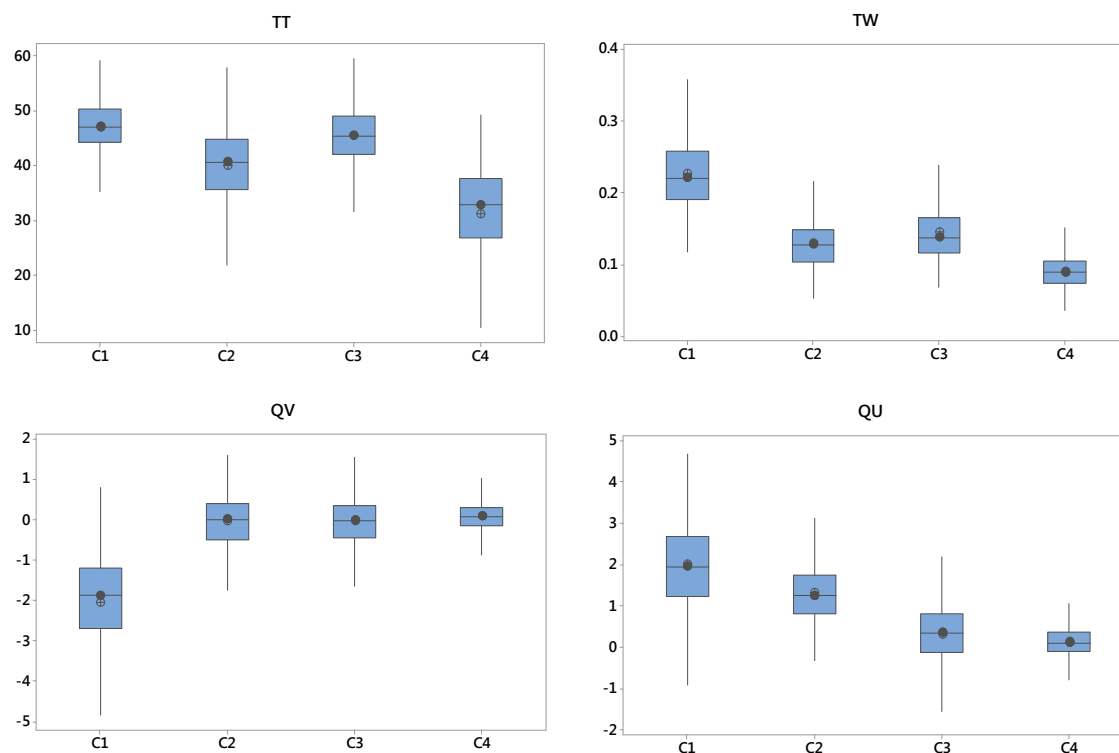


Figure 2.8 Box plot of synoptic indicators for four clusters with outliers removed. Upper and lower whiskers calculated based on the quartile method. Filled and unfilled dots show the median and mean values, respectively.

### 2.5.2 Temporal variability of synoptic classes using six indicators

The frequencies of occurrence for the four clusters are about 10%, 20%, 37% and 33%, respectively. The seasonal variability of clusters is found to be consistent with D14, the relative frequencies of C1 and C2 increase towards the end of winter. C3 is more frequent in early winter and C4 occurs more often in midwinter (Figure 2.9). Further, the synoptic meteorology of the wettest cluster C1, is consistent with the analysis of Chubb et al. (2011), a strong northwesterly moisture flux and low surface pressure are commonly present. C2 can also be generally relates to a postfrontal environment, where winds are predominantly westerly (Chubb et al. 2012).

It is also interesting to consider the interannual variability of the frequency of each class. The frequency of occurrence of C1, that occurs 10% of the time, varies from 4.7% in 2002 to 22.1% in 2013, with a 21-yr average of 10.4%. More than 46% of the winter days fall into the driest class (C4 that occurs 33% of the time) in 2006, while the frequency of occurrence

of C4 in 2013 is only 22.1% (Figure 2.10). This variation is consistent with Figure 2.1, where the lowest May-Oct accumulated precipitation found in 2006.

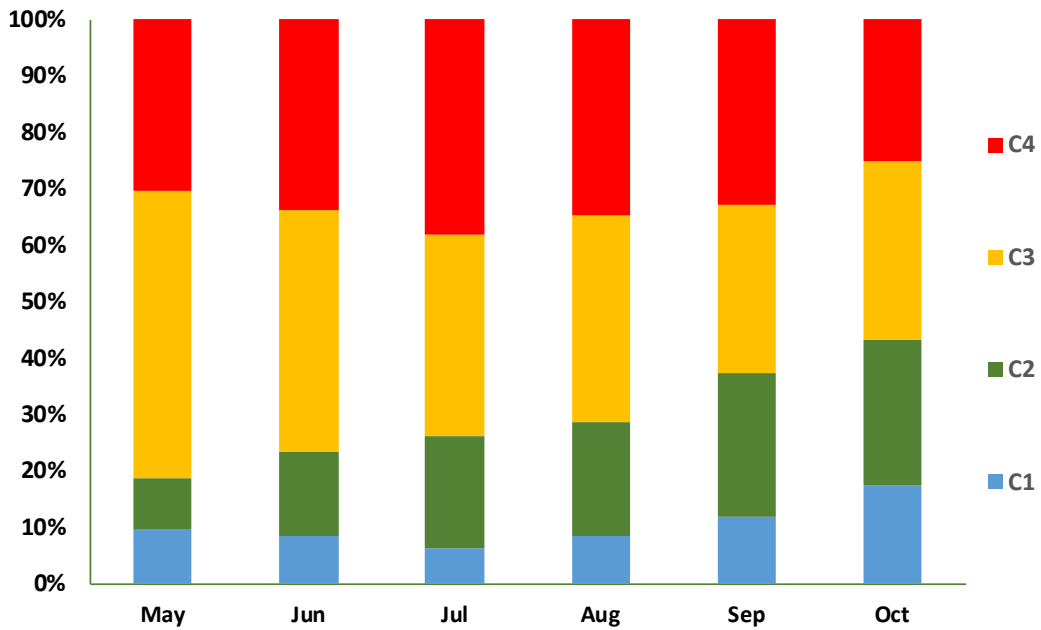


Figure 2.9 Seasonal variability of synoptic classes during 1995-2015.

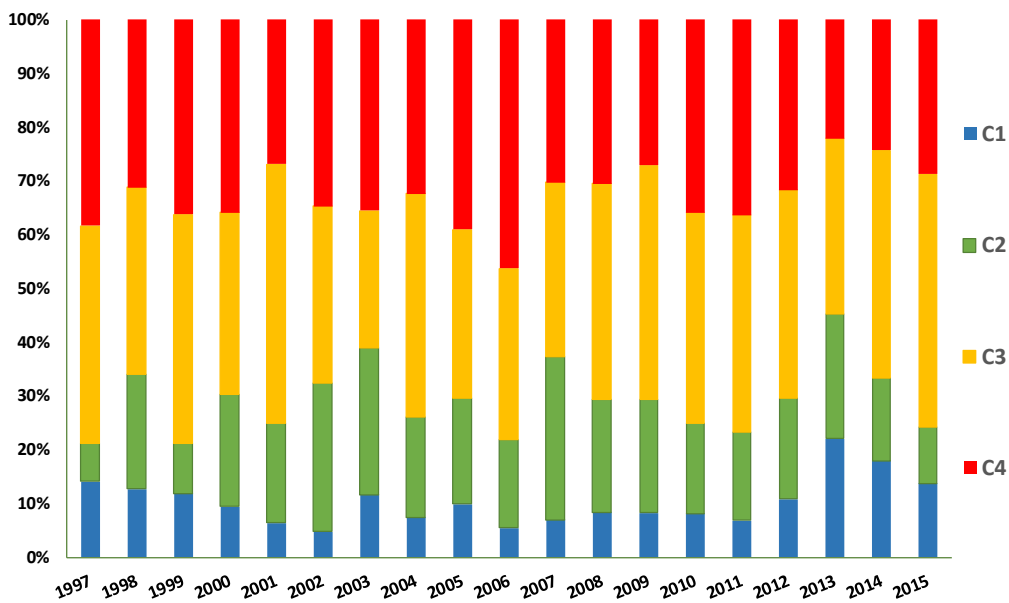


Figure 2.10 Interannual variability of synoptic classes during 1995-2015

### 2.5.3 Classification using seven indicators

Given the observed opposite relationship between orographic precipitation and  $\hat{H}^2$  during six-variable clustering, it is worthwhile to explore the sensitivity of the clustering analysis to the low-level stability by including  $\hat{H}^2$  as an additional input variable to the clustering method. A K-means clustering was then undertaken using the original six synoptic variables and  $\hat{H}^2$  (7-variable clustering results are only elaborated hereinafter). As before, four clusters were found to be necessary to distinctly represent the daily precipitation distribution (Figure 2.11). C1 and C2 were found to be quite stable to this revision with only a handful of days swapping between clusters. The two dry clusters, however, were found to be more sensitive to this clustering revision. 1037 out of the original 1123 days in C3 remain unchanged (5 days shifted to C1, 50 days to C2, and 31 days to C4), while 823 of the original 1003 days in C4 remain unchanged (35 days shifted to C2, and 145 days to C3). This further suggests that for the wet clusters, C1 and C2, that the low-level stability is reflected in the synoptic meteorology.

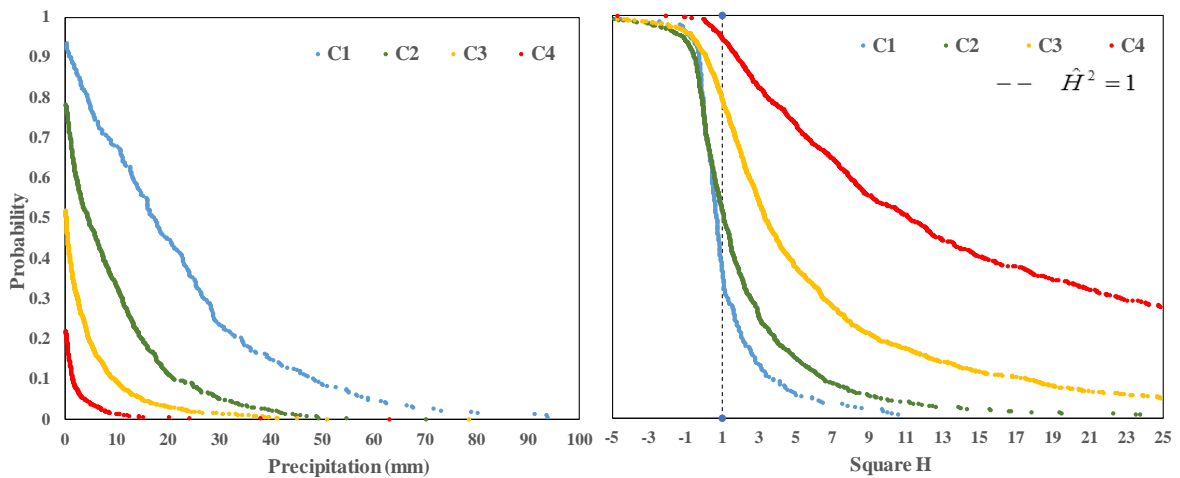


Figure 2.11 Cumulative distribution of precipitation (right) and  $\hat{H}^2$  (left) for next 24 hours after sounding measurements over the period 1995-2015 based on seven large-scale synoptic indicators.

According to Table 2.7, clusters C<sub>7</sub>1 (frequency of rainy days: 93%, median: 18 mm day<sup>-1</sup>) and C<sub>7</sub>2 (frequency of rainy days: 78%, median: 4.54 mm day<sup>-1</sup>) represent the wettest groups while C<sub>7</sub>3 (frequency of rainy days: 52%, median: 0.32 mm day<sup>-1</sup>) and C<sub>7</sub>4 (frequency of rainy days: 22%, median: 0.03 mm day<sup>-1</sup>) capture the driest weather. There are fewer days

of C<sub>71</sub> and C<sub>72</sub> than C<sub>73</sub> and C<sub>74</sub>. The mean values of  $\hat{H}^2$  for the four clusters are -0.45, 1.97, 6.24 and 20.20, respectively. Higher values of  $\hat{H}^2$  indicate stronger blocking and, accordingly, less orographic precipitation. The fraction of unblocked days ( $\hat{H}^2 < 1$ ) for the four clusters are 63%, 48%, 20% and 5%, respectively.

Table 2.7 Main statistical characteristics of daily winter rainfall and  $\hat{H}^2$  across synoptic clusters based on seven-variable clustering

	Frequency			Mean	1 <sup>st</sup> Quartile		2 <sup>nd</sup> Quartile		3 <sup>rd</sup> Quartile	
	All days %	Rainy days %	Unblocked* All (rainy days) %	Rainfall (rainy days) mm	Rainfall mm	$\hat{H}^2$	Rainfall mm	$\hat{H}^2$	Rainfall mm	$\hat{H}^2$
<b>C<sub>71</sub></b>	9.9	93	63 (66)	22.94	5.74	0.05	17.48	0.7	29.04	1.7
<b>C<sub>72</sub></b>	22.2	78	48 (53)	10.83	0.63	0.03	4.54	1.11	12.87	3.01
<b>C<sub>73</sub></b>	39.2	52	20 (30)	6.12	0	1.35	0.32	3.33	8.7	3.66
<b>C<sub>74</sub></b>	28.6	22	5 (12)	3.32	0	4.59	0.03	11.1	0.17	27.88

\*Unblocked cases: days with  $\hat{H}^2 < 1$ .

The probability density functions (PDF) of  $\hat{H}^2$  are broken down by cluster (Figure 2.12, a-d) for all days. Distribution of  $\hat{H}^2$  for all days is shown in stacked histogram in Figure 2.12e. For rainy days only, the PDF will be shifted to lower (less stable) values of  $\hat{H}^2$ , and for no rain days shifted to higher ones (more stable) (Figure 2.12f).

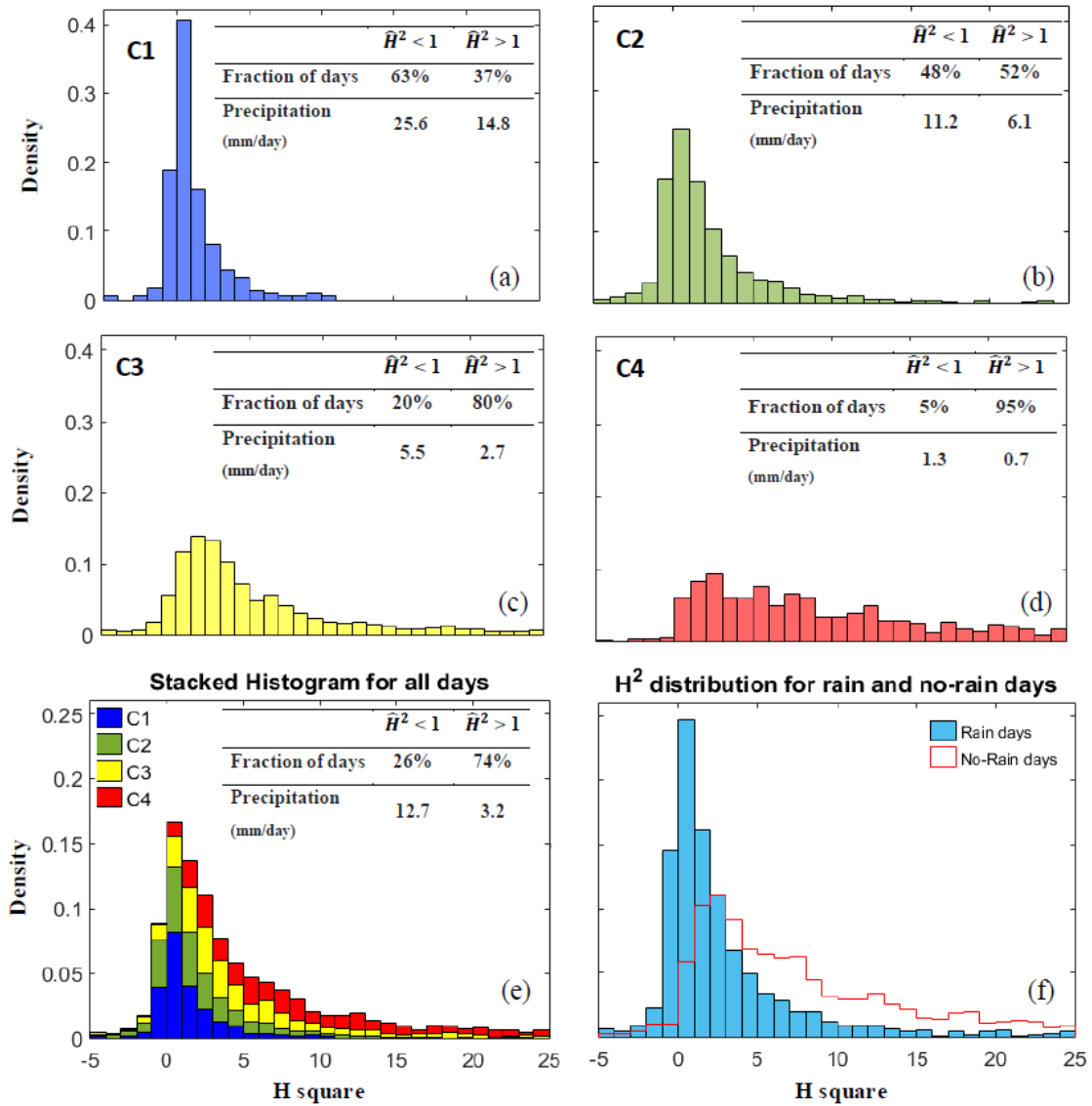


Figure 2.12 a-d) Distribution of  $\hat{H}^2$  for each cluster, e) stacked histograms of  $\hat{H}^2$  variable for different clusters, f) the  $\hat{H}^2$  distribution for No-Rain days and Rain days. ( $\hat{H}^2 > 25$ , occurring ~7% of the time and mostly in C4 are not shown). Note the different axes in (e and f) compared to (a-d)

## 2.5.4 Synoptic conditions associated with each class

### a. Synoptic features for the centroids of C1-C4

It is worthwhile to determine the synoptic meteorology under which each cluster occurs by considering the MSLP charts, obtained from the Bureau of Meteorology, and the associated upper-air sounding profile at Wagga Wagga weather station on days closest to the centre of

the four clusters. Table 2.8 summarizes the values of seven indicators for the closest day to centroid of each cluster.

The day closest to the centre of the wettest cluster (24 Oct 2011) has the lowest value of surface pressure (GP: 986 hPa), while the driest cluster centroid (13 Sep 2000) has the highest value of surface pressure (GP: 1001 hPa). The day closest to C<sub>7</sub>1 centroid shows the weakest static stability (as expressed by TT, SH and  $\hat{H}^2$ ). Looking at the fluxes, northerly moisture flux that is also greatest in magnitude can only be found in C<sub>7</sub>1. Note that negative values of QV indicate moisture flux in the northerly direction. This feature commonly occurs in prefrontal conditions. This indicator is relatively weak in the other cluster's centroids, suggesting the dominant northwesterly moisture flux in C<sub>7</sub>1 and westerly moisture flux in C<sub>7</sub>2, C<sub>7</sub>3 and C<sub>7</sub>4. The daily precipitation in centroids of each cluster is decreasing from 28.4 mm in C<sub>7</sub>1 to zero in C<sub>7</sub>4. The trends in this table are consistent with Figure 2.8.

Table 2.8 Values of seven indicators along with their daily precipitation for days closest to each cluster centroid.

	<b>Date</b>	<b>GP</b> <i>hPa</i>	<b>SH</b> <i>s<sup>-1</sup></i>	<b>TT</b> <i>°C</i>	<b>TW</b> <i>hPa.s<sup>2</sup>.n</i>	<b>QV</b> <i>Kg s<sup>-1</sup></i> <i>m<sup>-1</sup></i>	<b>QU</b> <i>Kg s<sup>-1</sup></i> <i>m<sup>-1</sup></i>	$\hat{H}^2$	<b>Precipitation</b> mm/day
<b>C<sub>7</sub>1</b>	24-Oct-11	986	0.0031	44.8	0.231	-2.148	2.335	0.49	28.40
<b>C<sub>7</sub>2</b>	15-Sep-05	988	0.0045	39.4	0.118	0.093	1.44	0.99	7.22
<b>C<sub>7</sub>3</b>	16-Sep-12	996	0.0018	43.6	0.133	0.131	0.427	13.65	0.11
<b>C<sub>7</sub>4</b>	13-Sep-00	1001	0.0024	28.4	0.086	0.242	0.120	25.17	0.00

To check the consistency of the concluded characteristics of these days, it is beneficial to look at their MSLP charts and sounding profiles that are show in Figure 2.13. It can be found that two dry clusters (C<sub>7</sub>3 and C<sub>7</sub>4) are mostly under the influence of high pressure system over the Snowy Mountains with a very stable and dry sounding for C<sub>7</sub>4. For the MSLP chart of the closest day to the centre of C<sub>7</sub>1, a low pressure system, which is cut-off from the main belt of low pressure, has developed and centred near the region with a cold front passing the region. Looking at the first sounding, it shows strong northwesterly winds associated with passage of cold front. In general, high clouds with cold cloud tops are expected as a cold front is coming through, while in postfrontal conditions, shallow clouds are expected to be dominant. This feature can be seen from the height of the inversion which gradually decreases from C<sub>7</sub>1 to C<sub>7</sub>4 in Figure 2.13.

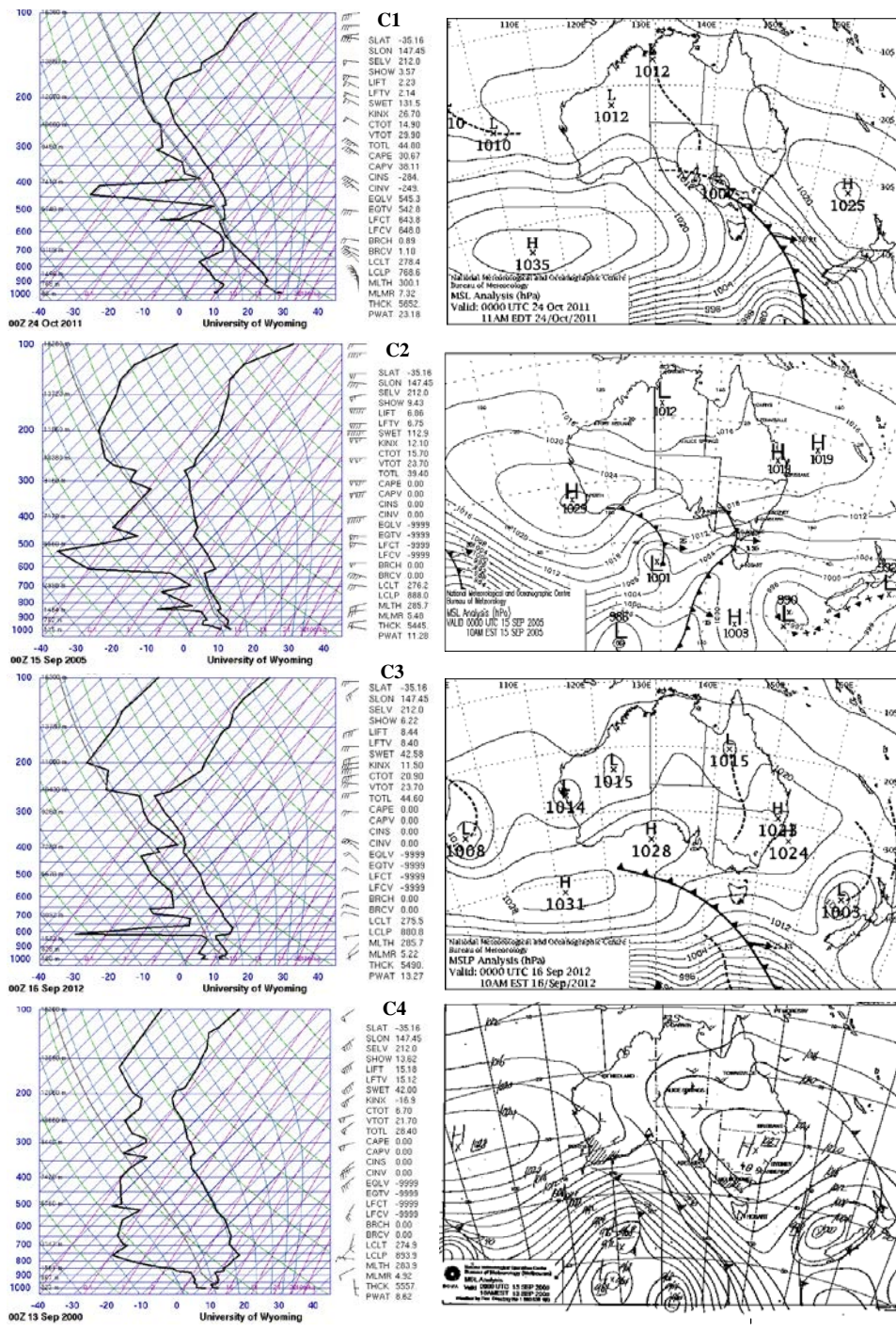


Figure 2.13 Upper-air sounding at Wagga Wagga weather station and MSLP chart for the days closest to the center of each class.

**b. Composite maps of the large-scale synoptic indicators for each cluster**

To better appreciate the synoptic meteorology of these four clusters (based on 7-variable clustering), ERA-Interim data are used to construct composite maps of the large-scale

synoptic indicators for each cluster. Following Theobald et al. (2015), the map domain is 20- 46°S and 120°-140°E in order to capture the dominant synoptic meteorology. For these maps, only the top 25% of days of each cluster are employed. Specifically, these are the days that have the shortest Euclidean distance to the cluster centre. While this approach is commonly used when employing daily observations (e.g. Pook et al. 2006; Theobald et al. 2015), it has been noted that the daily resolution of composite maps may mask some unresolved features within daily systems (e.g. a diurnal cycle), as well as over-represent slow-moving synoptic systems (Gallant et al. 2012).

Starting first with the MSLP and total water (Figure 2.14), general synoptic states can be assigned to the four clusters. The MSLP for C<sub>71</sub>, suggests that the cluster is associated with a frontal passage. It is not possible to distinguish between a cut-off low and an embedded low due to the compositing technique and the low number of clusters. Further, C<sub>71</sub> is associated with a maximum in total water over the mountains, which is seen to extend up the Great Dividing Range through New South Wales and Queensland. Chubb et al. (2011) employed a back-trajectory analysis to define a ‘moisture corridor’ across this region for heavy precipitation events. C<sub>72</sub>, while less well resolved, suggests that the frontal system has passed over mountains. Chubb et al. (2012) detailed a case study of a frontal passage over the nearby Brindabella ranges, where orographic precipitation was recorded over the 24-hour period after the passage of a front. Here air originating from the Southern Ocean brings limited moisture and modest precipitation. Skipping to the dry cluster C<sub>74</sub>, a strong high pressure system is evident over the region with very little moisture available. Cluster C<sub>73</sub> is less easy to classify, most likely including a variety of synoptic settings that ultimately lead to little precipitation. A high-pressure ridge is present across central Australia in the composite map, although it is much weaker than that of C<sub>74</sub>.

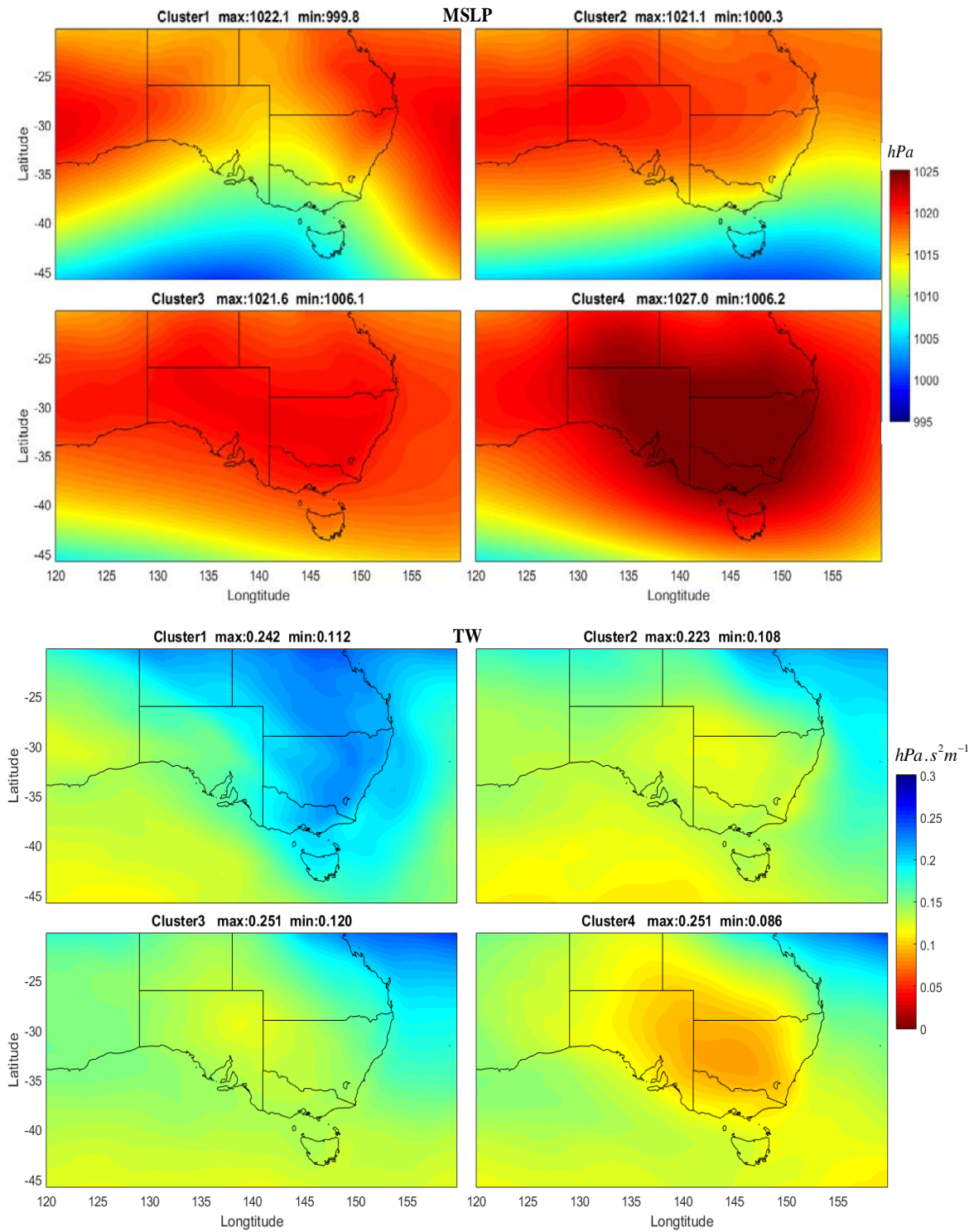


Figure 2.14 Composite charts of MSLP in hPa (Top) and TW in  $hPa \cdot s^2/m$  (bottom), showing total moisture up to 250-hPa, for the four classes. Era-Interim data (00UTC, May-October, 1995-2015) at a spatial resolution of  $0.75^\circ \times 0.75^\circ$  used to construct composite maps of only the top 25% of days of each cluster with the shortest Euclidean distance to the cluster centre. The corresponding maximum and minimum values of the examined variables are shown on top of the individual panels.

Turning to the moisture fluxes (Figure 2.15), the strong northerly and westerly moisture fluxes of C<sub>7</sub>1 stand out, consistent with a frontal passage. There is virtually no northerly moisture flux over the Snowy Mountains for C<sub>7</sub>2. It is strictly a westerly flux that is bringing the moisture for precipitation, again suggesting a post-frontal environment (Chubb et al. 2012). Spatially, C<sub>7</sub>3 and C<sub>7</sub>4 are quite similar, with weak fluxes evident over the mountains. C<sub>7</sub>4 is drier and has weaker fluxes of the two.

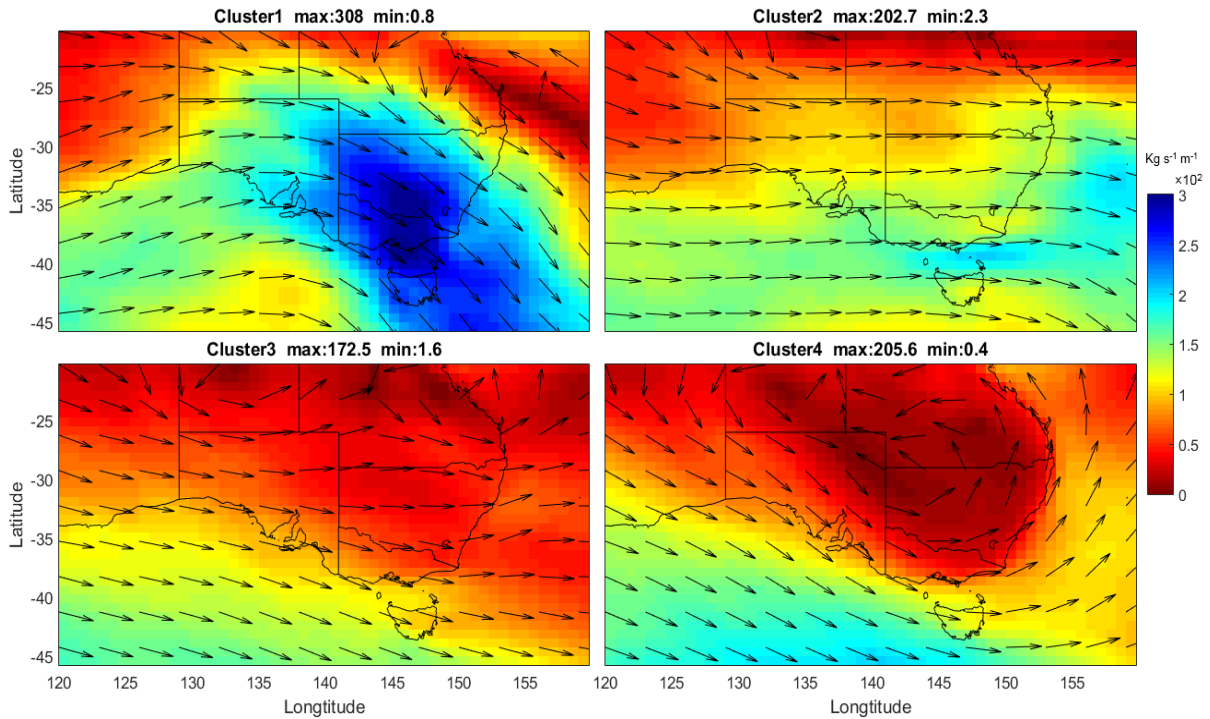


Figure 2.15 As in Figure 2.14, but showing QV and QU (westerly and southerly moisture flux up to 250-hPa) for the four classes. Colour-filled contours shows the magnitude of the moisture fluxes ( $\sqrt{QU^2 + QV^2}$ ) in Kg s<sup>-1</sup> m<sup>-1</sup> and arrows of the same length represent the moisture flux direction.

The synoptic stability composites (TT and SH, Figure 2.16) further complete the general classifications of clusters C<sub>7</sub>1 (frontal), C<sub>7</sub>2 (post-frontal) and C<sub>7</sub>4 (high pressure system). Over the mountains, the atmosphere is most unstable during a frontal passage and most stable under a high-pressure system. Unlike the other composite maps, however, these maps for C<sub>7</sub>3 are now quite distinct, especially for the mid-level shear (SH). Very weak shear is evident just to the south of the Snowy Mountains, over Bass Strait and extending into the

Tasman Sea. This perhaps suggests that the upper free troposphere may be important in defining the synoptic meteorology of this cluster. A more thorough analysis of C<sub>7</sub>3 revealed that a number of the days included in the composite included ‘east coast lows’ (e.g. 02 Oct. 2004 and 18 Sept. 2015; Bureau of Meteorology 2017).

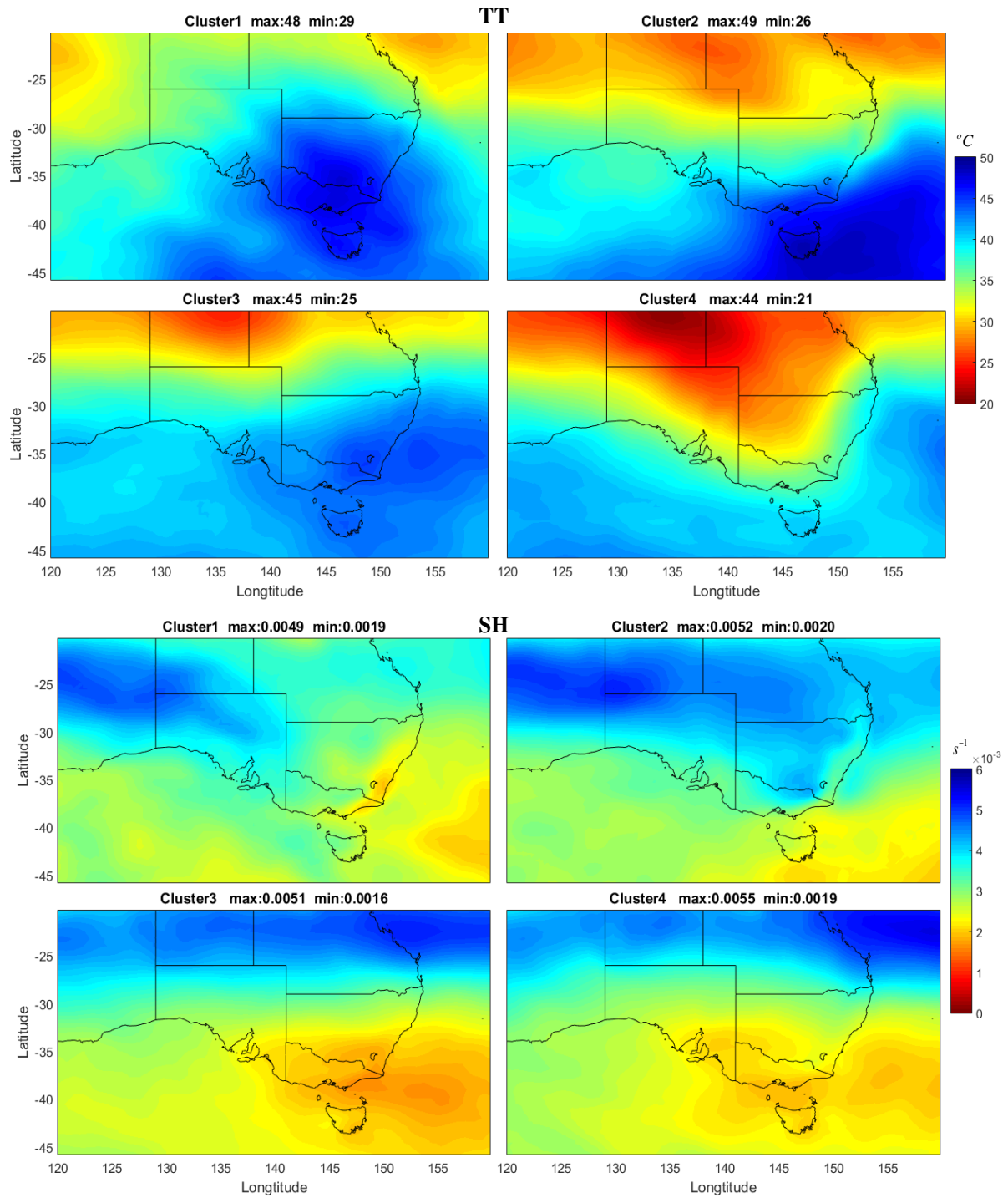


Figure 2.16 As in Figure 2.14, but showing total totals index (TT) in °C and root-mean-square wind shear between 850 and 500 hPa (SH) in 1/s.

A number of studies have diagnosed the principal synoptic types in southeastern Australia (e.g. Pook et al. 2006; Chubb et al. 2011). Specifically, Theobald et al. (2015) applied an automated approach to generate synoptic types by combining meteorological variables throughout the depth of the troposphere across the Snowy Mountains. It is interesting to compare and contrast our four wintertime clusters with their 11 synoptic types. Only a limited comparison is possible as Theobald et al. (2015) considered only heavy precipitation days (threshold of  $10 \text{ mm day}^{-1}$ ) for the full year. Further, instead of employing physical observations from a sounding site, they employed 13 variables provided from the ERA-Interim reanalysis. In spite of these substantial differences, it is evident from the composite maps that  $C_{71}$  and  $C_{72}$  correspond to Theobald clusters T5 (Prefrontal troughs; approaching cold fronts) and T1 (Embedded cold fronts). Not surprisingly, dry clusters  $C_{73}$  and  $C_{74}$  (occurring  $\sim 70\%$  of the time during the cold seasons and most frequently at the start and middle of winter) were not represented by any of the Theobald clusters, since their analysis was limited to wet conditions throughout the year.

In summary,  $C_{71}$  includes the heaviest precipitation days and the lowest  $\hat{H}^2$  values (and the highest frequency of unblocked cases). It occurs for 10% of the winter days, but accounts for 39% of the precipitation. It is associated with frontal passages.  $C_{72}$  is associated with post-frontal conditions. It occurs 22% of the time and accounts for 33% of the precipitation.  $C_{73}$  is associated with a variety of synoptic conditions. It is a dry cluster, occurring 40% of the time and accounts for 23% of the total precipitation. Finally,  $C_{74}$  is the driest cluster associated with high-pressure system dominating the region over the Snowy Mountains and to its north. This occurs  $\sim 30\%$  of the time and accounts for only 5% of the precipitation. It has also the strongest low level stability (i.e. highest  $\hat{H}^2$  values).

## **2.6 Conclusion:**

Bureau of Meteorology station data at a spatial resolution of  $0.05^\circ \times 0.05^\circ$  (Jones et al. 2009) have been previously used to investigate the relationship between precipitation and large-scale climate drivers. In the mountains of southeast Australia, this product is often too sparse or incapable of recording frozen precipitation rates greater than about 3 mm/hr (Gorman

2003). Thus, precipitation obtained from seven high-elevation gauges, operated by Snowy Hydro Ltd. (SHL) for a 21-yr period from 1995 to 2015 is used to explore the relationship between precipitation and large-scale climate drivers. A much stronger relationship between the wintertime precipitation in the Snowy Mountains and the position and intensity of the STR is found in comparison with that found across southeastern Australia (e.g. Timbal and Drosdowsky 2013). Monthly correlation coefficients (Statistically significant at the 5% confidence level) between these two components of the subtropical ridge and precipitation tend to peak in August in both the high-elevation gauges ( $r = -0.81$  and  $-0.68$  for STR\_I and STR\_P, respectively) and across southeast Australia ( $r = -0.69$  and  $-0.51$  for STR\_I and STR\_P, respectively; Timbal and Drosdowsky 2013). The SOI and IOD are found to be significantly strongly correlated with precipitation in the high elevations of the Snowy Mountains in early spring (Sep-Oct), showing a consistent interannual variability with the southeast Australia (Risbey et al. 2009).

A primary aim of this chapter has been to better understand the sensitivity of precipitation over the Snowy Mountains of southeast Australia to the low-level stability (as measured by the square of the non-dimensional mountain height,  $\hat{H}^2$ ) and to understand the relationship between the low-level stability and the synoptic meteorology, if any.

Previous research (D14) demonstrated that the precipitation over these mountains is sensitive to the large scale synoptic meteorology. Following this methodology, a K-means clustering algorithm was applied to the precipitation using six synoptic predictors (GP, TW, QU, QV, SH and TT). As before, four clusters were identified as the minimum number of clusters necessary to distinguish the precipitation distribution between clusters. Examining these more thoroughly with the use of ERA-I reanalysis data, the wet cluster (C1) was associated with frontal passages. C2 was also a wet cluster, being associated with post-frontal conditions. C4 was a dry cluster associated with suppressed (stable) conditions, and C3 was a dry cluster constructed from the remaining observations. Distributions of  $\hat{H}^2$  were also distinguished by this clustering, suggesting that  $\hat{H}^2$  was also strongly defined by the synoptic meteorology. When repeating the clustering for seven variables (the original six predictors plus  $\hat{H}^2$ ), only minor changes were observed for the two wet clusters, while changes were observed in the number and composition of dry clusters, C3 and C4.

## **Chapter 3**

### **Prediction of wintertime daily precipitation over the Snowy Mountains**

### 3.1 Introduction

Given the many challenges in numerically simulating orographic precipitation, a common practice has been to develop statistically based models to forecast precipitation as a function of some independent predictors (i.e. a regression between synoptic and/or local indicators to forecast precipitation). Statistical models are relatively simpler than NWP models; however, they do not consider the various physical processes of precipitation. Therefore, a combination of current NWP and statistical models seems to be an appropriate solution to address the above-mentioned limitations. Model Output Statistics (MOS) is a commonly used, post-processing technique to improve the skill of NWP forecasts, employing a statistical method to relate model output to observations (Glahn and Lowry 1972). Examining an ensemble NWP precipitation forecast, D14 found a significant underestimation of precipitation intensity over the high elevation terrain of the Snowy Mountains. Using their synoptic clustering, they applied a linear regression algorithm to improve the performance of ensemble precipitation forecasts, reducing the root mean square error (RMSE) by over 20% for their two wet clusters. The ensemble model, known as the Poor Man's Ensemble (Ebert 2001), combined the output of seven independent large-scale NWP models to forecast precipitation at a coarse spatial scale of  $1^\circ \times 1^\circ$  resolution.

One of the broader aims of the current research is to evaluate the performance of the high-resolution Australian Community Climate and Earth-System Simulator (ACCESS) NWP system (Puri et al. 2013) in forecasting wintertime precipitation across the high elevation terrain of the Snowy Mountains. A further aim is to test whether the method developed in D14 (based on building a statistical relationship between the variables from a synoptic classification and the ensemble forecast of rain to enhance the skill of the model in precipitation intensity prediction) is applicable to operational, higher-resolution precipitation forecasts (compared to the Poor Man's Ensemble) provided by the ACCESS model. Further, we seek to improve this clustering based MOS methodology by extending the analysis to explicitly consider the lower atmosphere stability. Limiting our analysis to the cold seasons (May – October), the main outcomes of this chapter are: i) the investigation of inter-dependences between the low-level atmospheric stability and the daily precipitation, and ii) the improvement in the accuracy of the daily NWP precipitation forecasts over the Snowy Mountains via stepwise regressions coupled with the results of the synoptic

categorization (chapter 2). Much of the work in this chapter has been published in Sarmadi et al. (2017).

### **3.2 Datasets:**

#### **ACCESS model dataset:**

In addition to the dataset presented in chapter 2, the model data examined in this study are taken from the current operational ACCESS NWP system. The atmospheric component of ACCESS is the UK Met Office Unified Model (MetUM), which is a non-hydrostatic model using a semi-implicit, semi-Lagrangian numerical scheme (Davies et al. 2005) to solve deep-atmosphere dynamics. This version of the ACCESS NWP system is referred to as the “Australian Parallel Suite 1” (APS1), which represents the first major upgrade to the system since operational running commenced in August 2010. The ACCESS-R forecasts used in our study for the two year (2014-2015) cold months (May-October) is the Australian-wide regional domain model, which covers an area of 65°S-16.95°N and 65°E-184.57°E (Figure 3.1). This model has a horizontal resolution of ~12km (0.11°) and a vertical resolution of 50 levels with the highest level at 37.5 km. Benefiting from the 4-D data assimilation, the ACCESS-R forecasts are initialized at 0000, 0600, 1200 and 1800 UTC of each day and provides hourly precipitation forecasts up to 72 hours ahead. The forecast precipitation is the sum of two components that are computed separately in the model using the convective and large-scale (i.e. microphysics) parameterization schemes, respectively. More detailed information on the ACCESS-R can be found in Puri et al. (2013). For this study, the mean value of 10 grid boxes covering the Snowy rain gauges, bounded by latitudes 35.85°-36.40°S and longitudes 148.27°-148.49°E, is employed to represent the ACCESS-R precipitation forecast over the high elevations of the Snowy Mountains. Given issues related to the model spinup, the first few hours of the ACCESS\_R simulations are neglected. On the other side, the forecast time need to be consistent with the sounding at Wagga Wagga and represents forecast for the next 24 h after sounding measurements. To address these two issues, the second day (24-48 hr) precipitation forecast is considered as the following day forecast.

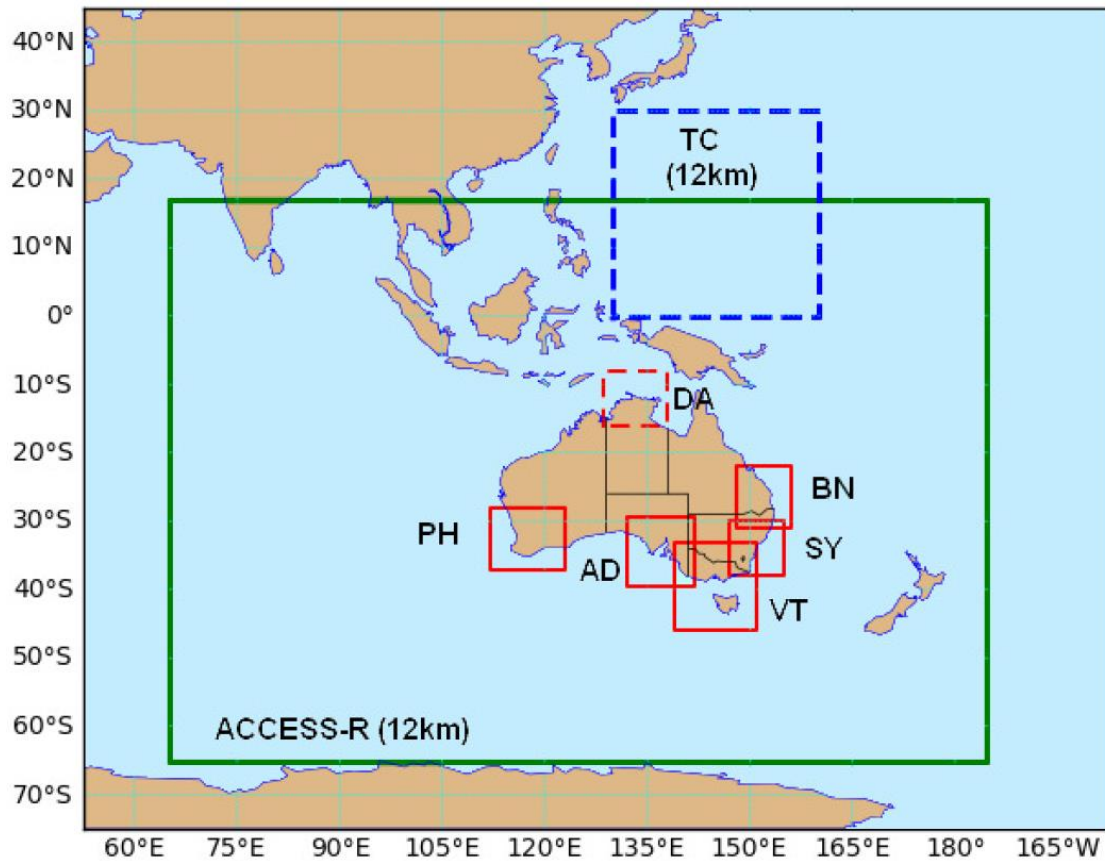


Figure 3.1 ACCESS system APS1 configuration. Source: National Meteorological and Oceanographic Centre (NMOC) Operations Bulletin Number 99.

### 3.3 Winter precipitation characteristics

Same as chapter 2, a rainy day is defined at a threshold of  $0.25 \text{ mm day}^{-1}$  for either the average SHL surface observations or ACCESS-R precipitation. A basic summary of the winter precipitation is provided in Table 3.1. Focusing on the two-year analysis period (2014-2015), the SHL surface observations show a reduction in both the frequency of rainy days and the intensity (not significant at the 5% level) compared to the 21-year climatology (1995-2015; see Table 2.1). The statistics with ACCESS-R, show that both the frequency and intensity are greater than the observed values in comparison to two-year analysis period (not significant at the 5% level), while the opposite is true for the 21-year climatology (see Table 2.1).

Table 3.1. Main statistical characteristics of daily winter precipitation in mm for rainy days (>0.25mm) for a 2-yr period (2014-2015). Numbers shown in the brackets are the ACCESS-R results.

Month	May	June	July	August	September	October	May-Oct
<b>Rainy days</b>	51%	50%	58%	55%	35%	23%	45%
<b>Frequency</b>	(55%)	(50%)	(64%)	(52%)	(49%)	(40%)	(51%)
<b>Mean</b>	8.8	10.8	8.8	6.3	6.9	8.2	8.3
<b>Intensity</b>	(8.4)	(12.0)	(9.7)	(5.4)	(7.4)	(10.1)	(8.8)

### 3.4 Methodology of cluster analysis

The main aim is to improve the daily ACCESS-R precipitation forecasts (Prec\_Acc) by combining the results of the synoptic classification with a stepwise regression. To this end, the averaged high-elevations SHL rain gauge observations are taken as the “ground truth” for this analysis. As the aim is to develop an operational MOS algorithm, the six predictors and  $\hat{H}^2$  are taken from ACCESS-R instead of the physical soundings. Note that due to operational management issues, the number of daily soundings at the Wagga Wagga station has been reduced to roughly three per week in recent years. Only 154 days are available during the two-winter period of interest at 00:00 UTC (10:00 Local Standard Time). To assess the skill of ACCESS-R in representing the synoptic regimes as observed by the physical soundings, the six synoptic indicators derived from the Wagga Wagga and ACCESS-R soundings are compared for the same time window (2014-15). The pairwise Pearson correlations between synoptic indicators showed significant correlations (at the level of 0.05) with the values of 66% (for SH), 86% (for TT), 92% (for QV), 93% (for TW), 94% (for QU) and 99% (for GP), suggesting a good agreement between the model and the observations. Based on this, the synoptic classification scheme is applied to the ACCESS\_R soundings. The results show high consistency in the frequencies of occurrence of the observed and model classes, justifying the use of the synoptic classification on the ACCESS-R soundings for deriving the regression equations. As discussed above, within a forecasting context, all variables are taken from the ACCESS\_R output, including the definition of a rain day. Model 1 is a single regression for all 366 winter days, regardless of cluster. Model

2 first classifies each day into one of the four clusters, with each cluster having its own regression.

The seven predictors and the ACCESS-R precipitation data were normalized before the regression models were developed. Model selection/complexity is an obvious problem when a large number of predictors are available. A stepwise approach (from a single constant value to quadratic combinations, including an intercept, linear terms, products, and squared terms) was applied to determine the leading predictors and the optimum regression formulation (degree of complexity within equations). Measures of accuracy (e.g. the RMSE or bias) will automatically improve as more predictors are included, but this comes at the cost of model simplicity. To balance the complexity and accuracy, the number of predictors employed was determined by minimizing the Bayesian Information Criterion, BIC, as an objective function (Liebscher 2012). The BIC is expressed as:

$$BIC = k \cdot \ln(n) - 2 \cdot \ln(\hat{L}) \quad (2)$$

where  $k$  is the number of free parameters to be estimated,  $n$  is the number of observations and  $\hat{L}$  is the maximized value of the likelihood function of the model. Further, we have considered a stepwise procedure that entails a forward selection and backward elimination algorithm. This process includes an examination of any linear dependency between predictors (also called multicollinearity) with redundant variables removed regardless of the goodness-of-fit criterion value (Curtis and Ghosh 2011).

Both regression models were cross-validated via a bootstrapping methodology with 10000 simulations to ensure that the results were statistically robust. For each simulation, 80% of the data are randomly assigned to the control group (used for deriving the coefficients) and the rest for testing.

### **3.5. Relationships between independent variables and observed precipitation**

Given that an aim of this chapter is to improve orographic forecasts of precipitation through model output statistics, it is worthwhile to examine the correlation of these predictors with the precipitation. Working with the historic data (1995-2015), QV (-0.51), QU (0.46), GP (0.46) and TW (0.43) are highly correlated with precipitation, while the stability measures

$\hat{H}^2$  (-0.24), TT (0.23) and SH (0.16) are less strongly correlated. All correlations are statistically significant, confirming our underlying premise that these variables can be of use in forecasting orographic precipitation. Table 3.2 also illustrates the cross-correlations between these variables at the 0.01 significance level. The highest significant correlation is between TW and QV (-0.55); while, the lowest significance is for SH-TT (-0.136). SH-TW and SH-QV did not indicate significant linear correlations.

Table 3.2. Cross-correlation coefficients between seven synoptic indicators. \*Bold numbers are significant correlation at significance level of 1%.

	GP	SH	TT	TW	QV	QU	$\hat{H}^2$
GP		<b>-0.283</b>	<b>-0.361</b>	<b>-0.379</b>	<b>0.223</b>	<b>-0.530</b>	<b>0.338</b>
SH			<b>-0.136</b>	-0.030	-0.019	<b>0.334</b>	<b>-0.154</b>
TT				<b>0.516</b>	<b>-0.224</b>	<b>0.149</b>	<b>-0.269</b>
TW					<b>-0.554</b>	<b>0.388</b>	<b>-0.237</b>
QV						<b>-0.297</b>	<b>0.155</b>
QU							<b>-0.249</b>
$\hat{H}^2$							

Returning to the correlation between precipitation and the seven predictors, it is worthwhile to break down the analysis to the four clusters (Table 3.3). Not surprisingly, the correlation between the precipitation and any predictor is reduced within an individual cluster defined by these predictors. While greatly reduced, the correlations of QV, QU, GP, and  $\hat{H}^2$  remain statistically significant within each of the four clusters. TW remains significantly correlated within C1, C2 and C3. SH is only significantly correlated with precipitation in C4. Table 3.3 also details the rank correlation of these predictors against the precipitation. For the three stability predictors (SH, TT, and  $\hat{H}^2$ ), the rank correlation (measures the degree of similarity between two rankings assigned to two members of a set) is greater in magnitude than the linear correlation suggesting a non-linear relationship exists between precipitation and stability. The rank correlation for  $\hat{H}^2$  is nearly as great in magnitude as that for GP, both of which are negative.

Table 3.3. Linear (Pearson) and Rank correlation coefficients between seven synoptic indicators and observed precipitation over the period of 1995-2015 (Classification results based on 7-variable clustering). \*Bold numbers are significant correlation at significant level of 5%. No Class: no classification process has been implemented.

		GP	SH	TT	TW	QV	QU	$\hat{H}^2$
C1	Linear	<b>-.206</b>	.018	-.039	<b>.176</b>	<b>-.482</b>	<b>.194</b>	<b>-.198</b>
	Rank	<b>-.261</b>	.019	.010	.063	<b>-.460</b>	<b>.143</b>	<b>-.296</b>
C2	Linear	<b>-.370</b>	.032	<b>.219</b>	<b>.197</b>	<b>-.181</b>	<b>.276</b>	<b>-.203</b>
	Rank	<b>-.400</b>	-.012	<b>.311</b>	<b>.166</b>	<b>-.161</b>	<b>.308</b>	<b>-.355</b>
C3	Linear	<b>-.288</b>	.002	.052	<b>.119</b>	<b>-.137</b>	<b>.144</b>	<b>-.180</b>
	Rank	<b>-.360</b>	.010	<b>.210</b>	<b>.124</b>	.002	<b>.218</b>	<b>-.344</b>
C4	Linear	<b>-.199</b>	<b>.114</b>	-.061	.041	<b>-.153</b>	<b>.194</b>	<b>-.098</b>
	Rank	<b>-.150</b>	<b>.151</b>	-.019	<b>-.073</b>	<b>.071</b>	<b>.161</b>	<b>-.215</b>
No Class	Linear	<b>-.464</b>	<b>.163</b>	<b>.232</b>	<b>.428</b>	<b>-.509</b>	<b>.465</b>	<b>-.237</b>
	Rank	<b>-.555</b>	<b>.186</b>	<b>.367</b>	<b>.376</b>	<b>-.231</b>	<b>.469</b>	<b>-.533</b>

To better appreciate the inter-dependencies between  $\hat{H}^2$  and precipitation, their joint probabilities are explored with the use of a copula function (Sklar 1959). Copula functions have been widely used (e.g. Drouet-Mari and Kotz 2001; Genest and Plante 2018; Nicoloutsopoulos 2005) to detect the probabilistic relationships between variables and to show that a set of variables with low correlations (even zero) may still retain complicated “tail” dependence structures. Unlike the commonly used correlation measures, copulas are invariant under strictly increasing transformations of random variables which are used for comprehensively exploring nonparametric measures of interdependence (Schweizer and Wolff 1981). Copulas are not restricted to any particular type of parametric functions (e.g. Gumbel distribution) for the marginal or the joint probability distributions (Madadgar and Hamid 2014). According to Figure 3.2A, the scatter plot and marginal histograms illustrates the relationship between precipitation and  $\hat{H}^2$  in which, in overall, large values of precipitation are associated with low values of  $\hat{H}^2$  and high values of  $\hat{H}^2$  are associated with weak precipitation. The marginal histograms further indicate that the vast majority of data are located in the range of 0.25 mm to 10 mm for precipitation and -1 to 5 for  $\hat{H}^2$ , overwhelming the “tail” observations outside this range.

Figure 3.2B and Figure 3.2C illustrate the marginal CDF distributions of  $\hat{H}^2$  (ranging from -5 to 25) and precipitation (ranging from 0 up to 100 mm) for rainy days based on the data from 1995-2015. A steep slope implies a higher density of data within a considered range; precipitation values less than 10 mm and  $-1 < \hat{H}^2 < 5$  have the highest frequency of occurrences (similar to what is concluded from the marginal histograms). Figure 3.2B and C are the main input elements used in calculating the joint probability values and copula function. The Frank copula (Frank 1979), selected as the best-fitting copula in this study, suggests that  $\hat{H}^2$  values greater than 7.8 correspond to precipitation events less than 0.6 mm, and  $\hat{H}^2$  values less than -0.3 correspond to precipitation events greater than 28.4 mm (Figure 3.2D). Conversely, low frequencies are given to pairwise events when  $\hat{H}^2$  and precipitation values are both low ( $\hat{H}^2 < -0.3$  & precipitation  $< 0.6$  mm) or high ( $\hat{H}^2 > 7.8$  & precipitation  $> 28.4$  mm) (Figure 3.2D). In summary, the copula identifies and quantifies the tail-end relationship (as previously highlighted by Aghakouchak et al. (2010) between  $\hat{H}^2$  and precipitation that was not evident in the simple correlation coefficient. An inverse, non-linear relationship between  $\hat{H}^2$  and precipitation was also suggested by the individual probability distributions of Figure 2.6 in Chapter 2.

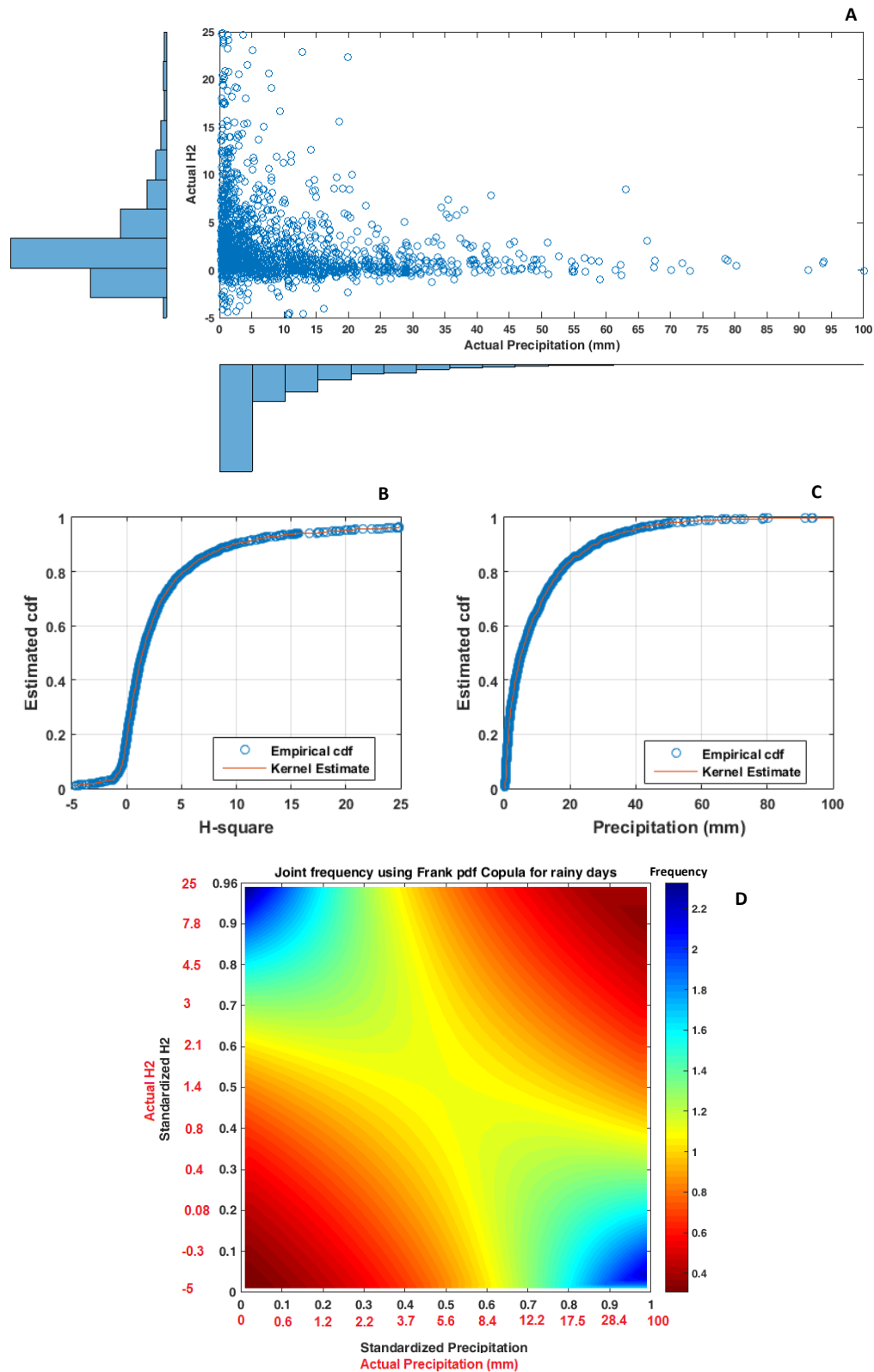


Figure 3.2. A) Histogram and scatter plot of precipitation and  $\hat{H}^2$ , B & C) the marginal CDF distributions of precipitation and  $\hat{H}^2$ . D) Joint frequency using the Frank PDF copula. All the graphs are based on the data from 1995-2015 (for rainy days).

### 3.6. Results of Daily winter precipitation forecasting

#### 3.6.1 Precipitation estimations by ACCESS-R

The daily ACCESS-R precipitation forecasts serve as our control forecast for the full two-year (2014-2015) winter (May-October) period. Table 3.4 summarizes the verification scores used to evaluate the ACCESS-R forecasts in this study. When these precipitation forecasts were evaluated against Snowy Hydro’s high-elevation surface observations, the overall RMSE was 4.20 mm with a bias of 0.3 mm. On average ACCESS-R slightly overestimated the surface observations. Looking at observed rain days only (0.25 mm day<sup>-1</sup> threshold), the hit rate for ACCESS-R was 88% with an RMSE of 6.2 mm day<sup>-1</sup> and a bias of 0.42 mm day<sup>-1</sup>. For no-rain days, the false alarm rate was 20.7% with an RMSE of 0.58 mm day<sup>-1</sup> and a bias of 0.19 mm day<sup>-1</sup>.

Table 3.4 Summary of verification scores/metrics used to evaluate the ACCESS-R forecasts in this study

Score/Metric Names	Formula
Root Mean Square Error (RMSE)	$\sqrt{\frac{1}{N} \sum_{i=1}^N (F_i - O_i)^2}$ where N is the number of observations, F <sub>i</sub> (O <sub>i</sub> ) are the forecast (observed) values.
Bias	$\frac{1}{N} \sum_{i=1}^N (F_i - O_i)$
Hit Rate	$\frac{hits}{hits + misses}$
False Alarm Ratio	$\frac{false\ alarms}{hits + false\ alarms}$
Equitable Threat Score (ETS)	$ETS = \frac{hits - hits_{random}}{hits + misses + false\ alarms - hits_{random}}$ $hits_{random} = \frac{(hits + misses)(hits + false\ alarms)}{total}$
Frequency Bias Score (FBS)	$\frac{hits + false\ alarms}{hits + misses}$
Accuracy Score	$\frac{hits + correct\ negatives}{total}$

These basic statistics can readily be broken down into the four clusters (Table 3.5). As expected, the wet ‘frontal’ cluster, C1, has the highest percentage of rain days, the greatest overall RMSE of 10.17 mm day<sup>-1</sup> and bias of 0.76 mm day<sup>-1</sup>. For rain days only, the hit rate was 97%. Over the two-years of data (no-rain days), the false alarm rate was calculated to be zero for C1. The relatively wet ‘post-frontal’ cluster, C2, shows the next highest overall percentage of hits (69%) and RMSE (5.2 mm day<sup>-1</sup>). The overall bias for C2 is 0.3 mm day<sup>-1</sup>. Most notable for this cluster is the high rate of false alarm (38%) when looking at no-rain days. ACCESS-R produces precipitation too readily in these post-frontal conditions. For the dry clusters, C3 and C4, the overall RMSE are small. They are less skilled on rain days (hit rates of 86 and 72%, respectively) and relatively skilled on no-rain days (false alarm rates of 27 and 13%, respectively).

Table 3.5. Performance of ACCESS-R precipitation estimation of observed precipitations over the period of 2014-15 with a value of 0.25 mm for the rain-day threshold. (hit, miss, false alarm and correct/negative values are in percentage)

Synoptic classes (No. days)	All days						rain days only			No-rain days only		
	Hit	Miss	False alarm	Correct/negative*	RMSE (mm)	Bias (mm)	Hit rate	RMSE (mm)	Bias (mm)	False alarm rate	RMSE (mm)	Bias (mm)
<b>C1 (34)</b>	88	3	0	9	10.2	0.76	97	10.7	0.83	0	0.03	-0.01
<b>C2 (51)</b>	69	6	10	16	5.2	0.3	92	6.0	0.15	38	1.50	0.73
<b>C3 (141)</b>	36	6	16	43	2.1	0.1	86	3.2	-0.04	27	0.41	0.2
<b>C4 (110)</b>	16	6	10	67	2.0	0.4	72	4.1	1.4	13	0.44	0.10
<b>All days ** (336)</b>	40	6	11	43	4.2	0.3	88	6.2	0.42	21	0.58	0.19

\* Correct/Negative: model correctly detects no rain days

\*\* All days: all days without implementing the classification.

More advanced metrics can readily be employed on these observations to assess the skill of deterministic precipitation forecasts, following the World Meteorological Organization Working Group on Numerical Experimentation (WWRP/WGNE 2008). For example, the frequency bias score (FBS, the ratio of the frequency of forecast precipitation events to that

of observed; where 1 indicates a perfect score) was calculated to be 1.12, and 0.97, 1.05, 1.24, 1.16 for the overall time period and then broken down by cluster, respectively. An FBS score greater than one suggests that the model generally tends to predict rain days more frequently than they are observed. The absence of false alarm in C1 led to an FBS score of just under unity, indicating the tendency to less frequently predict precipitation, however the opposite occurred in the rest of the classes.

The equitable threat score (ETS, the fraction of correctly predicted of observed and/or forecast events that has a range of -1/3 to 1, where 0 indicates no skill and 1 is a perfect score.) was calculated to be 0.49, and 0.73, 0.39, 0.41, 0.39 for the overall time period and the four clusters, respectively. The ETS accounts for correct forecasts due to chance when computing an index that combines the hit rate and the false alarm ratio. Ebert (2001) finds an ETS of around 0.4 for 21 April 1998 from the Poor Man's Ensemble precipitation predictions, suggesting that the present system is especially skilful in identifying heavy-precipitation events. The accuracy score (The fraction of "correct" forecasts) was also calculated to be 0.83, 0.97, 0.84, 0.79, 0.84 for the overall time period and the four clusters, respectively, indicating an encouraging result, with the most accurate forecast in C1.

### **3.6.2 MODEL 1: SINGLE REGRESSION MODEL**

The single regression model (Model 1) is based on only two predictors, a linear combination of the ACCESS-R precipitation forecast and QU (Table 3.6), determined by the stepwise approach and the BIC. Coefficient of determination ( $R^2$ ) values show that the ACCESS-R forecast accounts for about 70% of the variation while QU contributed roughly 14%. Having QU as a leading predictor in the single regression model suggests that the model systematic error may be rooted in misrepresentation of westerly moisture flux. Four goodness-of-fit criteria [RMSE,  $r^2$  (the coefficient of determination), the hit rate, and bias (for all days)] are calculated to quantify the improvement in using a simple regression formula from the control ACCESS-R forecast precipitation (Table 3.7).

Table 3.6 Leading predictors in regression equations for different models. ‘‘Int.’’ stands for intercept.

<b>Model</b>	<b>Leading Predictors using stepwise algorithm coupled with BIC criteria on 8 indicators</b>	<b>Regression equation</b>
<b>1</b>	QU, Prec_Acc	Y = Int. + $\alpha$ QU+ $\beta$ Prec_Acc+ $\gamma$ QU $\times$ Prec_Acc Int.= 0.290 $\alpha$ = 0.015 $\beta$ = 0.857 $\gamma$ =- 0.075
C1	TT, Prec_Acc	Y = Int. + $\alpha$ TT+ $\beta$ Prec_Acc+ $\gamma$ TT $\times$ Prec_Acc Int.= 34.718 $\alpha$ = -0.676 $\beta$ = 0.77 $\gamma$ =-0.342
<b>2</b>	C2    Prec_Acc	Y = Intercept + $\alpha$ Prec_Acc Int.= 0.495 $\alpha$ = 0.876
C3	QU, Prec_Acc	Y =Int.+ $\alpha$ QU+ $\beta$ Prec_Acc+ $\gamma$ QU $\times$ Prec_Acc Int.= 0.106 $\alpha$ = 0.723 $\beta$ = 0.865 $\gamma$ =0.084
C4	QV, Prec_Acc	Y = Int. + $\alpha$ QV+ $\beta$ Prec_Acc+ $\gamma$ QV $\times$ Prec_Acc Int.= 0.206 $\alpha$ = -0.918 $\beta$ = 0.442 $\gamma$ =-0.271

When limited to forecast precipitation days, the straight ACCESS-R forecast had an RMSE of 6 mm day<sup>-1</sup>, a bias of 0.68 mm day<sup>-1</sup>, a hit rate of 76% and  $r^2$  at 0.83 for the full two-year period (Results in Table 3.7 are different than those previously presented in Table 3.5 as the selection of rain day was changed from the surface observations to the ACCESS-R forecast to allow for an operational application). When the single regression model is applied, forecast precipitation had an RMSE of 5.6 mm day<sup>-1</sup>, a bias of -0.15 mm day<sup>-1</sup>, a hit rate of 78% and  $r^2$  at 0.85. The single regression produced a 7% reduction in the RMSE. We can examine the forecast rain days by cluster, even when employing a single regression. The single regression model improves the RMSE in all four clusters, most strongly in C4. The bias is also reduced in each of the four clusters, most strongly in C4 and C1. The coefficient of determination remains largely unchanged by cluster. The single regression does not strongly improve one or more clusters at the expense of the remaining clusters; the improvement is largely across all clusters.

### 3.6.3 Model 2: Cluster-based regression model

As stated before, Model 2 first classifies each day into one of the four clusters, with each cluster having its own regression. Linear combinations are built based on the leading predictors within each cluster (Table 3.6). The cluster-based regression (Model 2), produces an RMSE of  $4.2 \text{ mm day}^{-1}$ , a bias of  $-0.1 \text{ mm day}^{-1}$ , an  $r^2$  of 0.89 and a hit rate of 84% when computed over all days. The RMSE was reduced by 30% and the bias was reduced by 85% in comparison to the control ACCESS-R forecast precipitation.

When breaking this down into the individual clusters, large improvements are identified in C1 (24% reduction in RMSE) and C4 (42% reduction in RMSE). Further  $r^2$  increases most for these two clusters. It is important to note that all of the tested indicators have already been utilized as input variables to the clustering algorithm. For the predicted rain days in C1 (C4), a linear combination of the ACCESS-R precipitation forecast and TT (QV) is determined by the stepwise approach and the BIC. Having TT (QV) as leading predictor in C1 (C4) suggests that the model systematic error may be mostly associated with the variation of tropospheric stability (northerly moisture flux). While the gains for cluster C2 were more modest (C2 has the simplest regression fit with just having the ACCESS-R precipitation forecast as leading predictor), improvement is evident for all goodness of fit criteria. The cluster based regressions also reduced the false alarm rate (as well as improving the hit rate) in all clusters, but more strongly in the two wet ones.

Table 3.7. Goodness-of-fit criteria for different models for estimating daily winter precipitations over 2014-15 based on ACCESS-R rainy days (results are only for the test groups).

Classes	Models	Goodness-of-fit criteria				Improvement of model 1 and 2 in compare to ACCESS forecast for each criterion (%)			
		RMSE (mm)	$r^2$	BIAS (mm)	Hit rate	RMSE	$r^2$	BIAS	Hit
Overall	ACCESS	6.0	0.83	0.68	76	NA			
	1	5.6	0.85	-0.15	78	6.7	2.4	77.9	3.1
	2	4.2	0.89	-0.10	84	30.1	7.2	85.3	10.8
C1	ACCESS	10.8	0.67	1.10	90	NA			
	1	10.3	0.77	-1.30	93	4.0	14.9	-18.2	3.7
	2	8.2	0.81	-0.60	100	23.5	20.9	45.5	11.1
C2	ACCESS	5.9	0.82	0.48	90	NA			
	1	5.8	0.84	-0.34	93	2.2	2.4	29.2	2.8
	2	5.7	0.88	-0.19	100	3.9	7.3	60.4	11.1
C3	ACCESS	3.0	0.89	0.23	67	NA			
	1	2.7	0.90	-0.17	68	7.4	1.1	26.1	2.0
	2	2.6	0.91	-0.04	70	13.5	2.2	82.6	4.1
C4	ACCESS	3.9	0.62	1.70	62	NA			
	1	3.4	0.62	1.40	66	12.9	0.0	17.6	5.6
	2	2.3	0.69	-0.21	79	42.0	11.3	87.6	27.8

\*NA: Not Applicable

Histograms of goodness-of-fit criteria for the cluster-based regression model for C1 (Model 2 C1) derived from cross-validation analysis are illustrated in Figure 3.3. Due to the presence of skewness in histograms of coefficients and goodness-of-fit criteria (Figure 3.3), for all models, median of the histograms is considered and reported to reduce the influence of outliers. Similar histograms are obtained for other classes but not shown. It should be noted that the RMSE and bias histograms are derived from the normalized values of estimations, which are converted to mm for the final comparisons between the models.

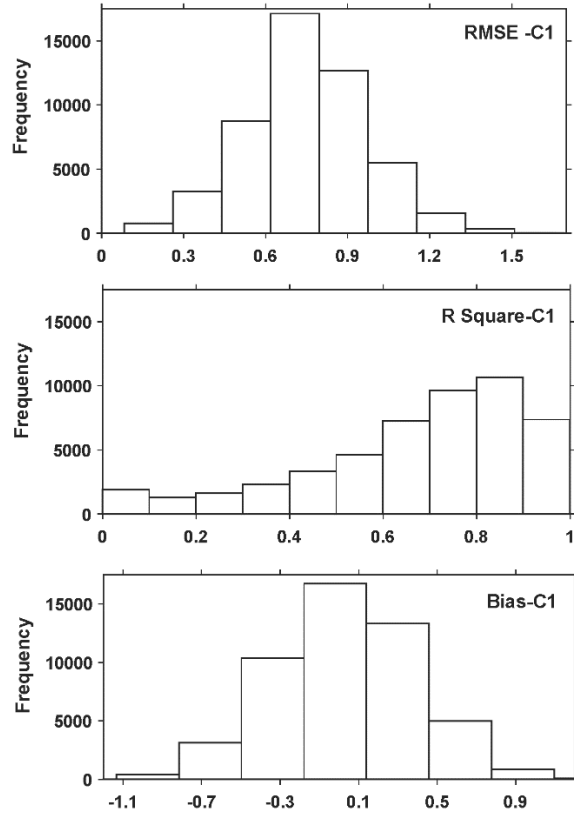


Figure 3.3. Histograms of goodness-of-fit criteria (RMSE,  $r^2$ , and Bias) based on normalized values for Model-2\_C1 derived from cross-validations with 10000 simulations. The median of each panel is taken to represent the average values in Table 3.6.

### 3.7 Conclusion:

A primary aim of this chapter has been to exploit any uncovered relationship between the non-dimensional mountain height and precipitation to improve forecasts of precipitation over these mountains for water management purposes. It has long been appreciated that orographic precipitation is sensitive to  $\hat{H}^2$  with strong stability (large  $\hat{H}^2$ ) suppressing rainfall and, conversely, weak stability enhancing orographic precipitation (e.g. Watson and Lane, 2014). An analysis of 21 years of wintertime data confirmed this relationship for the Snowy Mountains. Average  $\hat{H}^2$  was significantly greater for no-rain days (14.5) than for rain days (3.9). A rain day was defined by a threshold of  $0.25 \text{ mm day}^{-1}$ . A deeper analysis of these data found that the relationship was primarily driven by extreme values with very large values of  $\hat{H}^2$  ( $>7.8$ ) being associated with suppressed rainfall and very heavy rainfalls ( $>28 \text{ mm day}^{-1}$ ) being associated with low values of  $\hat{H}^2$ . A further investigation on the

relationship between the seven predictors (GP, TW, QU, QV, SH, TT and  $\hat{H}^2$ ) and the observed precipitation showed that they are all statistically correlated, justifying their application in forecasting orographic precipitation. Higher values in rank correlations of the stability indicators (more obviously for  $\hat{H}^2$ ) suggested a non-linear relationship rather than linear relationship.

D14 noted that over the Snowy Mountains a NWP model demonstrated more skill at predicting the synoptic meteorology than the precipitation. Thus, model output statistics (MOS) of the synoptic variables was used to improve precipitation forecasts. Two different regression models were developed with the aim of improving the precipitation forecasts of the ACCESS-R model. Specifically, the goal was to reduce the RMSE and bias. First, a single regression model was developed and applied to two-years (2014-2015 wintertime) of ACCESS-R precipitation forecasts. This led to a 7% reduction in the RMSE and a 78% reduction in the bias. Then, a cluster-based regression was applied leading to a 30% reduction in the RMSE and an 85% reduction in the bias.

The stepwise-based regression method (Curtis and Ghosh 2011) employed initially seeks a leading predictor that is able to convey a large portion of the dependent variable information (i.e. the ACCESS\_R precipitation forecasts). Following on, the regression methodology tries to select another leading predictor to further improve the accuracy of forecasts. While additional predictors will improve accuracy, they are only added if they avoid redundancy, collinearity and complexity. It is important to note that all of the tested indicators have already been utilized as input variables to the clustering algorithm. Having TT as a leading predictor in C1 suggests that the model systematic error may be mostly associated with the variation of large-scale stability. Following this logic, the model precipitation overestimation in C4 may be rooted in misrepresentation of northerly moisture flux.

## **Chapter 4**

### **Simulations of orographic precipitation in the Snowy Mountains of Southeastern Australia**

## 4.1 Introduction

The literature provides well-studied examples of long-term precipitation and the climatology of precipitation in the Australian Alpine regions (e.g. Landvogt et al. 2008; Chubb et al. 2011; Timbal and Drosowsky 2013; Theobald et al. 2015; Fiddes et al. 2015). However, there has been only a limited number of studies on quantitative short-term precipitation forecasts from numerical weather prediction (NWP) models, despite the significant progress in the implementation of increasingly sophisticated numerical models. Evaluation of the regional forecast model (on a  $0.1^\circ \times 0.1^\circ$  grid) in Chapter 3 showed that ACCESS-R, on average, overestimates the daily wintertime precipitation intensity over the high elevations. This error is, presumably, a consequence of the limited horizontal resolution in resolving the complex surface geometry or the misrepresentation of microphysical processes. Recently, Huang et al. (2018) elaborated on the estimation-forecast skill of ACCESS-VT (a higher resolution configuration of ACCESS with a horizontal grid length of 4 km over the analysis region) precipitation for two winters (May–September 2014–2015), evaluated against a high-density precipitation gauge network. They showed that the main shortcomings of the model are likely rooted in misrepresenting the key dynamical and microphysical processes. The orographic clouds of the Snowy Mountains are renowned for the frequent presence of supercooled liquid water (SLW, liquid maintained at  $T \leq 0^\circ\text{C}$ ) during winter (Morrison et al. 2013; Osburn et al. 2016). Clouds composed primarily of SLW may be sensitive to processes such as the Wegner-Bergeron-Findeisen process and ice multiplication. In a case study of two wintertime frontal precipitation events in the Brindabella Ranges to the north-east of the analysis region, Chubb et al. (2012) noted the extensive occurrence of SLW in the extended post-frontal periods. An accurate representation of such processes in NWP models remains challenging.

Efforts have been made to evaluate the skill of microphysics (MP) parameterizations in simulating clouds and precipitation associated with cold fronts (e.g. Han et al. 2013; Huang et al. 2014; Ganetis and Colle 2015; Nicholls et al. 2017), terrain-induced ascent (e.g., Lin and Colle 2009; Liu et al. 2011) and convection (e.g., Van Weverberg et al. 2013; White et al. 2017). Several studies have documented the sensitivity of simulated orographic precipitation to model horizontal grid spacing (e.g. Colle and Mass 2000; Colle et al. 2005; Smith et al. 2015; Pontoppidan et al. 2017; Grubišić et al. 2005). It has been found that finer

horizontal resolution generally improves simulation skill until the principle orographic features are satisfactorily resolved. Any further increase in horizontal resolution does not necessarily cause significant additional enhancement in model skill; however, this sensitivity is also subject to the detailed orography characteristics of the area being studied. These findings suggest that the fine model resolution alone is not sufficient to acquire skillful simulations of topographic precipitation.

Distinct from sensitivity studies on model microphysics and resolution, investigating the impact of topography on precipitation has been of great interest. Flesch and Reuter (2012) examined the sensitivity of a flooding event to the Rocky Mountains topography and reported a reduction of about 50% in maximum precipitation by reducing the elevation of the higher mountains. In a similar manner, Milrad et al. (2017) employed a series of terrain smoothing experiments using the WRF model to quantify the role of the Alberta topography in producing an extreme rainfall event as seen through ascent forcing and precipitation. They showed the precipitation pattern, intensity and associated physical mechanisms were most sensitive to a terrain reduction above 25%.

In this chapter, we present an analysis of a typical wintertime storm associated with a cold frontal passage in the Snowy Mountains of southeastern Australia. The main objectives are (1) to evaluate the skill of the simulations of precipitation and the associated meteorology over the analysis region, and (2) to explore the impact of changes in the topography, horizontal resolution and the microphysics (MP) schemes on the magnitude and spatial distribution of precipitation and associated cloud characteristics. A range of simulations are conducted address these objectives.

## **4.2 Datasets:**

### **4.2.1 High density ground-based observation:**

A well-maintained network of precipitation gauges operated by Snowy Hydro Ltd. (SHL) is used in this study for evaluation. These gauges are a combination of ETI Noah-II all-weather precipitation gauges (ETI Instrument Systems Inc. 2008) with different configurations of wind fences at high elevations and heated and unheated tipping-bucket type gauges at lower

elevations. Rain gauge data are archived at half-hourly intervals and quality controlled, based on manual corrections and equipment faults. For the model evaluation, forecasts of half-hourly precipitation and surface temperature over the study period are directly compared with data from 51 gauges across the mountains. The reliability of these data for climatological research has been previously investigated by Chubb et al. (2011, 2016). They noted the significantly better skill of this dataset in representing the orographic precipitation signal over the steep western slopes of the Snowy Mountains, when compared against the Australian Water Availability Project (AWAP) precipitation analysis. Still, an underestimate is expected for some exposed sites, particularly under snowing, windy conditions because the current data set does not take into account the wind-induced losses in observations that are common over high-elevation sites (e.g. Chubb et al. 2015).

#### **4.2.2 Satellite imagery**

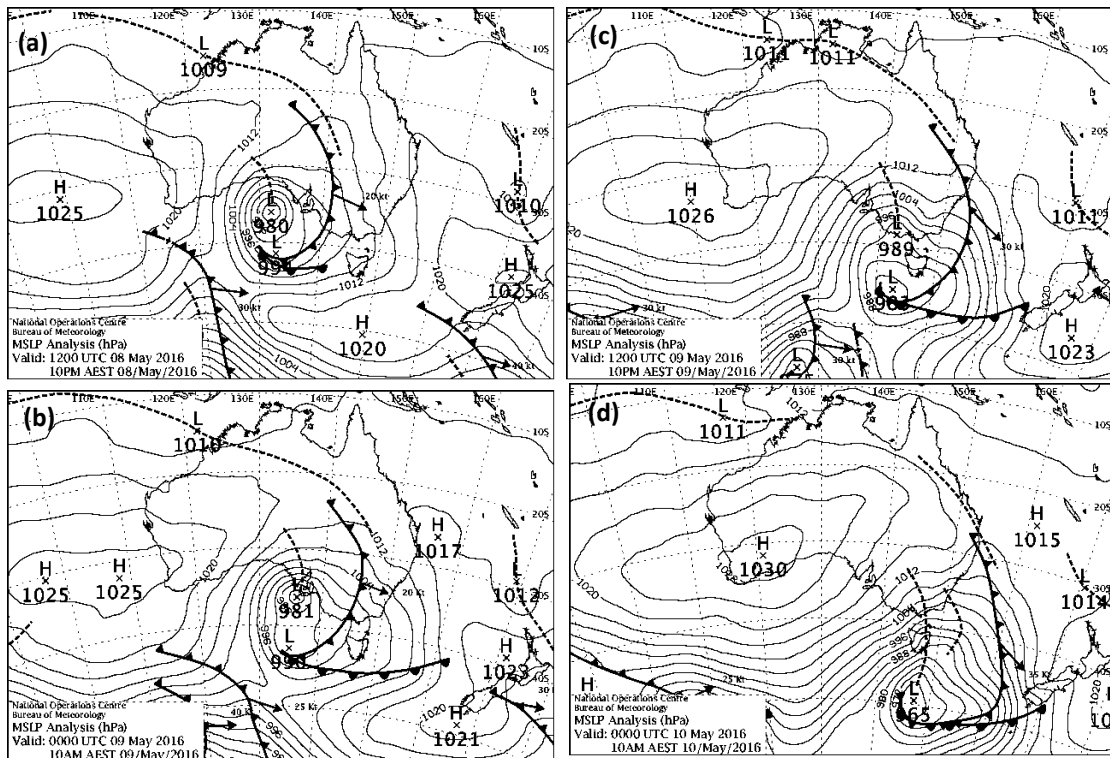
Himawari-8 is a geostationary Earth orbit meteorological satellite at 35793 km above the Earth, launched by the Japan Meteorological Agency in 2014, using new frequency bands for communication. Himawari-8 has a dedicated meteorological mission which began a new era in environmental satellites. This spacecraft carries the 16-channel (from the visible to infrared wavelength bands, covering the wavelength range between 0.47 and 13.3  $\mu\text{m}$ ) Advanced Himawari Imager instrument, which provides a better examination of the atmosphere characteristics than the previous satellite MTSAT. This instrument provides imagery that is finer in spatial resolution (0.5–2 km vs 1–4 km for MTSAT) and precision (12–14-bit images vs 10-bit for MTSAT) and higher in temporal resolutions (every ten minutes compared to hourly from MTSAT). Himawari-8 includes cloud top characteristics such as temperature and phase that are used in this study.

#### **4.3 The meteorological conditions of the case study**

Built upon the defined climatology in Chapter 2, here we present a case study that is characterized by transitioning from cluster C1 on 8 and 9 May, to C2 on 10 May, to C3 on 11 May 2016. 8 and 9 May are also associated with weak low-level local atmospheric stability (non-dimensional mountain height  $<0.5$ ), indicating that the airflow can readily pass over the terrain and mountain waves will be generated. Looking at the mean sea level

pressure (MSLP) analysis (Figure 4.1a-d) at 12:00 UTC on the 8th, a well-developed mid-latitude cyclone is present with the low pressure centre (minimum MSLP of 980 hPa) located at approximately 35°S. There is a relatively slow-moving cold front associated with this strong cut-off low, leaving the analysis region in the post-frontal field.

As shown in the Himawari-8 true color images (Figure 4.1e-f), Southeastern Australia was mostly obscured by clouds, as the cold front swept through this region. The cold front is associated with a well-defined thick frontal cloud band migrating eastward with a vividly illustrated cloud-free band behind the front and a line of convection associated with a trough. Satellite observations at 0000UTC 9 May reveal an optically thick, well-defined frontal cloud band that is heavily glaciated, which is followed by shallow orographic clouds composed primarily of supercooled liquid water in the post-frontal environment (as will be discussed later). The prefrontal sounding profile (Figure 4.4a) shows considerable moisture up to 200 hPa. The surface temperature drops by 7.5°C (from 18.5 to 11°C) following the passage of this system, leaving the analysis region in a post-frontal environment as shown by the strict westerly winds (Figure 4.4b).



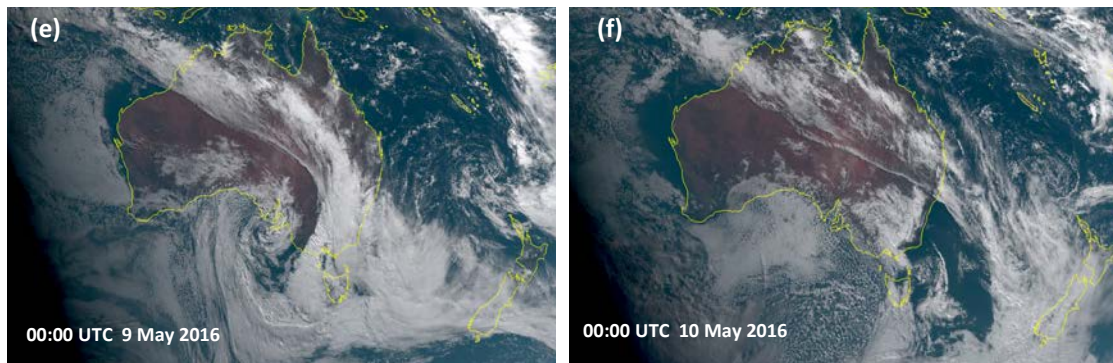
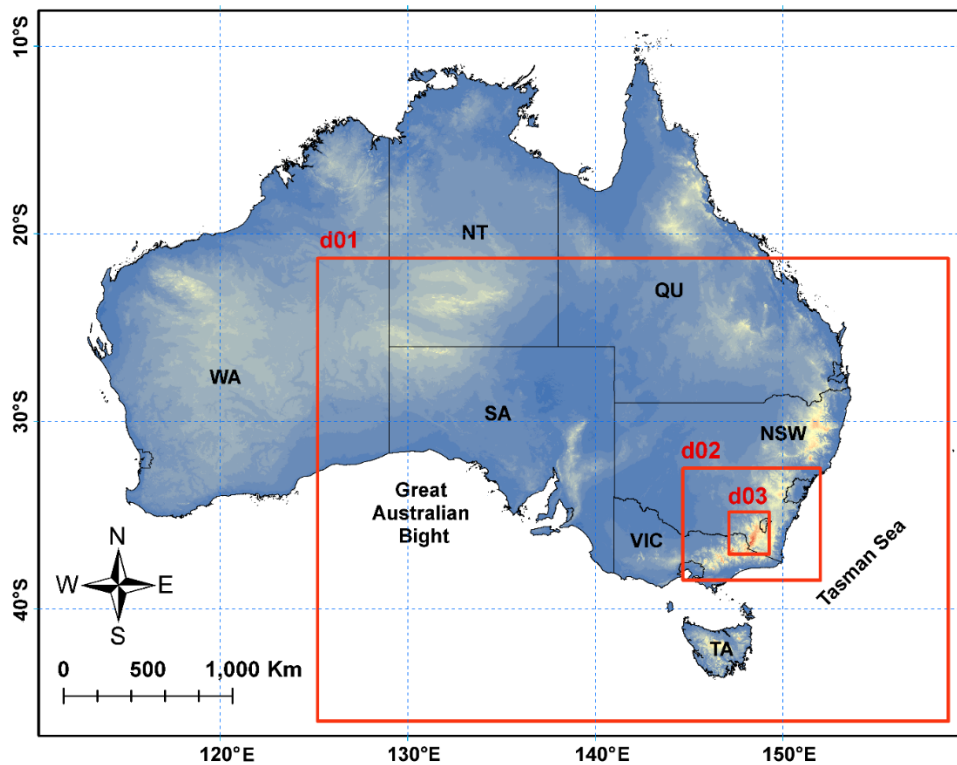


Figure 4.1 Mean Sea-Level Pressure (MSLP) analyses for May case at (a) 12 UTC 8th, (b) 00 UTC 9th, (c) 12 UTC 9th and (d) 00 UTC 10<sup>th</sup>. Himawari-8 true color imagery for (e) 00 UTC on 9th and (f) 10th May 2016 are presented at the bottom. Images are provided by the Australian Bureau of Meteorology.

#### 4.4 Model configuration

The Weather Research and Forecasting (WRF, version 3.8.1) model is used in this study. The WRF model is a sophisticated numerical model that solves the non-hydrostatic, nonlinear, fully compressible equations with a third-order Runge-Kutta scheme for time integration in a terrain-following coordinate system (Skamarock and Klemp 2008). In this study, the model is configured with exponentially increasing vertical levels (60  $\eta$ -levels with a 50 mb model top), with a vertical resolution of 20 m at the surface extending to 600 m for the upper levels, allowing 20 levels in the first 1 km. Three nested-domains with Horizontal grid spacing of 9 km, 3 km, and 1 km are utilized (Figure 4.2). The innermost domain (d03) is set up with 180 $\times$ 240 grid points covering the Snowy Mountains region. This domain was chosen given the computational expense of running high resolution simulations. However, an adequate distance to the precipitation analysis region is considered. To facilitate comparisons between the different resolution domains, feedback between the domains is switched off (one-way nesting). The model uses the daily ERA-Interim reanalysis data set (0.75 $^{\circ}$   $\times$  0.75 $^{\circ}$  grid, 21 set pressure levels, and every 6 hour updates, Dee et al. 2011) for initial and lateral boundary conditions as part of the standard WRF pre-processing system (WPS). Three days of simulation are initialized at 0600 UTC 8 May 2016 with the first 3 hour as the spinup time. The history intervals of prediction outputs are set to be 2 hours for d01, 60 min for d02 and 30 min for d03. Simulations were performed with the “Noah” land

surface model (Chen and Dudhia 2001), Yonsei University planetary boundary layer (PBL) scheme (YSU, Hong et al. 2006, first-order nonlocal) and the Goddard (Chou and Suarez 1994) and RRTM (Mlawer et al. 1997) schemes for shortwave and longwave radiation scheme, respectively. The same schemes are used for each domain, with the exception of the cumulus scheme. The Betts-Miller-Janjic (Janjic et al. 2000) cumulus parameterization was used only for the coarsest domain (d01) to represent sub-grid convection. For the control run (CTRL), the microphysics is parameterized using the Thompson semi-double-moment bulk microphysics scheme (Thompson et al. 2008), which is double-moment (prognostic mass and number concentrations) for ice and rain and single-moment (prognostic mass concentration only) for other species (i.e., snow, graupel, cloud water, and vapour). This scheme can be used in real-time NWP as it is computationally less expensive than the full double-moment schemes (e.g. Morrison et al. 2005; Milbrandt and Yau 2005). The Thompson scheme has been shown in previous studies to have promising skill in representing both supercooled and glaciated conditions within wintertime storms over complex terrains (Stoelinga et al. 2003; Morrison et al. 2010; Chubb et al. 2012). An overview of the parameterization schemes used in this study is provided in Table 4.1.



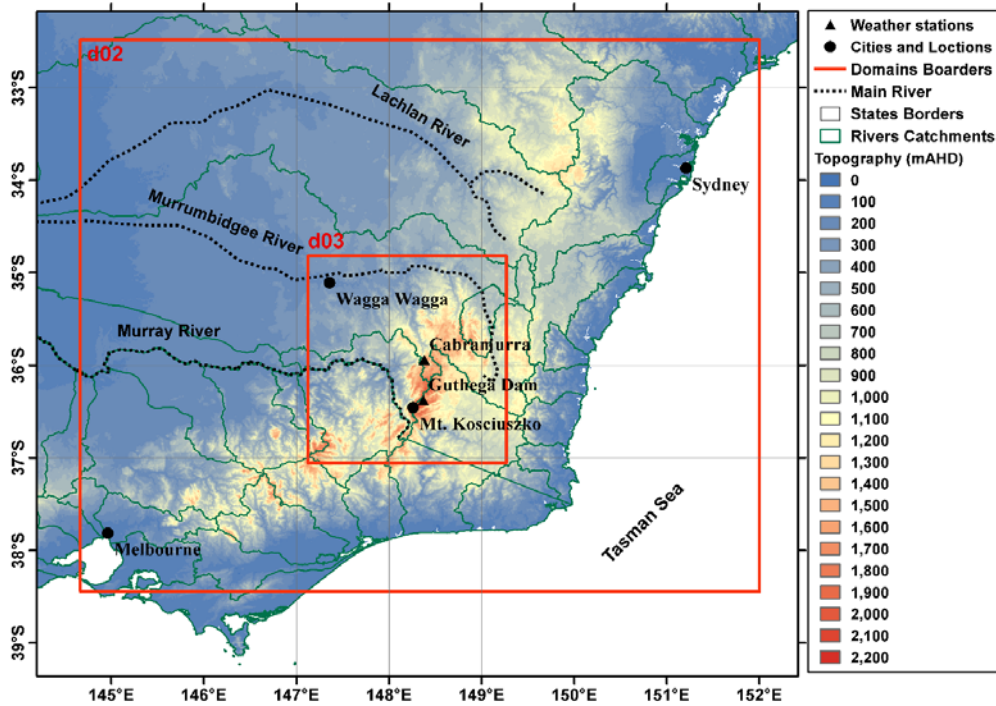


Figure 4.2 (Top) Topography map of Australia (color shaded) and the WRF three nested domains (red boxes) used in this study. (Bottom) Zoomed-in view of the two inner domains with the location of two alpine rain gauges (Cabramurra and Guthega Dam). Other features include waterways (black dashed lines), river basins (green lines) and location of the Wagga Wagga weather station.

Table 4.1 A list of configuration settings for numerical study.

Parameterisation	Option No. (d01,d02,d03)	Comments
Microphysics	mp_physics = 8,8,8	Thompson (2008) scheme
Planetary boundary layer	bl_pbl_physics = 1,1,1	YSU PBL scheme
Cumulus	cu_physics = 2,0,0	Betts-Miller-Janic (d01 only)
Land/Sea surface	sf_surface_physics = 2,2,2	Noah LSM
Short wave radiation	ra_sw_physics = 2,2,2	Goddard Scheme
Long wave radiation	ra_lw_physics = 1,1,1	RRTM

## **4.5 Sensitivity studies**

A suite of carefully designed sensitivity simulations are undertaken to investigate the impact of the dynamical and microphysical processes on orographic precipitation over the Snowy Mountains.

### **4.5.1 Microphysics run (MP)**

Wintertime precipitation simulations in complex terrain are widely reported to be sensitive to the choice of the microphysics scheme, which brings many uncertainties to atmospheric models despite significant progress during recent years (Liu et al. 2011; Pieri et al. 2015). Bulk parameterization of ice-phase microphysics is challenging given the diverse densities, complex shapes and several growth processes of ice particles (Morrison and Milbrandt 2015). In the current study, we examine the impact of a single-moment scheme versus the CTRL-run in the prediction of the precipitation and associated cloud properties over the analysis region. The single-moment microphysics scheme, implemented into the WRF model (WSM5), predicts the mass mixing ratios of five hydrometeors: rain, cloud ice, vapour, snow and cloud droplets (Hong et al. 2004). Huang et al. (2018) hypothesized that errors in the distribution of ice/snow occur over the Alps are due to the heavy presence of SLW and the single-moment MP scheme employed in the current operational ACCESS model. Considering that Thompson MP is particularly designed for SLW favorable environments in complex terrain (Stoelinga et al. 2003), the WSM5 microphysics scheme is chosen to test the hypothesis from Huang et al. (2018). The WSM5 microphysics scheme tends to initiate ice more rapidly at ice saturation from vapour (deposition growth), limiting the environment for cloud water generation. This lesser ability to capture the supercooled liquid clouds is mainly arising from misrepresentation of the number of activated crystals in their single-moment ice nuclei parameterization (Listowski and Lachlan-Cope 2017)

### **4.5.2 Topography run (TOPO)**

Given the importance of the underlying topography in the modification of orographic precipitation, the aim of this experiment is to obtain a quantitative understanding as to how

the barrier influences the precipitation amount in the analysis region. A variety of techniques can be employed to analyze such sensitivity experiments. A number of studies have compared NWP results with the actual terrain to that of eliminated terrain (e.g. Colle and Mass 2000; Wang et al. 2016), while others tried to perform experiments with reduced terrains only, using different smoothing techniques (e.g. Flesch and Reuter 2012; Schumacher et al. 2015; Milrad et al. 2017). In our experiment, we conduct a sensitivity run in which the rise above 1000 m is reduced by 75% (see Figure 4.3), as similarly done in Flesch and Reuter (2012). A threshold of 1000 m is chosen because it is the mean altitude of the Snowy Mountain region hence representing the background geography. A 75% reduction is used in order to preserve some of the topographic feature and to avoid drastic changes of topography that may induce dramatic changes in the large-scale circulations.

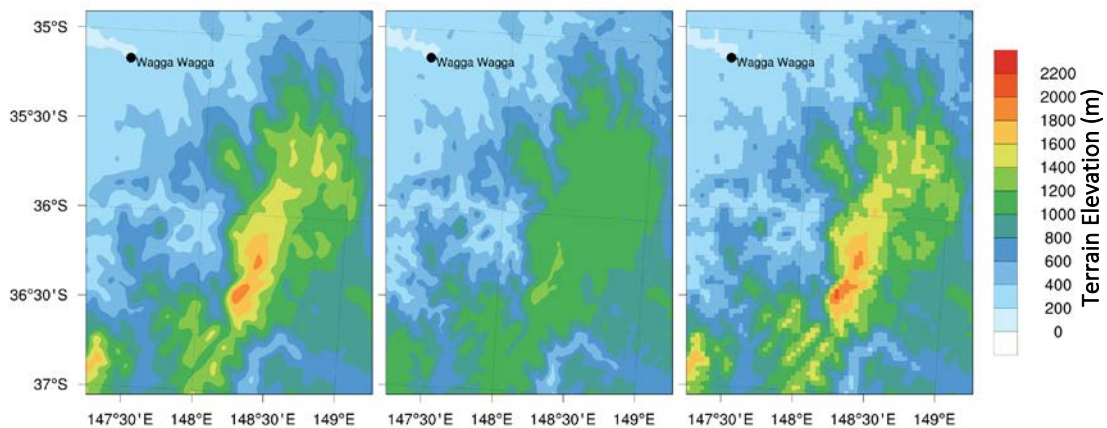


Figure 4.3 The model topography map (CTRL-run, left), the reduced-mountain topography map (TOPO-run, Middle) where rise above 1 km is reduced by 75%, and the upscaled topography map (RES-run, right) where the orography of d02 (3 km) replaces that d03 (1 km).

#### 4.5.3 Resolution run (RES)

The objective of this sensitivity experiment is to examine the influence of the fine-scale orographic details on the precipitation enhancement. Smith et al. (2015) found the Met Office Unified Model tends to simulate less cloud water and ice mixing ratios over the lower hills, leading to a reduction of the modelled rain accumulation of up to 23% by replacing the orography with coarser resolution models (1.5 km grid spacing replaced with 40 km). To quantify the effect of the resolution, the orography of d01 (3 km) replaces that of d03 (1 km)

while everything else remained unchanged. In this way, the highest model peak in d03 is slightly reduced, dropping from 2088.04 to 2085.22 meter (see Figure 4.3, right).

## **4.6 Evaluation of Control Run**

In this section, the simulated synoptic and the surface features are first evaluated by comparing the results of the CTRL-run, against the observations. The CTRL-run is found to correctly simulate the transition of synoptic clusters from C1 on 8 and 9 May 2016, to C2 on 10 May, to C3 on 11 May 2016 as seen through the sounding profiles characteristics. For example, the simulated surface pressure at Wagga Wagga station is found to increase from C1 on 8 and 9 May 2016, to C3 on 11 May 2016 with a wind shift from northwesterly to westerly component. Low-level and tropospheric stability values are also well simulated, which suggest the correct transition of synoptic clusters.

### **4.6.1 Upper Air Profile**

Figure 4.4 shows the observed soundings (black) from the closest upwind site of the BoM to the Snowy Mountains (Wagga Wagga weather station located at 180km to the northwest) and the simulated atmospheric profile (red) at the nearest grid point in the 1 km domain. A buffer region of 30 grid points along each border was provided between the domain boundary and the precipitation analysis region. The simulated sounding (Figure 4.4a), roughly coinciding with the passage of the cold frontal system, has a good agreement with the Wagga Wagga sounding at 0000 UTC 9 May. With a time adjustment (lead) of half an hour, the model well captured both wind speed and direction throughout the profile with an exception of the wind direction in the lowest 2km. The simulation does a good job in predicting the cloud base height and surface temperature (within  $\sim 1^{\circ}\text{C}$ ); however, the simulation fails to reproduce the inversion and the multilayer structure at lower levels, which may partially be attributed to the limited vertical resolution of the simulation. The sonde stopped reporting data above 250 hPa. The westerly wind profile during the post-frontal environment is well captured by the WRF simulation (Figure 4.4b). The evolution of large-scale synoptic pattern, as seen through MSLP charts, is well simulated by WRF in terms of both the location (e.g. Approximately  $35^{\circ}\text{S}$  on 8 May 2016) and the magnitude (both around 980 hPa on 8 May 2016) of the low surface pressure system (not shown).

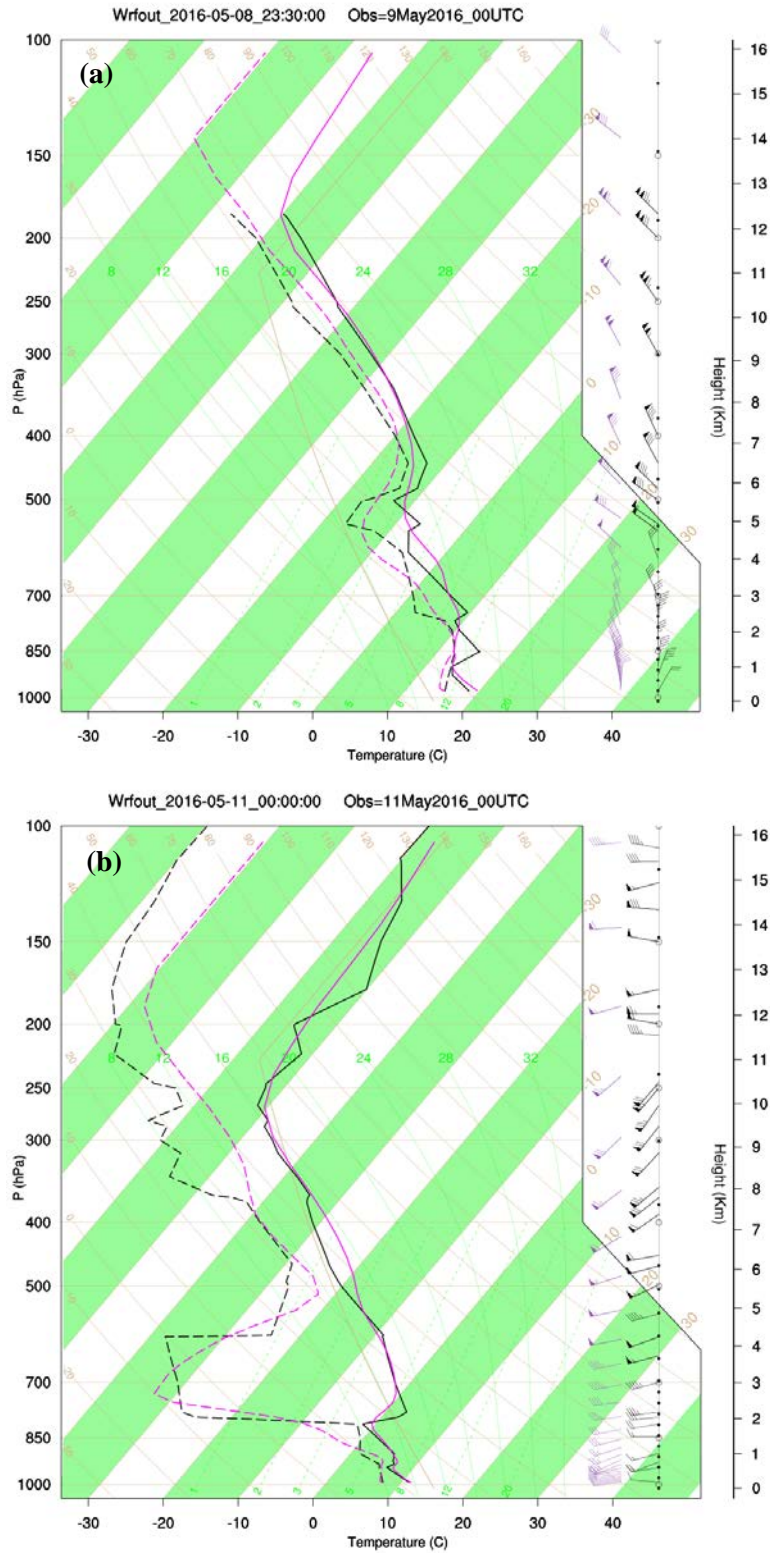


Figure 4.4 Comparison of the observed upper air soundings from the Wagga Wagga weather station (black lines) alongside 1 km WRF simulations from the nearest grid point to Wagga Wagga station (red lines) on 9 of May, 2016 at 00:00 UTC (a) and 11 of May, 2016 at 00:00 UTC (b).

#### 4.6.2 Surface Precipitation and Temperature Evaluation:

Time series of observed precipitation and temperature from two gauges along the main ridge line (Cabramurra and Guthega Dam, see Figure 4.2) are directly compared to the WRF simulations (9 km, 3 km and 1 km) to confirm the timing, the rate of precipitation and the impact of the grid resolution (Figure 4.5, top plots). Different precipitation episodes, apparent by the varying slope of the curves, relate to the synoptic situation as illustrated in the MSLP charts. The first jump (in light blue shade) in precipitation occurred when the cold front passed through in the early hours on the 9th, bringing about 20 mm precipitation during a 3-hr period. The second jump (in dark blue shade), separated by a dry period (in yellow shade) of about 8 hour, was associated with a trough that brought about 50 mm precipitation during 12 hours at Cabramurra and 80 mm during 18 hours at Guthega Dam. Shaded areas correspond to different precipitation episodes. The timing of the precipitation onset is generally in good agreement with the simulated precipitation, despite the 1-hour lag. Comparing precipitation from the three domains with different grid resolutions shows that the inner-most domain (d03) agreed best with the observations, particularly towards the end of the integration time. However, a slight underestimation was persistent throughout the simulation. This result is consistent with the previous studies using different models in other mountainous regions (e.g. Colle and Mass 2000; Grubišić et al. 2005; Rögnvaldsson et al. 2007; Smith et al. 2015) that found only a marginal improvement in the model performance by decreasing the grid spacing, once the principal orographic features are resolved. Note that, potential biases arising from comparing precipitation observed at individual surface sites over complex terrain with “gridded” precipitation cannot be ruled out.

Looking at a time series of the surface observations of temperature (Figure 4.5, bottom plots), a sharp drop (from 12°C to 6°C in three hours) is seen at approximately 04:00 UTC, suggesting the passage of the main front. The onset of this drop in surface temperature has a lag of about 2 hours in the simulations. The simulated temperatures were about 1 to 2°C colder than the observations. It is worth noting that the accuracy of the simulations was similar across the other high-elevation SHL sites. The 1-hour difference in lag between the observed rainfall and the temperature suggests that there is prefrontal rain. Also noted is a difference in timing in the simulated surface temperature at the Wagga Wagga sounding site and the SHL observations. The 2-hours lag in the mountains compare with the half an hour

lag upwind at Wagga Wagga can potentially show that the mountain is slowing down or changing the direction of the actual passage of the front in the model. In other word, it is plausible that the simulation shows a greater impact of the mountain ranges than was observed.

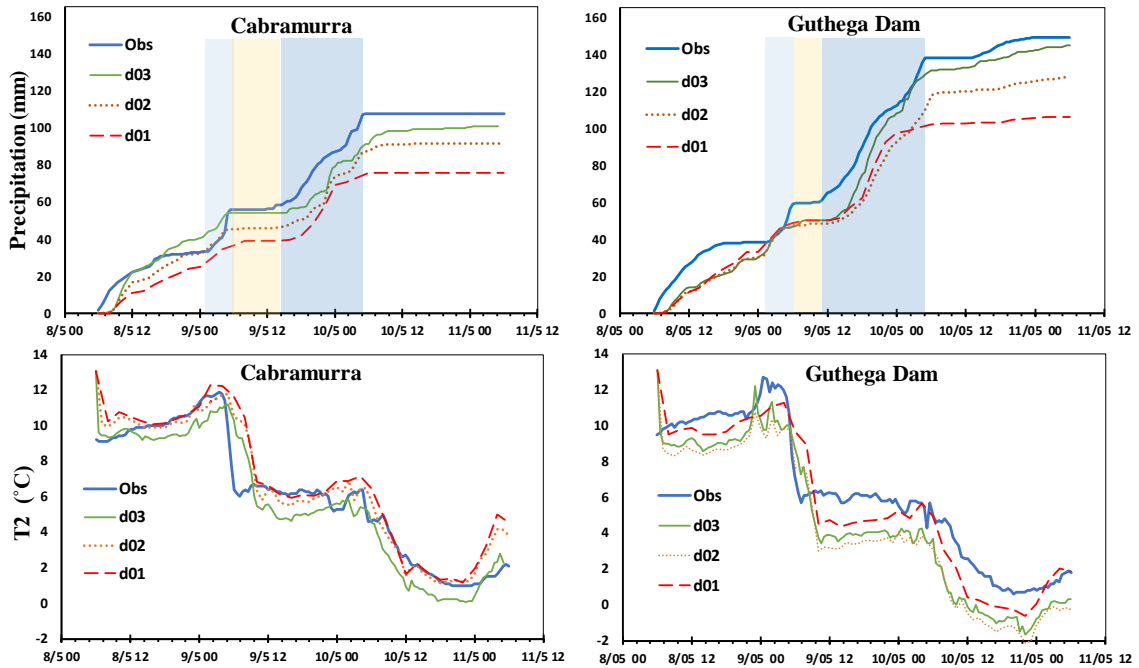


Figure 4.5 Time series of the observed surface accumulated precipitation (top panels, solid blue lines), 2-m temperature (bottom panels, solid blue lines) measurements of Cabramurra and Guthega Dam with the WRF d01 (9 km, dashed red lines), d02 (3 km, dotted brown lines) and d03 (1 km, solid green lines) outputs from the nearest grid point to the sites. Shaded areas correspond to different precipitation episodes.

Figure 4.6 shows the spatial distribution of observed and modeled accumulated precipitation. The colours show the 69-hr accumulated precipitation from CTRL-run, overlaid with that observed by rain gauge stations shown as filled circles using the same colour scale; grey lines show the topography used in the simulations. The nearest grid point to the SHL rain gauges in WRF simulation is used for the comparison. The orographic signature, as seen through the correlation between the precipitation values and topography, is detectable in both the observed and simulated precipitation. The overall mean of the

accumulated precipitation from the gauges against the CTRL-run forecast agree well (both about 62 mm) with a bias of -1.2 mm. Perhaps the most striking feature is the negative bias (underestimate) at a number of sites, generally located along the lower slopes and just immediately upwind (western) of major peaks. This bias in the upwind can be an underestimate of up to 70 mm for the 69-hr accumulated precipitation. In summary, the good performance of the CTRL-run justifies consideration of the sensitivity runs. Potential reasons for the upwind bias will be explored through the sensitivity runs, particularly the MP-run.

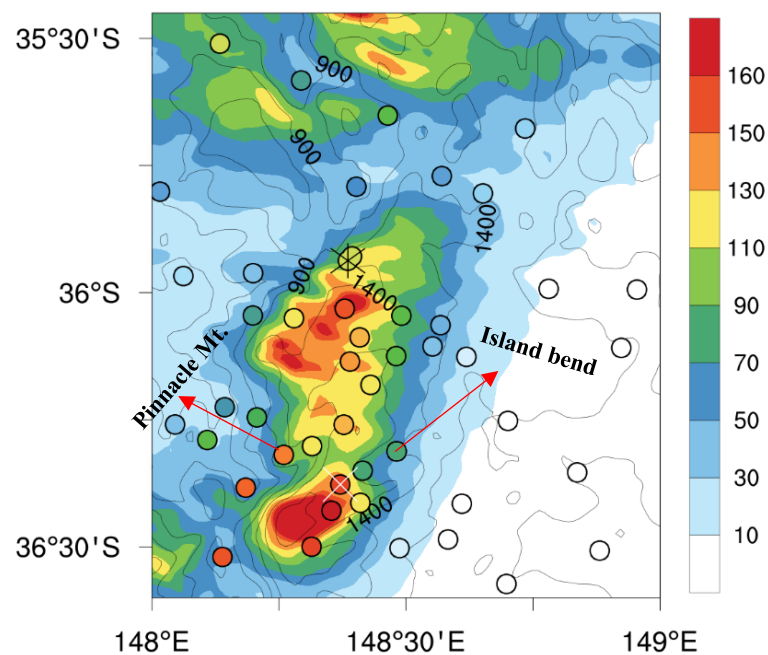


Figure 4.6 The 69-hr accumulated simulated precipitation amounts (in mm) from 1km resolution with CTRL-run (Thompson MP), overlaid with the model topography (black contours from 400 to 2400 m by 250m-interval). Filled circles show the SHL observations using the same colour scale. Black asterisk and white cross mark the location of two precipitation gauges at Cabramurra and Guthega dam, respectively.

Taylor diagram (Taylor 2001) of the 69-hr accumulated precipitation at the 51 SHL rain gauge stations (Figure 4.7) illustrates how well the simulations compare with the observations, as measured by the Pearson correlation coefficient, the root-mean-square error

(RMSE) and the standard deviation. The standard deviation as an indicator of spatial variability amongst the stations, for d01 with 9 km grid spacing (about 32 mm) is clearly underestimated compared with the observed standard deviation (about 42 mm); however, this value is just slightly underestimated in d03 (about 44 mm) and more strongly in d02 (about 46 mm) compared with the observations. Looking at the RMSE and the correlation values, the 1 km control simulation performs the best (20.8 mm and 0.89, respectively), while the other two simulations (3 and 9 km) are comparable (~25 mm and ~0.84, respectively). Overall, the high-resolution run, d03, agrees best with the observations, and the 3 km simulation is slightly less skillful. This result is similar to the finding of Pontoppidan et al. (2017) who found the same response from their three nested WRF domains with the same horizontal resolution as this study.

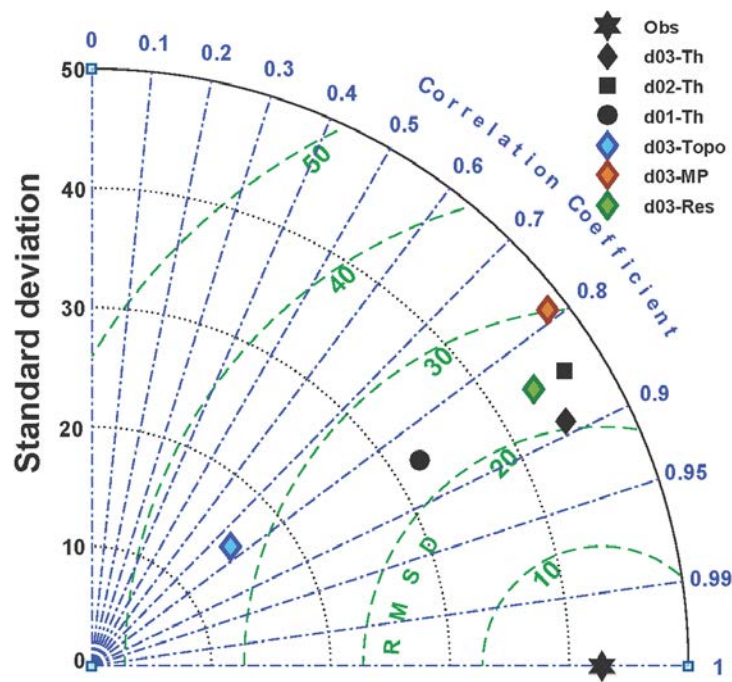


Figure 4.7 A Taylor diagram based on the 69-hr precipitation at the 51 stations for d01 (black circle), d02 (black square), d03 (black diamond) CTRL-run simulations, along with the observations marked as a star for reference. The TOPO-run, MP-run and RES-run from the 1 km simulations marked as blue, brown and green diamonds. Correlation coefficients are in blue contours. Dashed-green solid-black contours indicate the RMSE and standard deviation values, respectively.

#### 4.7 Sensitivity Study:

Figure 4.8a shows the time series of the observed accumulated precipitation averaged over all precipitation gauges along with the WRF precipitation forecast for the CTRL-run and the three sensitivity runs. Overall, all simulations correctly generate the two periods of heavy precipitation as shown in the observations. The MP-run produces similar accumulated precipitation to that from CTRL-run until the end of the dry period, where it starts to diverge and constantly simulate more precipitation by about 9%. The greater precipitation from the MP-run is in better agreement with the observations during this period. Potential reasons for this feature will be explored in more details through the MP-run.

While the accumulated area-averaged precipitation is only slightly changed in the MP-run and the RES-run, a strong reduction is apparent in the TOPO-run, indicating the major role of terrain in the development of orographic cloud and precipitation during the period of simulation. This feature can also be seen from the boxplots of total precipitation at all SHL sites over the three days of simulation (Figure 4.8b). This comparison explains the important aspect of the terrain in the production of orographic precipitation in this case. In other words, it highlights the higher impact of the peak heights in comparison with the valleys and ridges that have been smoothed out in the RES-run.

Time series of accumulated precipitation from an upwind site (west) and a downwind (east) site of the main ridge line (Pinnacle Mountains and Island Bend, respectively; for location see Figure 4.6) are also compared (Figure 4.8c-d), showing much more precipitation is produced by the MP-run on the immediate upwind and downwind sides. Huang et al. (2018) suggested that the single-moment three-phase bulk MP scheme in ACCESS (Wilson and Ballard 1999) glaciated too quickly, which led to overestimation of precipitation on windward of the Snowy Mountains. The opposite feature is true for the CTRL-run, where the underestimation of precipitation is occurred in both upwind and downwind sides. This underestimation is likely due to higher concentration of SLW in the CTRL-run, which leads to longer cloud lifetime and lower precipitation rates, compared to the simulated ice clouds in the MP-run (Raubert and Grant 1987). It can be seen that the contrast in the accumulated precipitation between the upwind and downwind sites is much weaker in the MP-run, compared to the CTRL-run and observation.

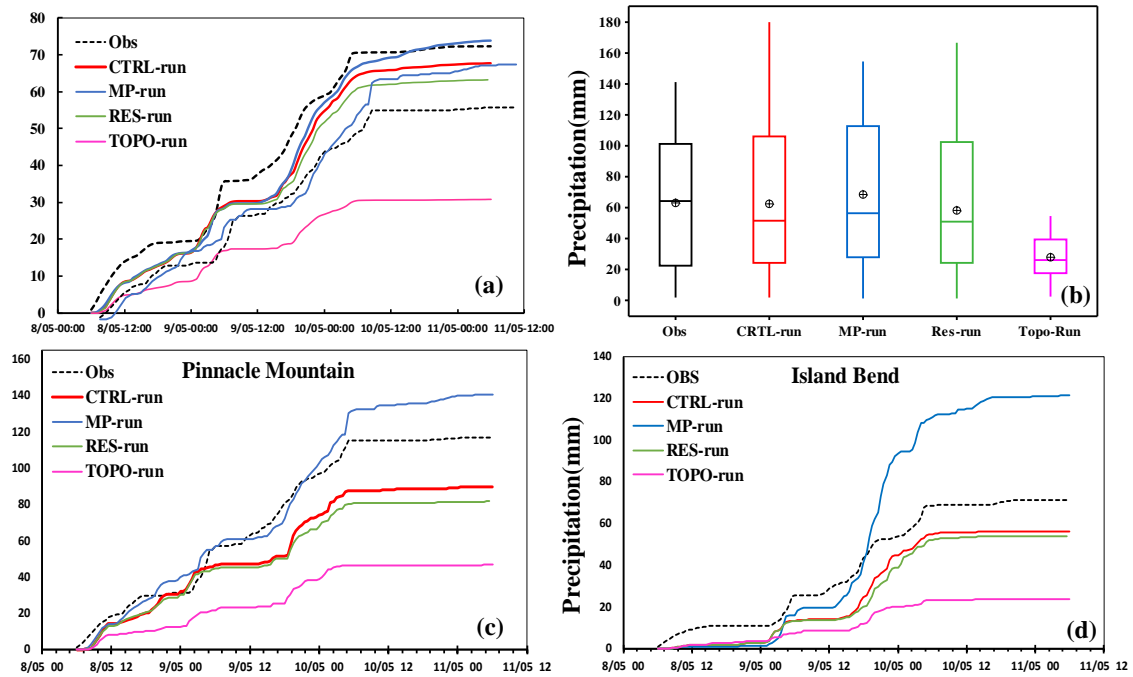


Figure 4.8 (a) Comparison of total accumulated observed and simulated precipitation averaged at all SHL rain gauge sites. (b) Boxplots of the total observed and simulated accumulated precipitation at the rain gauge sites for a 69-hour period. The first and third quartiles of the associated data represent at the top and bottom of the boxes, respectively. The 5th and 95th percentiles are shown by the start and end of the whiskers. The unfilled circles inside the boxes are the mean values. Time series of the observed surface accumulated precipitation measurements of (c) an upwind site of Pinnacle Mountain and (d) and a downwind site of Island bend.

Comparing the spatial distribution of the observed precipitation to that from the nearest grid points of the sensitivity runs shows that, generally speaking, there is a weak sensitivity in the broad pattern of the spatial distribution of precipitation accumulations to the microphysics scheme employed (Figure 4.9b), except where the terrain is steep and complex. This feature can be also seen from the time series of precipitation at both an upwind and downwind sites (Figure 4.8c-d). The precipitation average at all sites tends to be overestimated by 10% with an overall mean and bias of 68 and of 5.5 mm, respectively. The precipitation magnitude and spatial distribution in the TOPO-run differ significantly from observations with an overall reduction of 56% from 62 to 27 mm and a bias of -34 mm

(Figure 4.9c). By reducing the rise above 1 km, the approaching flow continues to pass over the less-impeding ridge and generate more precipitation in a band along the eastern slope, which weakens the rain shadow effect far downstream (south-eastern sides) of the ridge. A similar finding was reported by Flesch and Reuter (2012) when analyzing the sensitivity of the precipitation features of a flooding event to reduction in the Rocky Mountains topography.

They also found that the synoptic feature can also be affected by the reduced mountain topography, where weaker pressure perturbation along the windward slopes generated and shifted the surface low. Replacing the orography of d03 (1 km) with that used by d02 (3 km) does not change the overall spatial distribution associated with the orography; however, the average at the gauge sites has decreased by 8% from 62 to 57 mm with a bias of -4.8 mm (Fig. 7d).

The Taylor diagram (Figure 4.7) also shows the basic statistics for the sensitivity runs. Comparing the observed statistics marked as a star for reference with that of the sensitivity runs reveals that the RES-run (marked as a green diamond; RMSE = 23.6 mm and  $r = 0.85$ ) is in a relatively good agreement with the CTRL-run (marked as a black diamond; RMSE = 20.8 mm and  $r=0.89$ ), with a slightly lower correlation coefficient and higher RMSE. The MP-run shows a poorer correlation and overestimation of both the RMSE and standard deviation by roughly 10 and 4 mm, respectively, in comparison with the CTRL-run. Finally, the TOPO-run shows the highest RMSE and a poor correlation with observations.

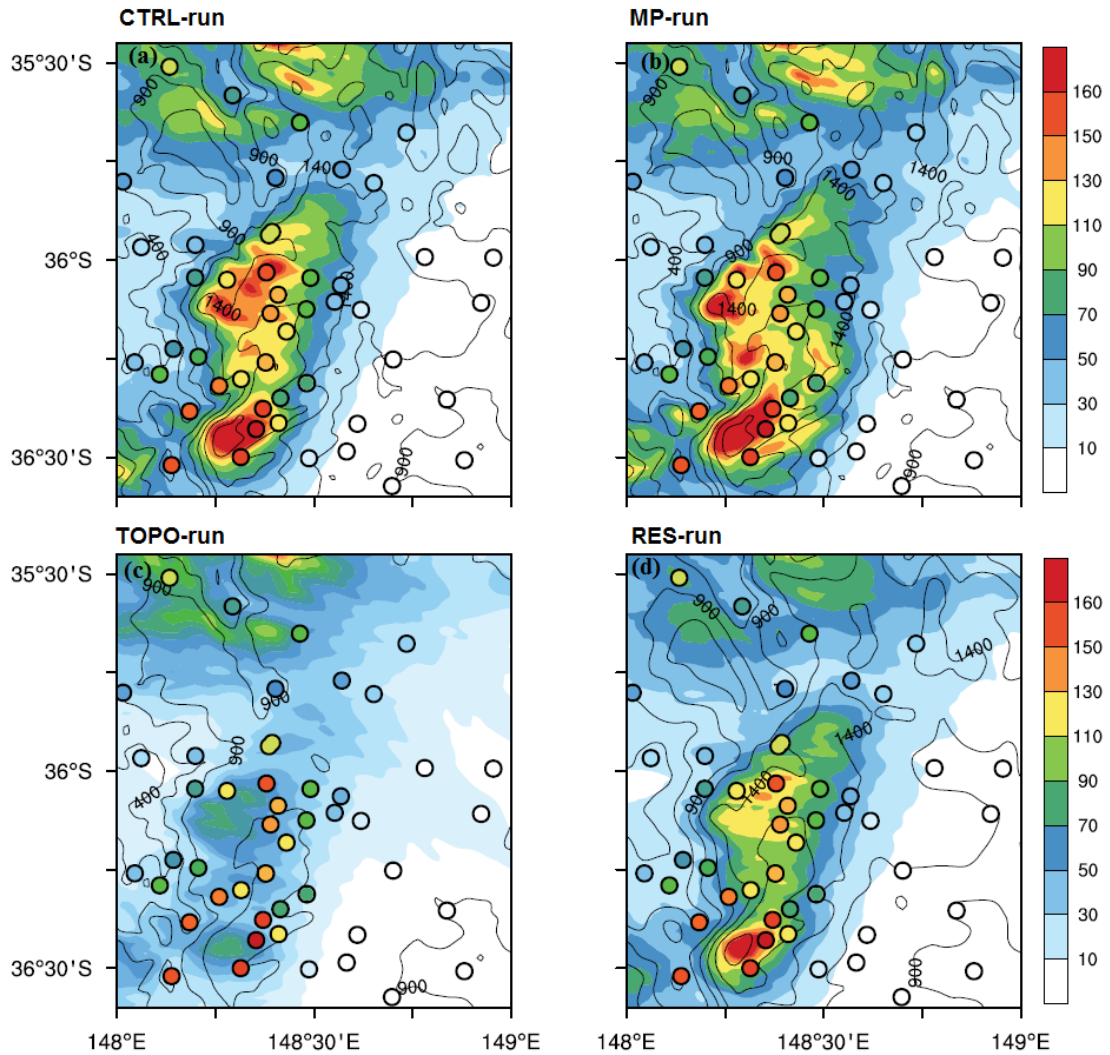


Figure 4.9 The 69-hr accumulated simulated precipitation amounts from 1km resolution with (a) CTRL-run (Thompson MP) (b) MP-run (WSM5 MP) (c) TOPO-run, and (d) RES-run, overlaid with the model topography (black contours from 400 to 2400 m by 250m-interval). Filled circles show the SHL observations using the same colour scale.

Figure 4.10 compares the difference in accumulated precipitation between CTRL-run and the three sensitivity runs. Looking at the first plot (Figure 4.10a), the precipitation features of the single-moment MP run differ from those of the CTRL simulation using the Thompson MP scheme. Although the broader pattern is similar in MP run (see Figure 4.9a-b), a much stronger influence is evident at high elevations to the choice of MP schemes as seen in Figure 4.10a and d. While the domain-average precipitation has just marginally changed

(from 31.5 to 33.5 mm, leading to about 6% increase), the precipitation spatial distribution has been clearly affected with less precipitation over the mountain peaks and more precipitation over the windward and more clearly over lee slopes (with stronger relative difference, Figure 4.10d) where topography gradients are sharp. This result can be compared with that of Liu et al. (2011), who found that the WSM5 MP scheme generates greater precipitation than Thompson MP scheme (~22%) over the 3-month (Dec-Feb) total precipitation in the Colorado Rocky Mountains. They further noted that the WSM5 MP scheme produced more precipitation in the upslope region (similar to what we found here), but less precipitation in the lee-side that is in contrast to our results. They believed that the higher precipitation efficiency in this single-moment MP scheme had likely caused the western sides differ from the eastern sides of the mountains over the Colorado Headwaters Region. Our result is also consistent with the findings of recent model evaluation study of two cold seasons (May-Sep, 2014-15) precipitation forecast that the single-moment scheme overestimates the total precipitation over the western slope of the Snowy Mountains (Huang et al. 2018).

Looking at the second plot (Figure 4.10b), the major differences occur at high elevations, where the maximum accumulated precipitation dropped from 224 mm to 64 mm with relative difference of over 100% (Figure 4.10e), where the topography has been most suppressed. The domain-average precipitation dropped from 31.5 to 23 mm, giving a 27% reduction in precipitation. This result shows good agreement with Flesch and Reuter (2012), who studied the sensitivity of the precipitation features of a flooding event to reduction in the Rocky Mountains topography. They found the most (least) sensitivity to topography in the precipitation over (outside) the mountains as a consequence of a decrease in orographic lifting over the reduced-mountain terrain.

Much less sensitivity in precipitation is observed by just replacing the orography of d02 by that of used in d03 (Figure 4.10c and f). Making the underlying topography three times coarser while everything else is kept the same, mostly affects the precipitation on the mountain peaks along with the steepest windward slopes which leads to slight reductions of about 6% and 4% in the maximum and area-average of the accumulated precipitation, respectively. This result is consistent with Smith et al. (2015) who assessed the skill of the Met Office operational weather forecasts. They found that replacing the 1.5 km orography

with that used in the 4 km model, only reduces the area-averaged precipitation by 5%. They further concluded that the precipitation overestimation of 4 km model (~18%) over the hills cannot be related to the representation of the orography.

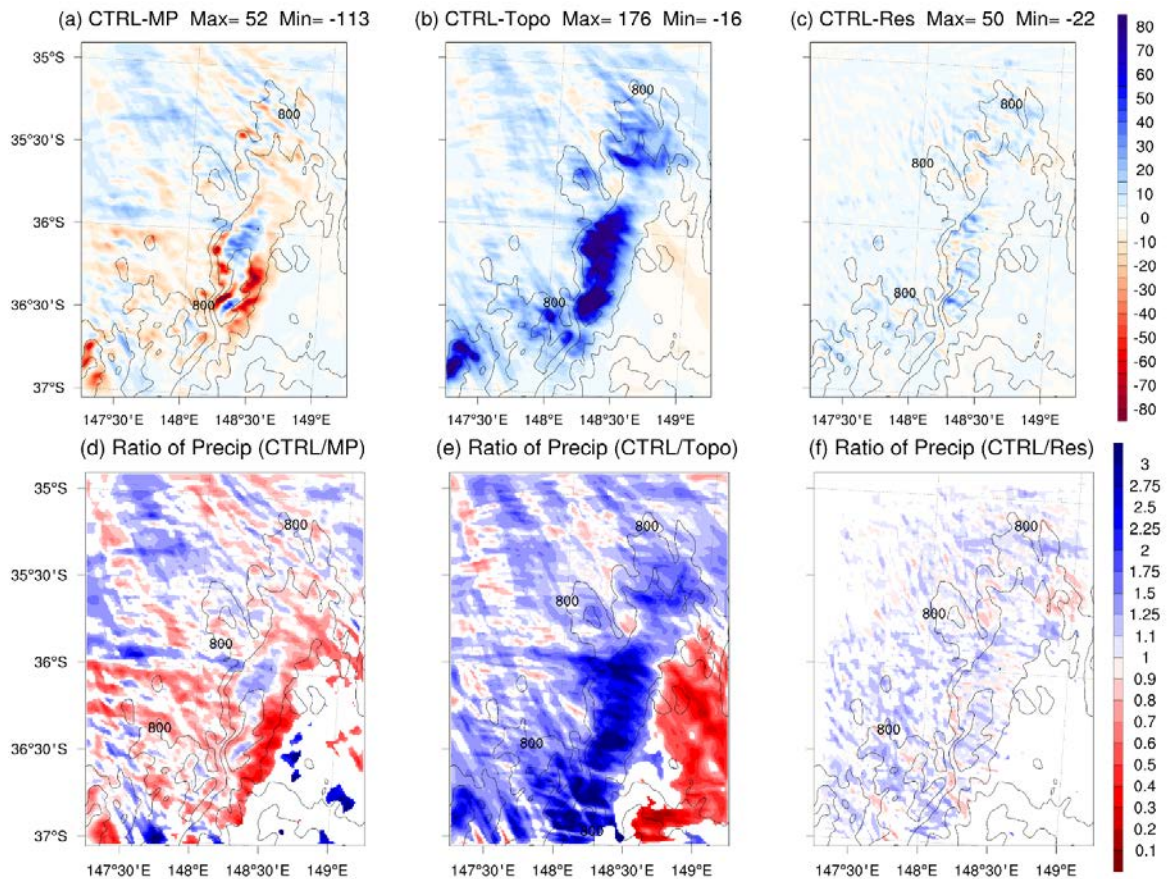


Figure 4.10 Differences in accumulated precipitation (mm, shaded) overlaid with the model topography (black contours from 800 to 2200 m by 400m-interval), between the WRF 1-km for a 69-hour period (0009 UTC 8 May to 0006 UTC 11 May 2016) for (a) CTRL-MP run; (b) CTRL-TOPO run; (c) CTRL-RES run. The maximum and domain-averaged precipitation differences are shown on top of the individual panels. Bottom panels show the ratio of the precipitation amounts from the CTRL-run to that from (d) MP-run, (e) TOPO-run and (f) RES-run.

Figure 4.11 shows the Hovmöller-type plots for differences of half-hourly precipitation rate for a 72-hr period through latitude 36.4°S over the southern peak of the Snowy Mountains to better appreciate the evolution of the simulated precipitation as the synoptic system

progressed eastwards. Looking at the Figure 4.11b, it can be seen that single-moment MP scheme tends to predict more precipitation on the both western and eastern slopes and less precipitating over the peak (the peak elevation is located at 148.3°E), where the topography gradient is sharp. Terrain reduction leads to less precipitation over the peak (Figure 4.11c) particularly during the second period of the heavy precipitation. Similar but weaker reduction features can be seen in RES-run (Figure 4.11d). The onset of two precipitation periods (see Figure 4.8a) and the spatial distributions of the heavy frontal precipitation (excluding TOPO-run) are generally in good agreement in the CTRL-run during the early hours of the 9th of May 2016. This precipitation patterns start to diverge from the second period of heavy precipitation during the post-frontal period (the second jump in Figure 4.8a).

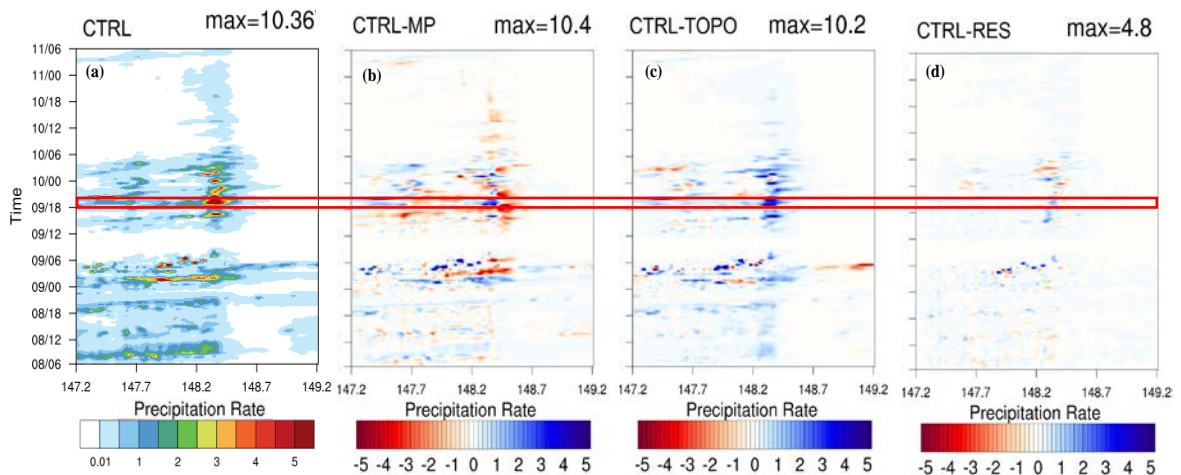


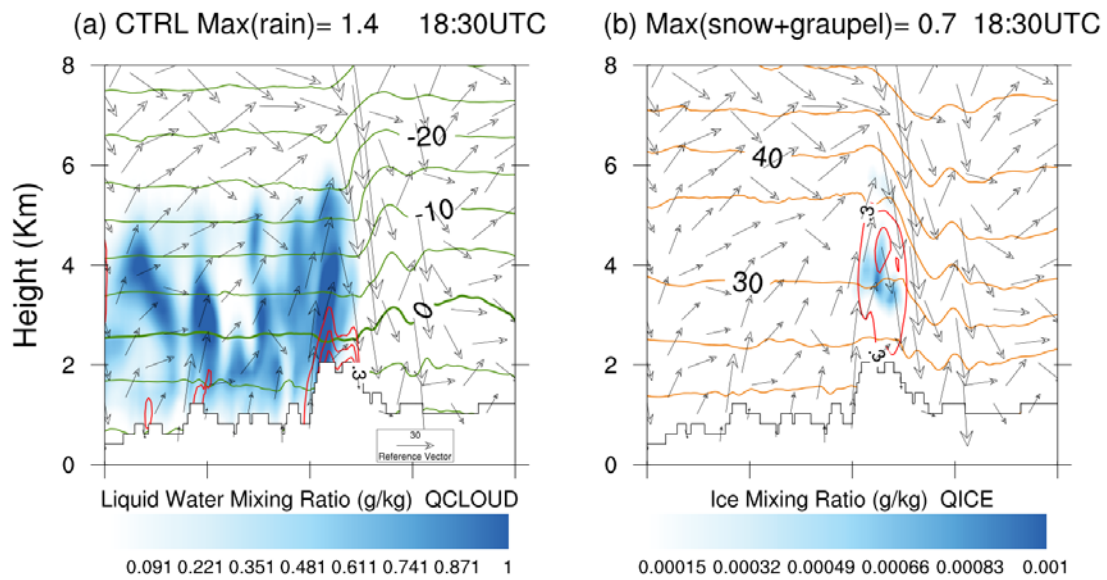
Figure 4.11 Time-distance diagrams showing half-hourly precipitation for (a) CTRL-run and differences rates in mm for a 72-hour period (0006 UTC 8 May to 0006 UTC 11 May 2016) through latitude 36.4°S for (b) CTRL–MP run; (c) CTRL-TOPO run; (d) CTRL-RES run. The vertical cross-sections are taken at a time during the post-frontal period, as indicated inside the red box.

Given that orographic precipitation is a direct product of the microphysical processes in the orographic clouds, it is important to further examine the cloud microphysical structure and associated orographic enhancement mechanisms. To do this, a series of vertical cross sections along latitude 36.4°S, showing the mixing ratios of different hydrometeor species, are drawn for CTRL-run, MP-run and TOPO-run (Figure 4.12). The focus is given to the

outputs at 18:30 UTC 9 May during the post-frontal period, when the largest discrepancies are found between the precipitation simulations (see Figure 4.11) and the dominant CTP is SLW (see Figure 4.13b). Previous studies have suggested that SLW is frequently observed during the post-frontal period in this region (e.g. Long and Huggins 1992; Chubb et al. 2012; Osburn et al. 2016). Looking first at cloud water mixing ratio, CTRL experiment has produced greater cloud liquid and maintained much more supercooled liquid water extended to higher altitudes (up to 6 km above the surface), where the temperature is as low as  $-20^{\circ}\text{C}$  (Figure 4.12a). A comparison of the solid phases (Figure 4.12; right panels) illustrates discernible differences between the three runs. A distinctly greater amount of total ice (ice+snow) is produced over the upwind slope, the mountain peak, and the immediate downwind slope, by the single-moment scheme. The Thompson scheme is double-moment for rain and ice (prognostic mass and number concentrations) and single-moment for other variables (snow, graupel, cloud water, and vapour). As the cloud number concentration is fixed in both MP schemes ( $300\text{ cm}^{-3}$  over land), the effects on the supercooled water contents due to the difference in the number concentration is limited. Graupel efficiently lead to surface precipitation due to being a large, fast-falling particle. This could partly explain the higher production of ice and precipitation on the peaks in the MP-run, which does not predict graupel as a prognostic variable. Note the different scale in ice mixing ratio in MP-run (two orders of magnitude larger than others). More rain is also produced in the immediate downwind slope, too, possibly as a consequence of melting (Figure 4.12d). The presented features suggest that the WSM5 MP scheme tends to simulate ice particles as large as snow, in contrast to the Thompson scheme. This feature is likely to be arising from the WSM5 scheme's tendency to initiate ice more rapidly at ice saturation from vapour (deposition growth), limiting the environment for cloud water generation. Several times greater solid hydrometeors further suggest that cold cloud precipitation (by riming and aggregation) is a dominant process in the WSM5 scheme that leads to less supercooled liquid water in the atmosphere (Figure 4.12c). This result is consistent with what Listowski and Lachlan-Cope (2017) reported in terms of the simulated thermodynamic phases of the orographic clouds over the Antarctic Peninsula. They found that WSM5 MP scheme predicts mostly glaciated clouds in the region of interest. They noted that the inverse relationship between the liquid water content and solid water content in this scheme suggests a systematic water vapour depletion at the expense of the liquid phase. It is also worth noting that in the Thompson

scheme, snow is assumed to be non-spherical with density that varies inversely with the particle size. This is different from most single-moment schemes where snow is assumed to be spherical with a constant bulk density. Accordingly, for a given snow mixing ratio, the Thompson scheme tends to produce snow with larger mass-weighted mean size, resulting in slower depositional growth, riming and sedimentation, hence maintaining more supercooled liquid water (Thompson et al. 2008).

The terrain-induced gravity waves and the induced wave breaking in the lee-side are substantially weakened in TOPO, where the approaching airflow is weakly blocked (Figure 4.12f). Smith (1979) noted that the vertical motions of these terrain-forced gravity waves can greatly affect the orographic precipitation distribution. Another feature of this plot is the limited rain mass production, developed in warm clouds (condensation and then collision/coalescence) or supercooled warm rain process in MP-run. More warm rain process in CTRL-run than MP-run is due to less abundant solid hydrometeors which sustains liquid phase. Vertical cross-sections of different phases of water mixing ratio show that the coarse horizontal resolution of the orography often produces slightly lower liquid and ice cloud water mixing ratio in comparison with the finer grid spacing (not shown).



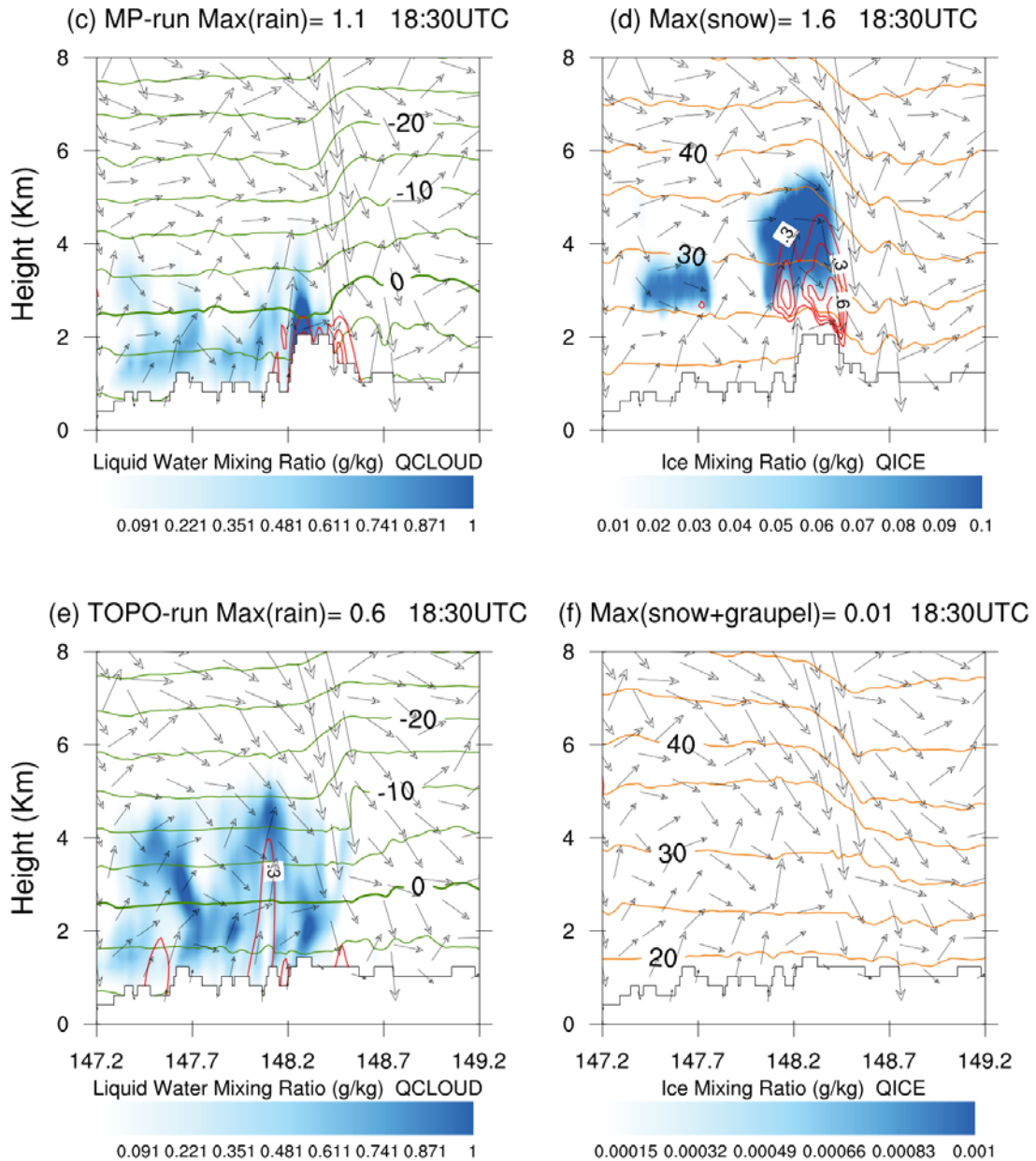


Figure 4.12 Vertical cross-sections of the simulated (a) liquid (shaded) with rain (red lines with 0.3 g/kg interval), (b) with small ice particles (shaded) with total big ice hydrometeors (red line with 0.3 g/kg interval) for (a-b) CTRL-run, (c-d) MP-run, and (e-f) TOPO-run through latitude 36.4°S at 18:30 UTC, overlaid with the simulated temperatures (left panels, green contours, thick line indicates freezing level with 5°C interval), potential temperature (right panels, orange contours with 5°C interval) and wind vectors (20vertical wind ×N-S wind).

Figure 4.13 shows a deeper investigation of the two microphysics parameterizations (at 18:30 UTC 9 May) compared to Himawari-8 satellite observations (at 17:40 UTC 9 May). Cloud-top temperatures (CTTs, left panels) and cloud-top thermodynamic phases (CTPs, right panels) are shown. Simulated CTTs and CTPs are defined by Huang et al. (2014) diagnostic method based on the relative fraction of liquid water to total water, and cloud top defined at 0.5 cloud optical thickness from the top of the model domain. Some high-level cold cirrus clouds are evident in the observation, with CTTs colder than  $-35^{\circ}\text{C}$  that are not being well simulated. Some convection activities are also detectable over there according to the satellite observations. To clarify some uncertainties on the potential ice generation by the convective systems across the southern peak, the cross-section of the northern peak of the mountain (along latitude  $36.1^{\circ}\text{S}$ ) was also investigated (not shown). A consistent picture across both peaks in the simulations was found. The similarity between the observed cloud-top characteristics and the simulated ones in CTRL experiment is obvious, where supercooled liquid water is found to be the dominant phase (Figure 4.13b and d). In contrast, CTPs in WSM5 MP scheme that predicts mostly glaciated clouds are less comparable to the satellite observations (Figure 4.13f). Similar to our findings, Huang et al. (2018) in a recent case study of wintertime precipitation over the Snowy Mountains, configured with a single-moment microphysical scheme (Wilson and Ballard 1999), noted the ice-dominated cloud tops during the post-frontal period, compared to the satellite observations.

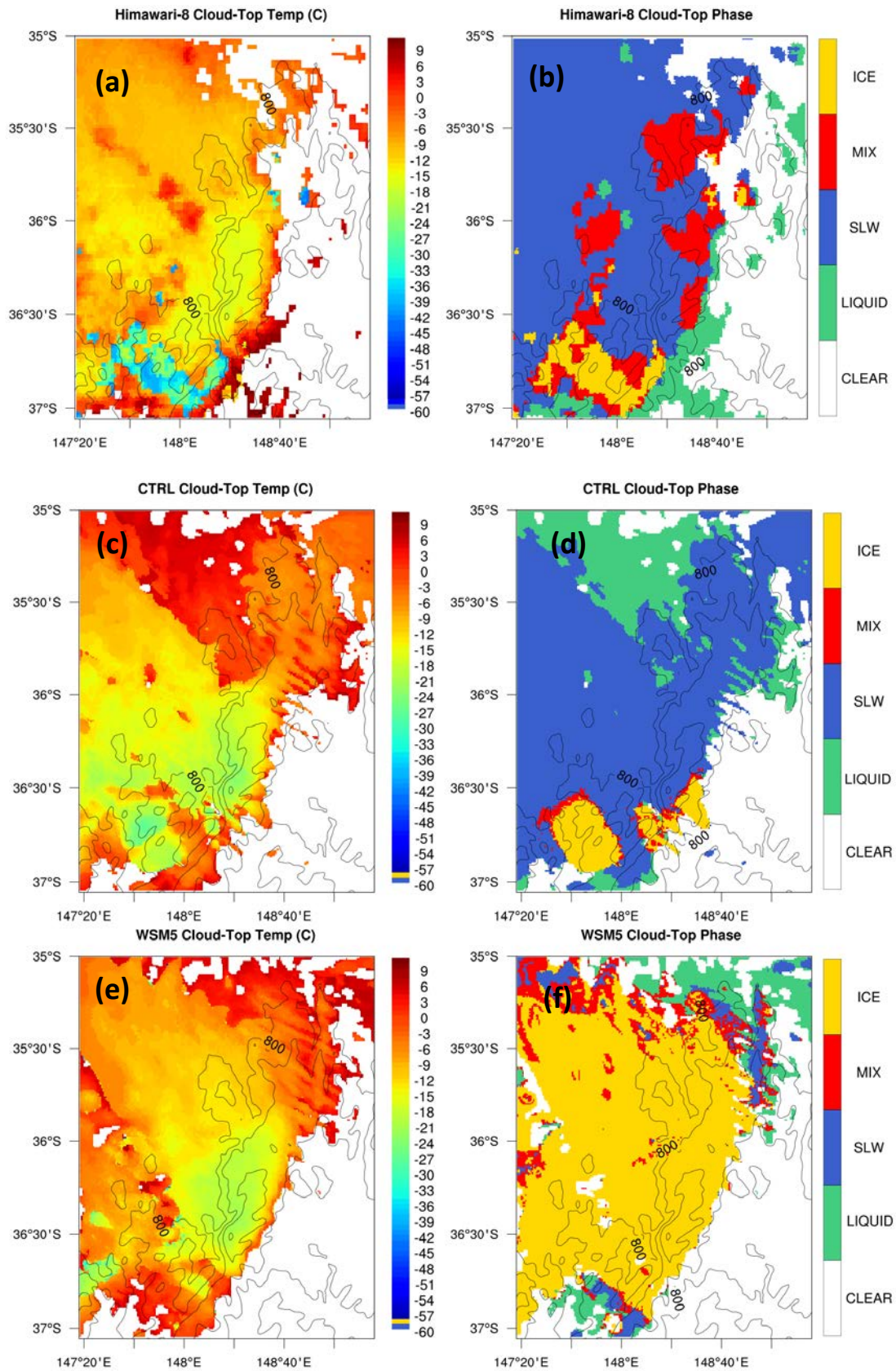


Figure 4.13 Cloud top temperature (left panels) and cloud top phase (right panels) from Himawari-8 (a-b) at 1740UTC 9 May 2016, CTRL-run (c-d) and MP-run (e-f) at 1830UTC 9 May 2016.

To describe the statistical distribution of CTP, histograms of the relative frequencies of the CTP decomposed into 5°C temperature bins (Figure 4.14). The cloud fraction (CF), defined by the ratio of cloudy columns to the total number of columns is shown on each panel.

Looking at the relative frequencies of the CTP at 1740 UTC 9 May 2016 (Figure 4.14a), the Himawari-8 CTP histogram suggests a total cloud fraction of 70%, with an outstanding amount (65%) residing between -5°C and 5°C, where the dominant CTP is SLW (54%). Histograms for the simulated cloud top for the CTRL-run (Figure 4.14b) display notable similarities to that observed in terms of the relative frequencies of SLW, although the cloud fraction and the warm clouds ( $CTT > 0^{\circ}\text{C}$ ) are over-predicted by 5% and 13%, respectively. The CTRL-run does a reasonable job in reproducing the SLW cloud top down to -20°C, whereas too much ice cloud top is produced by the MP-run (Figure 4.14c) for the same temperature range, although the MP-run does a better job in producing the mixed-phase cloud tops in comparison to the observation.

Looking at the overall relative frequencies of the CTP for a 69-hour period, the cloud fraction is significantly lower in both runs, compared to the Himawari-8 observation (Figure 4.14, bottom plots). This underestimation in the simulated cloud fraction is mostly arising from the underestimation of the ice clouds in the CTRL-run (18.4%, compared to 35.5% for Himawari-8) and the SLW clouds in the MP-run (11.06%, compared to 21.23% for Himawari-8). However, this discrepancy between the observations and the simulations might also be due to the misclassification of cloud top phase products from Himawari-8 retrievals, in which liquid phases exist at temperatures below freezing (see Figure 4.14a and d). The CTRL run (Figure 4.14e) under-predicts the ice clouds below homogeneous freezing temperature (-40°C). While more high clouds are simulated in the MP run, they are produced at much colder temperatures (Figure 4.14f).

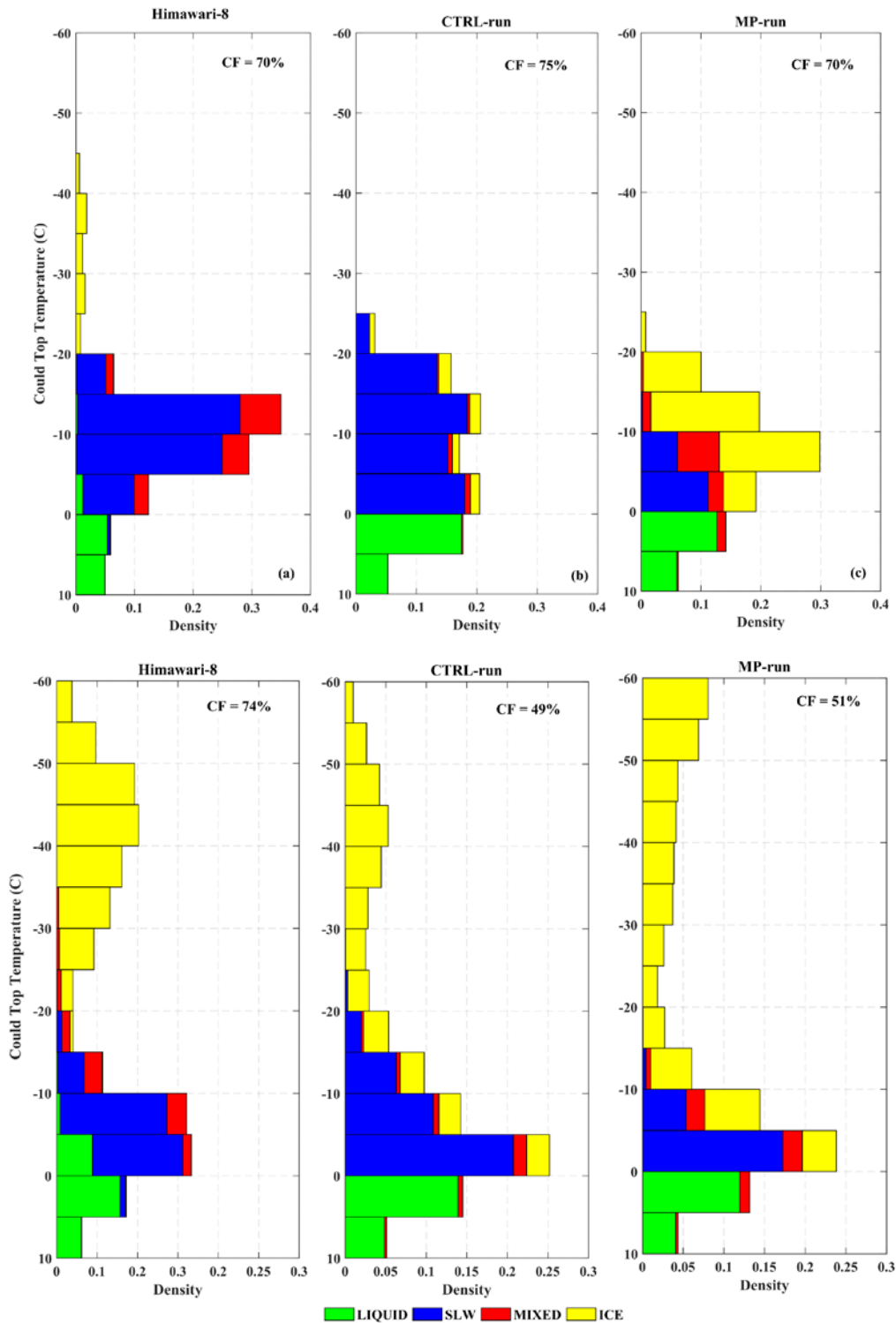


Figure 4.14 Histograms showing the relative frequencies of CTP decomposed into 5°C temperature bins. Top plots: The observation from Himawari-8 at 1740 UTC 9 May 2016 (left), CTRL-run (middle) and MP-run (right) at 1830 UTC 9 May 2016. The simulated cloud top is defined at 0.5 cloud optical thickness from the top of the model domain. Bottom plots: same as top plots, showing the relative frequencies of CTP but over a period of 69 hours.

## 4.8 Summary and Conclusion

Despite the implementation of sophisticated numerical models, precipitation forecast in the Alpine area is still an elusive goal as it involves interactions between different types of processes, which brings uncertainties to in NWP models.

A primary aim of this research is to evaluate the performance of the WRF model simulation of precipitation against the SHL rain gauge observations for a case study of a heavy precipitation event in May 2016. The selected days of simulations are featured by the synoptic classes transitioning from C1 on 8 and 9 May 2016, to C2 on 10 May, to C3 on 11 May 2016. These transitions of synoptic setting show the large-scale synoptic meteorology and the low-level atmospheric stability, where C1 is associated with cold frontal passages and being unstable to orographic lifting (low values of non-dimensional mountain height) and includes the heaviest precipitation days. The selection of this event allows assessing the model performance in such synoptic conditions.

The large-scale meteorology was well simulated in terms of both the location and the magnitude of the low surface pressure system. Comparison of upper air atmospheric profiles from the Wagga Wagga weather station illustrated good agreement in both wind speed and direction with marginal differences in timing. The simulation with the control configuration also demonstrated a considerable level of skill in simulating both the spatial distribution and the intensity of precipitation over the high elevations as compared to the high-density ground-based observations and reproduced the timing of the precipitation phases reasonably well with a 1-hour lag.

Further, the WRF model used to investigate the sensitivity of the dynamical and microphysical processes over the Snowy Mountains to changes in the topography, horizontal resolution, and the parameterization of microphysics. A range of simulations were conducted to investigate the sensitivity of the mentioned factors against the “control” simulation (CTRL-run) that is configured with the Thompson double-moment microphysical parameterization scheme. Our major findings of the conducted sensitivity analysis are summarized as follows:

- Reducing the elevation above 1000 m by 75% decreases the maximum precipitation by up to 70% over the mountains, leading to a domain average reduction of about 27%. From a dynamical point of view, the orographic signal has lessened and hardly noticeable in the spatial distribution of the precipitation with the weakened rain shadow effect on the downwind side. Moreover, weaker terrain-induced gravity waves are generated in the lee-side of the mountains. From a microphysical point of view, near zero prediction of solid hydrometeors (ice, snow and graupel) limits rain mass production.
- Changing the microphysics schemes from the Thompson semi-double-moment 6-class scheme to the single-moment 5-class scheme (WSM5) leads to a change of spatial distribution of precipitation with a reduction of precipitation over the mountain peaks and enhanced precipitation over the windward and lee slopes. The domain-averaged rain accumulation is less sensitive to the choice of microphysics (about 6% increase) compared with its clear impact on the precipitation spatial distribution. In addition to the different classification of hydrometeor species and their number of moments, these two MP schemes differ in many other aspects (e.g., particle size distributions, particle shapes, mass-diameter relationships, particle fall speed assumptions and growth process treatments) that likely cause variations in the estimation of precipitation (Han et al. 2013). It is found that the single-moment scheme tends to readily transform SLW to ice. The single-moment scheme is not optimal for clouds with a substantial amount of supercooled liquid water. It is also worth noting that the CTRL-run tends to generally underestimates the precipitation that is likely due to higher concentration of SLW, which leads to longer cloud lifetime and consequently lower precipitation rates, compared to the simulated ice clouds in the MP-run (Raubert and Grant 1987). Comparison with Himawari-8 satellite shows that the Thompson MP scheme is more capable of simulating CTTs and CTPs over the analysis region.
- Replacing the orography of d02 (3 km) by that of was used in d03 (1 km), however, shows much less sensitivity in the orographic precipitation (only a slight reduction of about 4% in the area-average of the accumulated precipitation); that is, changing

the horizontal resolution of topography leads to only a marginal impact on the spatial distribution of precipitation. Vertical cross-sections of different phases of water mixing ratio show that the coarse horizontal resolution of the orography often produces slightly lower liquid and ice cloud water mixing ratio in comparison with the finer grid spacing (not shown). Precipitation biases are more likely to arise from uncertainties in the physical processes represented in the model rather than the resolution of the grid spacing in the orography.

# **Chapter 5**

## **Summary**

The Snowy Mountains are the tallest mountains among a few alpine regions in Australia. Precipitation over the Snowy Mountains has been of great interest, given its central role in feeding some of the major river systems of the Murray-Darling Basin, as well as providing hydroelectric power for much of eastern Australia. This study looked at the climatology and predictability of wintertime precipitation in the Snowy Mountains.

Motivated by the recent drought in southeastern Australia, this study employed a clustering analysis to categorize the climatology of daily wintertime precipitation. The algorithm employed seven predictors, representing large-scale environment and the low-level atmospheric stability. The interactions between the large-scale environment and the low-level atmospheric stability across the Snowy Mountains were also investigated. Examining the sensitivity of the wintertime precipitation over this region to changes in the low-level atmospheric stability as seen through the non-dimensional mountain height index was of further interest to our study. With the aim of improving the accuracy of the current operational ACCESS\_R daily wintertime precipitation forecast, model output statistics (MOS) were employed. Finally, the performance of the Weather Research and Forecasting (WRF) NWP model in simulating precipitation event, featured by the transition of synoptic clusters, was evaluated. A suite of carefully designed sensitivity simulations were also undertaken, with the aim of gaining insights into the underlying dynamics and microphysics of the orographic precipitation events.

## **5.1 A climatology of wintertime precipitation over the Australian Snowy Mountains**

Previous studies have demonstrated that wintertime precipitation across the Australian Snowy Mountains is mostly governed by the large-scale synoptic meteorology. (e.g. D14; Theobald et al. 2015). Following the D14 methodology, a K-means clustering algorithm is employed using six synoptic predictors including moisture fluxes and variables related to stability of the atmosphere and shear. These indicators are westerly (QU) and southerly (QV) moisture flux up to 250 hPa, total moisture up to 250 hPa (TW), surface pressure at Wagga

Wagga (GP), the root-mean-square wind shear between 850 and 500 hPa (SH), and total totals index (TT). The standard-level data from the Wagga Wagga sounding profiles is used to calculate daily values of these predictor. These clusters define the large-scale environment the characteristics of the dominant precipitation regimes. With 21 years winter data (May–October, 1995–2015), four different precipitation regimes are identified to have distinct precipitation distributions. The initial classification also distinctly defines the low-level stability by class, suggesting that the low-level stability is reflected in the broader synoptic meteorology. Consistent with theory, the wet classes are found to have weak low-level stability, and the dry classes have strong low-level stability. In addition to the six indicators, the low-level atmospheric stability, as seen through the square of the nondimensional mountain height ( $\hat{H}^2$ ), is added as a seventh predictor. By including low-level stability as an additional input variable to the clustering method, only minor changes were observed for the two wet clusters with only a handful of days swapping between clusters. The two dry clusters, however, were found to be more sensitive to this revision. Precipitation is obtained from seven weather stations above 1100m across the Snowy Mountains for a 21-yr period from 1995 to 2015.

Based on seven-variable, it is found that there are two classes (C1 and C2) with high intensity (23 and 11 mm day<sup>-1</sup>) but low frequency of occurrence (10% and 22%), one (C3) with moderate intensity (6.1 mm day<sup>-1</sup>) and high frequency (39%), and one (C4) with the lowest intensity (3.3 mm day<sup>-1</sup>) and moderate frequency (28%). The probability of rainy days is dropped from 93% for C1 to 22% for C4. In contrast, the mean values of  $\hat{H}^2$  for the four clusters are increased from -0.45 for C1 to 20.20 for C4. Higher values of  $\hat{H}^2$  indicates stable or blocked conditions and, accordingly, less orographic precipitation. The probability density functions of  $\hat{H}^2$  for all days show that only 25% of total days are blocked ( $\hat{H}^2 > 1$ ) while their corresponding precipitation intensity is about four times greater than the rest of the unblocked days ( $\hat{H}^2 < 1$ ). The least frequent class (C1) contributes 39% of the winter precipitation, while C4 makes up only 5% of the total winter precipitation. C2 and C3 account for 33% and 23% of the total wintertime precipitation, respectively.

Composite synoptic charts for each cluster are also derived using the ERA-Interim reanalysis products to better understand the synoptic meteorology. C1 is found to be associated with a frontal passage with dominant north-westerly flow and deep moisture fluxes extend up the

Great Dividing Range through New South Wales and Queensland. C2 is mainly related to a post-frontal environment with strictly westerly flux and moderate static instability (as expressed by TT). C3 is a dry cluster and more frequently observed in early winter, and is largely constructed from the remaining observations. A very weak midlevel shear (SH), just to the south of the Snowy Mountains, over Bass Strait and extending into the Tasman Sea is also evident. C4 is the driest class, with the weakest moisture fluxes evident over the mountains, associated with the most stable conditions. It occurs more often in midwinter and tends to be under the influence of a strong anticyclone systems.

## **5.2 Adjustment to the ACCESS\_R forecast of daily wintertime precipitation over the Australian Snowy Mountains**

Downscaling methods have been widely used to adjust the output of numerical models. Here, model output statistics (MOS) was used with/without implementing the classification. The goal is to reduce the RMSE and bias in the daily ACCESS-R precipitation forecasts by relating model output to observations. The daily ACCESS-R precipitation forecasts (Australia-wide regional with 12-km spatial resolution) for the two years (2014–15) of cold months (May–October) are found to slightly overestimate the Snowy Hydro’s high-elevation surface observations (seven weather stations above 1100m) with an overall RMSE of 6.20 mm and a bias of 0.42 mm on rain days. Some normalized skill scores are also considered for evaluation of precipitation forecasts from the operational ACCESS-r model. For the overall time period the frequency bias score (FBS) is calculated to be 1.12, suggesting that the model generally tends to predict rain days more frequently than they are observed. The equitable threat score (ETS), often used in NWP inter-comparisons, is calculated to be 0.49 for the overall time period.

Sensitivity of precipitation over the Snowy Mountains to the large-scale synoptic meteorology and the low-level stability is investigated. Based on analysis on historical data (1995–2015), QV, QU, GP, and TW are highly correlated with wintertime precipitation, while the stability measures ( $\hat{H}^2$ , TT, and SH) are less strongly correlated. Statistically significant correlations confirms our underlying premise that these variables can be of use in forecasting orographic precipitation. Further examination reveals a highly nonlinear relationships between  $\hat{H}^2$  and precipitation; heavy rain was associated with very weak low-

level stability, and conversely, strong low-level stability was associated with very little precipitation.

MOS is a commonly used, statistical downscaling approach to improve forecast skill which depends on a historical relationship between model output and observations. In this study, this statistical technique is used to discover whether the daily ACCESS-R precipitation forecasts over the high elevations of the Snowy Mountains can be improved using a linear regression built on historical relationships that depends upon the large-scale environment and the low-level stability. First, a single regression model is developed based on 2 years of ACCESS-R precipitation forecasts (MODEL 1). The ACCESS-R precipitation forecast and QU are determined to be predictors by the stepwise algorithm coupled with BIC. The model reduces the RMSE from 6 to 5.6 mm by (7% improvement) on forecast precipitation days.

Then, four distinct regression models are developed using the same algorithm for each synoptic class (Chapter 2) with the goal of improving the prediction of precipitation intensity on forecast rain days (MODEL 2). The overall RMSE is reduced by 30%, dropping from 6 to 4.2 mm and the bias was reduced from 0.68 to -0.10 mm. Synoptic classification is found to sharpen the reliability of the ACCESS-R precipitation forecast. Cross-validation of regression models is then undertaken through a bootstrap technique to ensure that the results are statistically robust. This process is repeated 10000 times, and each time 80% of the data were randomly assigned to the control group for deriving the coefficient and the rest for testing.

### **5.3 Sensitivity Analysis of orographic precipitation using WRF Model**

In spite of the significant progress in the implementation of increasingly sophisticated numerical models, forecasting orographic precipitation continues to be a challenge. To reach a deeper understanding of the dynamical and physical processes that characterize the precipitation characteristics in this region, numerical simulations of the meteorology for the case study was performed. Wintertime cold fronts generate much of the precipitation in the Snowy Mountains of south eastern Australia where orographic clouds composed primarily of supercooled liquid water (SLW) are frequently observed (Morrison et al. 2013; Osburn

et al. 2016). A case study of a heavy precipitation event in late autumn (May 2016) is presented to better understand this precipitation. A frontal system generated from a strong cut-off low passed over the mountains producing up to 145 mm of precipitation over a period of 72 hours. The selected days of simulations are featured by the synoptic classes transitioning of synoptic setting from C1 on 8 and 9 May 2016, to C2 on 10 May, to C3 on 11 May 2016. Given the many challenges in short-term quantitative precipitation forecasting, the main objectives are:

- Evaluate the performance of the simulation of precipitation and clouds using high density ground based observations.

A range of simulations are conducted to investigate the sensitivity of the following factors on the magnitude and the spatial distribution of precipitation, against the “control” simulation (CTRL-run):

- Explore the impact of changes in the topography (TOPO-run: Reducing the elevation above 1000 m by 75%).
- Explore the role of horizontal resolution of the topography (RES-run: Replacing the orography of d02 (3 km) by that of was used in d03).
- Explore the role of microphysics schemes (MP-run: Changing the microphysics schemes from the Thompson semi-double-moment 6-class scheme to the single-moment 5-class scheme).

The Weather Research and Forecasting (WRFV3.8.1) NWP model is used to undertake the sensitivity experiments. Surface observation operated by Snowy Hydro Ltd. and some cloud features detected by Himawari-8 satellite have been used to evaluate the model. The upper-air soundings from the closet upper-wind site are also compared to assess the broad-scale meteorology and the thermodynamical structures. Comparison of sounding profile from the Wagga Wagga weather station illustrates good agreement in both wind speed and direction. The large-scale meteorology is also found to be well captured in terms of both the location and the magnitude of the low surface pressure system. The model shows a considerable level of skill in simulating the spatial distribution and the intensity of precipitation with an RMSE of 20.8 mm and a bias of -1.2 mm based on the 69-hr

accumulated precipitation at the 51 stations. The associated cloud properties, such as cloud-top temperature and phase as observed by Himawari-8 are also well simulated.

It is found from the TOPO-run that the maximum precipitation decreases, up to 70% over the mountains, leading to a reduction of about 27% on a domain-average. Vertical cross-sections of different phases of water mixing ratio show that Topo-run predicts near zero solid hydrometeors (ice, snow and graupel) which limits rain mass production. Weaker terrain-induced gravity waves are generated in the lee-side of the mountains. The approaching flow continues to pass over the less-impeding ridge, which weakens the rain shadow effect.

Changing the microphysics schemes from the Thompson semi-double-moment 6-class scheme to the single-moment 5-class scheme leads to a change of spatial distribution of precipitation with a reduction of precipitation over the mountain peaks and enhanced precipitation over the windward and lee slopes. The domain-averaged precipitation accumulation is less sensitive to the choice of microphysics (about 6% increase) compared with its clear impact on the precipitation pattern. The single-moment scheme tends to simulate a larger ice mixing ratio and is less favourable for clouds composed of supercooled liquid water.

Orographic precipitation, however, shows much less sensitivity (only a slight reduction of about 4% in the area-average of the accumulated precipitation) to upscaling the horizontal resolution of the topography. There is also a marginal impact on the spatial distribution of precipitation of replacing the coarse horizontal resolution of the orography data with the finer grid spacing. This further suggests that the precipitation biases are more likely to be arising from uncertainties in the physical processes rather than the resolution of the grid spacing in the orography.

#### **5.4 Future directions**

In this thesis, there are a number of avenues that could benefit from further investigation, including:

A potential extension of this work could be to consider the application of statistical adjustments for forecasts at longer lead times in the climatology studies presented in chapter 3. The ACCESS-R model only runs for 72 h, preventing such testing on the immediate observations and simulations. As the accuracy of the ACCESS system continues to improve, the main value of such statistical analysis may be in the identification of the source of systematic errors in the system. Forecasts with different resolutions and parameterizations worth to be examined.

More sensitivity experiments are required to uncover the source of potential uncertainties in the NWP models. Whilst the Thompson microphysics scheme used in CTRL-run has shown promising skills in reproducing the hydrometeors, the model has still some difficulties in simulating the temporal, spatial distribution and intensity of the orographic precipitation over the Snowy Mountains. For example, undertaking a sensitivity test with a new choice of physics (e.g. different boundary layer module) may permit a better insight into the details of the orographic forcing processes. Finally, better observations are needed to better understand the underlying dynamics and microphysics of the orographic precipitation events. This further highlights the need for a dedicated field campaign.

## References

- ABS/ABARE/BRS, 2009: *Socio-Economic Context for the Murray-Darling Basin - Descriptive Report*.
- Aghakouchak, A., G. Ciach, and E. Habib, 2010: Estimation of tail dependence coefficient in rainfall accumulation fields. *Adv. Water Resour.*, **33**, 1142–1149. <https://doi.org/10.1016/j.advwatres.2010.07.003>.
- Ashok, K., Z. Guan, and T. Yamagata, 2003: Influence of the Indian Ocean Dipole on the Australian winter rainfall. *Geophys. Res. Lett.*, **30**. <https://doi.org/10.1029/2003GL017926>.
- Baines, P. G., 1987: Upstream blocking and airflow over mountains. *Annu. Rev. Fluid Mech.*, **19**, 75–97.
- Bergeron, T. (1935), On the physics of clouds and precipitation, *Proces Verbaux de l'Association de Météorologie*, International Union of Geodesy and Geophysics, 156–178.
- Brunet, N., R. Verret, and N. Yacowar, 1988: An objective comparison of model output statistics and «perfect prog» systems in producing numerical weather element forecasts. *Weather Forecast.*, **3**, 273–283. [https://doi.org/10.1175/1520-0434\(1988\)003%3C0273:AOCOMO%3E2.0.CO;2](https://doi.org/10.1175/1520-0434(1988)003%3C0273:AOCOMO%3E2.0.CO;2).
- Bureau of Meteorology, 2017: About East Coast Lows. Accessed 20 March 2017.
- Chen, F., and J. Dudhia, 2001: Coupling an Advanced Land Surface–Hydrology Model with the Penn State–NCAR MM5 Modeling System. Part II: Preliminary Model Validation. *Mon. Weather Rev.*, **129**, 587–604.
- Chou, M.-D., and M. J. Suarez, 1994: *An efficient thermal infrared radiation parameterization for use in general circulation models*. 85 pp. <http://citeseerx.ist.psu.edu/viewdoc/summary?doi=10.1.1.26.4850>.
- Chubb, T. H., S. T. Siems, and M. J. Manton, 2011: On the decline of wintertime precipitation in the Snowy Mountains of southeastern Australia. *J. Hydrometeorol.*, **12**, 1483–1497. <http://journals.ametsoc.org/doi/abs/10.1175/JHM-D-10-05021.1>.
- , A. E. Morrison, S. Caine, S. T. Siems, and M. J. Manton, 2012: Case studies of orographic precipitation in the brindabella ranges: Model evaluation and prospects for cloud seeding. *Aust. Meteorol. Oceanogr. J.*, **62**, 305–321, doi:10.22499/2.6204.009.
- , M. J. Manton, S. T. Siems, A. D. Peace, and S. P. Bilish, 2015: Estimation of Wind-

- Induced Losses from a Precipitation Gauge Network in the Australian Snowy Mountains. *J. Hydrometeorol.*, **16**, 2619–2639. <https://doi.org/10.1175/JHM-D-14-0216.1>.
- , ———, S. T. Siems, and A. D. Peace, 2016: Evaluation of the AWAP daily precipitation spatial analysis with an independent gauge network in the Snowy Mountains. *J. South. Hemisph. Earth Syst. Sci.*, **66**, 55–67, doi:10.22499/3.6601.006.
- Colle, B. A., 2004: Sensitivity of Orographic Precipitation to Changing Ambient Conditions and Terrain Geometries: An Idealized Modeling Perspective. *J. Atmos. Sci.*, **61**, 588–606.
- , and C. F. Mass, 2000: The 5–9 February 1996 Flooding Event over the Pacific Northwest: Sensitivity Studies and Evaluation of the MM5 Precipitation Forecasts. *Mon. Weather Rev.*, **128**, 593–617.
- , J. B. Wolfe, W. J. Steenburgh, D. E. Kingsmill, J. A. W. Cox, and J. C. Shafer, 2005: High-Resolution Simulations and Microphysical Validation of an Orographic Precipitation Event over the Wasatch Mountains during IPEX IOP3. *Mon. Weather Rev.*, **133**, 2947–2971. <https://doi.org/10.1175/MWR3017.1>.
- Curtis, S. M. K., and S. K. Ghosh, 2011: A bayesian approach to multicollinearity and the simultaneous selection and clustering of predictors in linear regression. *J. Stat. Theory Pract.*, **5**, 715–735. <https://doi.org/10.1080/15598608.2011.10483741>.
- Dai, J., M. J. Manton, S. T. Siems, and E. E. Ebert, 2014a: Estimation of Daily Winter Precipitation in the Snowy Mountains of Southeastern Australia. *J. Hydrometeorol.*, **15**, 909–920. <https://doi.org/10.1175/JHM-D-13-081.1>.
- Davies, T., M. J. P. Cullen, A. J. Malcolm, M. H. Mawson, A. Staniforth, A. A. White, and N. Wood, 2005: A new dynamical core of the Met Office’s global and regional modelling of the atmosphere. *Q. J. R. Meteorol. Soc.*, **131**, 1759–1782. <https://doi.org/10.1256/qj.04.101>.
- Dee, D. P., and Coauthors, 2011: The ERA-Interim reanalysis: Configuration and performance of the data assimilation system. *Q. J. R. Meteorol. Soc.*, **137**, 553–597. <https://doi.org/10.1002/qj.828>.
- van Dijk, A. I. J. M., H. E. Beck, R. S. Crosbie, R. A. M. De Jeu, Y. Y. Liu, G. M. Podger, B. Timbal, and N. R. Viney, 2013: The Millennium Drought in southeast Australia (2001–2009): Natural and human causes and implications for water resources,

- ecosystems, economy, and society. *Water Resour. Res.*, **49**, 1040–1057, doi:10.1002/wrcr.20123.
- Drouet-Mari, D., and S. Kotz, 2001: Correlation and Dependence. *Imperial College Press*, 236 pp.
- Durrán, D. R., 1990: Mountain Waves and Downslope Winds. *Atmos. Process. over Complex Terrain*, **23**, 59–81. [http://link.springer.com/10.1007/978-1-935704-25-6\\_4](http://link.springer.com/10.1007/978-1-935704-25-6_4).
- , and J. B. Klemp, 1982: On the Effects of Moisture on the Brunt-Vaisala Frequency. *J. Atmos. Sci.*, **39**, 2152–2158. [https://doi.org/10.1175/1520-0469\(1982\)039%3C2152:OTEOMO%3E2.0.CO;2](https://doi.org/10.1175/1520-0469(1982)039%3C2152:OTEOMO%3E2.0.CO;2).
- Ebert, E. E., 2001: Ability of a Poor Man’s Ensemble to Predict the Probability and Distribution of Precipitation. *Mon. Weather Rev.*, **129**, 2461–2480. [https://doi.org/10.1175/1520-0493\(2001\)129%3C2461:AOAPMS%3E2.0.CO;2](https://doi.org/10.1175/1520-0493(2001)129%3C2461:AOAPMS%3E2.0.CO;2).
- ETI Instrument Systems Inc., 2008: NOAH II (TM) total precipitation gauge (30-inch capacity manually serviced). *Tech. Manual*, 42 pp.
- Fiddes, S. L., A. B. Pezza, and V. Barras, 2015: Synoptic climatology of extreme precipitation in alpine Australia. *Int. J. Climatol.*, **35**, 172–188, doi:10.1002/joc.3970.
- Findeisen, W. (1938), Kolloid-meteorologische Vorgänge bei Neiderschlags-bildung, *Meteor. Z.*, **55**, 121-133.
- Flesch, T. K., and G. W. Reuter, 2012: WRF model simulation of two Alberta flooding events and the impact of topography. *J. Hydrometeorol.*, **13**, 695–708, doi:10.1175/JHM-D-11-035.1.
- Fritsch, J., and Coauthors, 1998: Quantitative Precipitation Forecasting: Report of the Eighth Prospectus Development Team, U.S. Weather Research Program. *Bull. Am. Meteorol. Soc.*, **79**, 285–299.
- Gallant, A. J. E., A. S. Kiem, D. C. Verdon-Kidd, R. C. Stone, and D. J. Karoly, 2012: Understanding hydroclimate processes in the Murray-Darling Basin for natural resources management. *Hydrol. Earth Syst. Sci.*, **16**, 2049–2068, doi:10.5194/hess-16-2049-2012.
- Ganetis, S. A., and B. A. Colle, 2015: The Thermodynamic and Microphysical Evolution of an Intense Snowband during the Northeast U.S. Blizzard of 8-9 February 2013. *Mon. Weather Rev.*, **143**, 4104. <https://doi.org/10.1175/MWR-D-14-00407.1>.
- Garric, G., H. Douville, and M. Déqué, 2002: Prospects for improved seasonal predictions

- of monsoon precipitation over Sahel. *Int. J. Climatol.*, **22**, 331–345, doi:10.1002/joc.736.
- Genest, C., and J. Plante, 2018: On Blest's Measure of Rank Correlation. *Can. J. Stat.*, **31**, 35–52. <https://doi.org/10.2307/3315902>.
- Glahn, H. R., and D. a. Lowry, 1972: The Use of Model Output Statistics (MOS) in Objective Weather Forecasting. *J. Appl. Meteorol.*, **11**, 1203–1211, doi:10.1175/1520-0450(1972)011<1203:TUOMOS>2.0.CO;2.
- Gorman, J. D., 2003: *LABORATORY EVALUATION OF THE BUREAU DESIGNED HEATED TIPPING BUCKET RAIN GAUGE*. 1-12 pp. <https://www.wmo.int/pages/prog/www/IMOP/WebPortal-AWS/Tests/ITR675.pdf>.
- Grubišić, V., R. K. Vellore, and A. W. Huggins, 2005: Quantitative Precipitation Forecasting of Wintertime Storms in the Sierra Nevada: Sensitivity to the Microphysical Parameterization and Horizontal Resolution. *Mon. Weather Rev.*, **133**, 2834–2859. <http://journals.ametsoc.org/doi/abs/10.1175/MWR3004.1>.
- Han, M., S. A. Braun, T. Matsui, and C. R. Williams, 2013: Evaluation of cloud microphysics schemes in simulations of a winter storm using radar and radiometer measurements. *J. Geophys. Res. Atmos.*, **118**, 1401–1419. <https://doi.org/10.1002/jgrd.50115>.
- Hartigan, J. A., and M. A. Wong, 1979: AK-means clustering algorithm. *J. R. Stat. Soc.*, **28**, 100–108, doi:doi:10.2307/2346830. <https://www.jstor.org/stable/2346830>.
- Hendon, H. H., D. W. J. Thompson, and M. C. Wheeler, 2007: Australian rainfall and surface temperature variations associated with the Southern Hemisphere annular mode. *J. Clim.*, **20**, 2452–2467. <https://doi.org/10.1175/JCLI4134.1>.
- Henry, N. L., 2000: A Static Stability Index for Low-Topped Convection. *Weather Forecast.*, **15**, 246–254. [https://doi.org/10.1175/1520-0434\(2000\)015%3C0246:ASSIFL%3E2.0.CO;2](https://doi.org/10.1175/1520-0434(2000)015%3C0246:ASSIFL%3E2.0.CO;2).
- Hong, S.-Y., J. Dudhia, and S.-H. Chen, 2004: A Revised Approach to Ice Microphysical Processes for the Bulk Parameterization of Clouds and Precipitation. *Mon. Weather Rev.*, **132**, 103–120.
- , Y. Noh, and J. Dudhia, 2006: A New Vertical Diffusion Package with an Explicit Treatment of Entrainment Processes. *Mon. Weather Rev.*, **134**, 2318–2341. <http://journals.ametsoc.org/doi/abs/10.1175/MWR3199.1>.

- Houze, R. A., 2012: Orographic Effects on Precipitating Clouds. *Rev. Geophys.*, **50**, doi:10.1029/2011RG000365.
- Huang, Y., S. T. Siems, M. J. Manton, and G. Thompson, 2014: An Evaluation of WRF Simulations of Clouds over the Southern Ocean with A-Train Observations. *Mon. Weather Rev.*, **142**, 647–667, doi:10.1175/MWR-D-13-00128.1. <http://journals.ametsoc.org/doi/abs/10.1175/MWR-D-13-00128.1>.
- , T. Chubb, F. Sarmadi, S. T. Siems, M. J. Manton, C. N. Franklin, and E. Ebert, 2018: Evaluation of wintertime precipitation forecasts over the Australian Snowy Mountains. *Atmos. Res.*, **207**, 42–61. <https://doi.org/10.1016/j.atmosres.2018.02.017>.
- Hughes, M., A. Hall, and R. G. Fovell, 2009: Blocking in Areas of Complex Topography, and Its Influence on Rainfall Distribution. *J. Atmos. Sci.*, **66**, 508–518, doi:10.1175/2008JAS2689.1.
- Janjic, Z., K. Emanuel, and Z.-R. M., 2000: Comments on “Development and Evaluation of a Convection Scheme for Use in Climate Models.” *J. Atmos. Sci.*, **57**, 3686–3686. [https://doi.org/10.1175/1520-0469\(2000\)057%3C3686:CODAEO%3E2.0.CO;2](https://doi.org/10.1175/1520-0469(2000)057%3C3686:CODAEO%3E2.0.CO;2).
- Jiang, Q., 2003: Moist dynamics and orographic precipitation. *Tellus, Ser. A Dyn. Meteorol. Oceanogr.*, **55**, 301–316. <https://doi.org/10.1034/j.1600-0870.2003.00025.x>.
- Jones, D., W. Wang, and R. Fawcett, 2009: High-quality spatial climate data-sets for Australia. *Aust. Meteorol. Oceanogr. J.*, **58**, 233–248, doi:10.22499/2.5804.003.
- Klein, W. H., B. M. Lewis, and I. Enger, 1959: Objective prediction of five-day mean temperatures during winter. *J. Meteorol.*, **16**, 672–682. [https://doi.org/10.1175/1520-0469\(1959\)016%3C0672:OPOFDM%3E2.0.CO;2](https://doi.org/10.1175/1520-0469(1959)016%3C0672:OPOFDM%3E2.0.CO;2).
- Koch, S. E., M. Desjardins, and P. J. Kocin, 1983: An Interactive Barnes Objective Map Analysis Scheme for Use with Satellite and Conventional Data. *J. Clim. Appl. Meteorol.*, **22**, 1487–1503. <https://www.jstor.org/stable/26181170>.
- Landvogt, P. K., J. A. T. Bye, and T. P. Lane, 2008: An investigation of recent orographic precipitation events in northeast Victoria. *Aust. Meteorol. Mag.*, **57**, 235–247. <http://www.scopus.com/inward/record.url?eid=2-s2.61849139526&partnerID=tZOtx>.
- Liebscher, E., 2012: A Universal Selection Method in Linear Regression Models. *Open J. Stat.*, <http://www.scirp.org/journal/PaperDownload.aspx?DOI=10.4236/ojs.2012.22017>.
- Lin, Y., and B. a. Colle, 2009: The 4–5 December 2001 IMPROVE-2 Event: Observed

- Microphysics and Comparisons with the Weather Research and Forecasting Model. *Mon. Weather Rev.*, **137**, 1372–1392, doi:10.1175/2008MWR2653.1.
- Listowski, C., and T. Lachlan-Cope, 2017: The microphysics of clouds over the Antarctic Peninsula - Part 2: Modelling aspects within Polar WRF. *Atmos. Chem. Phys.*, **17**, 10195–10221, doi:10.5194/acp-17-10195-2017.
- Liu, C., K. Ikeda, G. Thompson, R. Rasmussen, and J. Dudhia, 2011: High-Resolution Simulations of Wintertime Precipitation in the Colorado Headwaters Region: Sensitivity to Physics Parameterizations. *Mon. Weather Rev.*, **139**, 3533–3553. <http://journals.ametsoc.org/doi/abs/10.1175/MWR-D-11-00009.1>.
- Long, A. B., and A. W. Huggins, 1992: Australian Winter Storms Experiment ( AWSE ) I: Supercooled Liquid Water and Precipitation-Enhancement Opportunities. **31**.
- Lu, L., and D. Hedlry, 2004: The impact of the 2002-03 drought on the economy and agricultural employment.
- Madadgar, S., and M. Hamid, 2014: Improved Bayesianmultimodeling: Integration of copulas and Bayesianmodel averaging. *J. Hydrol.*, **6**, 2108–2123, doi:10.1002/2012WR013085.Received.
- Manton, M. J., and L. Warren, 2011: A confirmatory snowfall enhancement project in the snowy mountains of Australia. Part II: Primary and associated analyses. *J. Appl. Meteorol. Climatol.*, **50**, 1448–1458, doi:10.1175/2011JAMC2660.1.
- Marshall, G. J., 2003: Trends in the Soutern Annular Mode from Observations and Reanalyses. *J. Clim.*, **16**, 4134–4143, doi:10.1175/1520-0442(2003)016<4134:TITSAM>2.0.CO;2.
- Mejia, J. F., M. Giordano, and E. Wilcox, 2018: Conditional summertime day-ahead solar irradiance forecast. *Sol. Energy*, **163**, 610–622, doi:10.1016/j.solener.2018.01.094. <https://doi.org/10.1016/j.solener.2018.01.094>.
- Meneghini, B., I. Simmonds, and I. N. Smith, 2007: Association between Australian rainfall and the Southern Annular Mode. *Int. J. Climatol.*, **27**, 109–121, doi:10.1002/joc. [http://cdiac.esd.ornl.gov/oceans/GLODAP/glodap\\_pdfs/Thermohaline.web.pdf](http://cdiac.esd.ornl.gov/oceans/GLODAP/glodap_pdfs/Thermohaline.web.pdf).
- Miao, Q., and B. Geerts, 2013: Airborne measurements of the impact of ground-based glaciogenic cloud seeding on orographic precipitation. *Adv. Atmos. Sci.*, **30**, 1025–1038, doi:10.1007/s00376-012-2128-2.
- Miglietta, M. M., and A. Buzzi, 2001: A numerical study of moist stratified flows over

- isolated topography. *Tellus A Dyn. Meteorol. Oceanogr.*, **53**, 481–499, doi:10.3402/tellusa.v53i4.12222.
- Milbrandt, J. A., and M. K. Yau, 2005: A Multimoment Bulk Microphysics Parameterization. Part I: Analysis of the Role of the Spectral Shape Parameter. *J. Atmos. Sci.*, **62**, 3051–3064, doi:10.1175/JAS3534.1. <http://journals.ametsoc.org/doi/abs/10.1175/JAS3534.1>.
- Milrad, S. M., K. Lombardo, E. H. Atallah, and J. R. Gyakum, 2017: Numerical Simulations of the 2013 Alberta Flood: Dynamics, Thermodynamics, and the Role of Orography. *Mon. Weather Rev.*, **145**, 3049–3072, doi:10.1175/MWR-D-16-0336.1. <http://journals.ametsoc.org/doi/10.1175/MWR-D-16-0336.1>.
- Mlawer, E. J., S. J. Taubman, P. D. Brown, M. J. Iacono, and S. A. Clough, 1997: Radiative transfer for inhomogeneous atmospheres: RRTM, a validated correlated-k model for the longwave. *J. Geophys. Res. Atmos.*, **102**, 16663–16682. <http://doi.wiley.com/10.1029/97JD00237>.
- Morrison, A. E., S. T. Siems, M. J. Manton, and A. Nazarov, 2010: A Modeling Case Study of Mixed-Phase Clouds over the Southern Ocean and Tasmania. *Mon. Weather Rev.*, **138**, 839–862.
- , S. T. Siems, and M. J. Manton, 2013: On a natural environment for glaciogenic cloud seeding. *J. Appl. Meteorol. Climatol.*, **52**, 1097–1104. <https://doi.org/10.1175/JAMC-D-12-0108.1>.
- Morrison, H., and J. A. Milbrandt, 2015: Parameterization of Cloud Microphysics Based on the Prediction of Bulk Ice Particle Properties. Part I: Scheme Description and Idealized Tests. *J. Atmos. Sci.*, **72**, 287–311. <http://journals.ametsoc.org/doi/10.1175/JAS-D-14-0065.1>.
- , J. A. Curry, M. D. Shupe, and P. Zuidema, 2005: A New Double-Moment Microphysics Parameterization for Application in Cloud and Climate Models. Part II: Single-Column Modeling of Arctic Clouds. *J. Atmos. Sci.*, **62**, 1678–1693. <http://journals.ametsoc.org/doi/abs/10.1175/JAS3447.1>.
- , G. Thompson, and V. Tatarskii, 2009: Impact of Cloud Microphysics on the Development of Trailing Stratiform Precipitation in a Simulated Squall Line: Comparison of One- and Two-Moment Schemes. *Mon. Weather Rev.*, **137**, 991–1007. <http://journals.ametsoc.org/doi/abs/10.1175/2008MWR2556.1>.

- Mossop, S. C., and J. Hallett, 1974: *Ice Crystal Concentration in Cumulus Clouds: Influence of the Drop Spectrum*. 632-634 pp. <http://www.jstor.org/stable/1739190>.
- Murphy, B. F., and B. Timbal, 2008: A review of recent climate variability and climate change in southeastern Australia. *Int. J. Climatol.*, **28**, 859–879. [http://cdiac.esd.ornl.gov/oceans/GLODAP/glodap\\_pdfs/Thermohaline.web.pdf](http://cdiac.esd.ornl.gov/oceans/GLODAP/glodap_pdfs/Thermohaline.web.pdf).
- Nicholls, N., 2005: Climate variability, climate change and the Australian snow season. *Aust. Meteorol. Mag.*, **54**, 177–185.
- , 2010: Local and remote causes of the southern Australian autumn-winter rainfall decline, 1958-2007. *Clim. Dyn.*, **34**, 835–845, doi:10.1007/s00382-009-0527-6.
- Nicholls, S. D., S. G. Decker, W.-K. Tao, S. E. Lang, J. J. Shi, and K. I. Mohr, 2017: Influence of bulk microphysics schemes upon Weather Research and Forecasting (WRF) version 3.6.1 nor'easter simulations. *Geosci. Model Dev.*, **10**, 1033–1049, doi:10.5194/gmd-10-1033-2017. <https://www.geosci-model-dev.net/10/1033/2017/>.
- Nicoloutsopoulos, D., 2005: Parametric and Bayesian non-parametric estimation of copulas. University College London, 1-132 pp.
- Osburn, L., T. Chubb, S. Siems, M. Manton, and A. D. Peace, 2016: Observations of Supercooled Liquid Water in Wintertime Alpine Storms in South Eastern Australia. *Atmos. Res.*, **169**, 345–356, doi:10.1016/j.atmosres.2015.10.007.
- Panziera, L., 2010: Orographic forcing, the key for heuristic nowcasting of rainfall in the Alps. ETH Zurich, 113 pp.
- Pieri, A. B., J. von Hardenberg, A. Parodi, and A. Provenzale, 2015: Sensitivity of Precipitation Statistics to Resolution, Microphysics, and Convective Parameterization: A Case Study with the High-Resolution WRF Climate Model over Europe. *J. Hydrometeorol.*, **16**, 1857–1872.
- Pierrehumbert, R. T., and B. Wyman, 1985: Upstream Effects of Mesoscale Mountains. *J. Atmos. Sci.*, **42**, 977–1003. [https://doi.org/10.1175/1520-0469\(1985\)042%3C0977:UEOMM%3E2.0.CO;2](https://doi.org/10.1175/1520-0469(1985)042%3C0977:UEOMM%3E2.0.CO;2).
- Pittock, J., and D. Connell, 2010: Australia demonstrates the planet's future: Water and climate in the Murray-Darling basin. *Int. J. Water Resour. Dev.*, **26**, 561–578.
- Pontoppidan, M., J. Reuder, S. Mayer, and E. W. Kolstad, 2017: Downscaling an intense precipitation event in complex terrain: the importance of high grid resolution. *Tellus A Dyn. Meteorol. Oceanogr.*, **69**, 1–15. <https://doi.org/10.1080/16000870.2016.1271561>.

- Pook, M. J., and T. Gibson, 1999: Atmospheric blocking and storm tracks during SOP-1 of the FROST Project. *Aust. Meteor. Mag.*, 51–60.
- , P. C. McIntosh, and G. A. Meyers, 2006: The synoptic decomposition of cool-season rainfall in the southeastern Australian cropping region. *J. Appl. Meteorol. Climatol.*, **45**, 1156–1170, doi:10.1175/JAM2394.1.
- Pope, M., C. Jakob, and M. J. Reeder, 2009a: Objective classification of tropical mesoscale convective systems. *J. Clim.*, **22**, 5797–5808, doi:10.1175/2009JCLI2777.1.
- , ——, and ——, 2009b: Regimes of the north Australian wet season. *J. Clim.*, **22**, 6699–6715, doi:10.1175/2009JCLI3057.1.
- Pruppacher, H. R., and J. D. Klett (1997), *Microphysics of Cloud and Precipitation*, Kluwer Academic, 954pp.
- Puri, K., and Coauthors, 2013: Implementation of the initial ACCESS numerical weather prediction system. *Journal South. Hemisph. Earth Syst. Sci.*, **63**, 265–284, doi:10.22499/2.6302.001. <http://www.bom.gov.au/jshess/docs/2013/puri.pdf>.
- Rasmussen, R., and Coauthors, 2011: High-resolution coupled climate runoff simulations of seasonal snowfall over Colorado: A process study of current and warmer climate. *J. Clim.*, **24**, 3015–3048, doi:10.1175/2010JCLI3985.1.
- Rauber, R. M., and L. O. Grant, 1987: Supercooled Liquid Water Structure of a Shallow Orographic Cloud System in Southern Utah. *J. Appl. Meteorol.*, **26**, 208–215.
- Reinecke, P. a., and D. R. Durran, 2008: Estimating Topographic Blocking Using a Froude Number When the Static Stability Is Nonuniform. *J. Atmos. Sci.*, **65**, 1035–1048, doi:10.1175/2007JAS2100.1.
- Richard, E., A. Buzzi, and G. Zangl, 2007: Quantitative precipitation forecasting in the Alps: The advances achieved by the Mesoscale Alpine Programme. *Q. J. R. ...*, **133**, 937–948. <https://doi.org/10.1002/qj.71> .
- Risbey, J. S., M. J. Pook, M. C. Wheeler, and H. H. Hendon, 2009: On the Remote Drivers of Rainfall Variability in Australia. *Mon. Weather Rev.*, **137**, 3233–3253. <https://doi.org/10.1175/2009MWR2861.1>.
- Roe, G. H., 2005: Orographic Precipitation. *Annu. Rev. Earth Planet. Sci.*, **33**, 645–671, doi:10.1146/annurev.earth.33.092203.122541.
- Rogers, D. C., and G. Vali, 1987: Ice Crystal Production by Mountain Surfaces. *J. Clim. Appl. Meteorol.*, **26**, 1152–1168, doi:10.1175/1520-

0450(1987)026<1152:ICPBMS>2.0.CO;2.

- Rögnvaldsson, Ó., J. W. Bao, and H. Ólafsson, 2007: Sensitivity simulations of orographic precipitation with MM5 and comparison with observations in Iceland during the Reykjanes Experiment. *Meteorol. Zeitschrift*, **16**, 87–98, doi:10.1127/0941-2948/2007/0181.
- Rossow, W. B., G. Tselioudis, A. Polak, and C. Jakob, 2005: Tropical climate described as a distribution of weather states indicated by distinct mesoscale cloud property mixtures. *Geophys. Res. Lett.*, **32**, 1–4, doi:10.1029/2005GL024584.
- Saji, N. H., B. N. Goswami, P. N. Vinayachandran, and T. Yamagata, 1999: A dipole mode in the tropical Indian ocean. *Nature*, **401**, 360–363, doi:10.1038/43855.
- Sarmadi, F., Y. Huang, S. T. Siems, and M. J. Manton, 2017: Characteristics of wintertime daily precipitation over the Australian Snowy Mountains. *J. Hydrometeorol.*, 2849–2867, doi:10.1175/JHM-D-17-0072.1.
- Schicker, I., P. Papazek, A. Kann, and Y. Wang, 2017: Short-range wind speed predictions for complex terrain using an interval-artificial neural network. *Energy Procedia*, **125**, 199–206. <http://dx.doi.org/10.1016/j.egypro.2017.08.182>.
- Schumacher, R. S., D. M. Schultz, and J. A. Knox, 2015: Influence of Terrain Resolution on Banded Convection in the Lee of the Rocky Mountains. *Mon. Weather Rev.*, **143**, 1399–1416. <http://journals.ametsoc.org/doi/10.1175/MWR-D-14-00255.1>.
- Schweizer, B., and E. F. Wolff, 1981: On Nonparametric Measures of Dependence for Random Variables. *Ann. Stat.*, **9**, 879–885. <http://www.jstor.org/stable/2240856>.
- Shafer, P. E., and H. E. Fuelberg, 2008: A Perfect Prognosis Scheme for Forecasting Warm-Season Lightning over Florida. *Mon. Weather Rev.*, **136**, 1817–1846. <http://journals.ametsoc.org/doi/abs/10.1175/2007MWR2222.1>.
- Sinclair, M. R., D. S. Wratt, R. D. Henderson, and W. R. Gray, 1997: Factors Affecting the Distribution and Spillover of Precipitation in the Southern Alps of New Zealand - A Case Study. *J. Appl. Meteorol.*, **36**, 428–442. [https://doi.org/10.1175/1520-0450\(1997\)036%3C0428:FATDAS%3E2.0.CO;2](https://doi.org/10.1175/1520-0450(1997)036%3C0428:FATDAS%3E2.0.CO;2).
- Skamarock, W. C., and J. B. Klemp, 2008: A time-split nonhydrostatic atmospheric model for weather research and forecasting applications. *J. Comput. Phys.*, **227**, 3465–3485. <https://doi.org/10.1016/j.jcp.2007.01.037>.
- Sklar, A., 1959: Fonctions de repartition à n dimensions et leurs marges. *Publ. Inst. Stat.*

- Univ. Paris, 8, 229–231.
- Smith, R. B., 1979: *The influence of mountains on the atmosphere*. 87-230 pp.
- , 1989: Hydrostatic Airflow over Mountains. *Adv. Geophys.*, **31**, 1–41, doi:10.1016/S0065-2687(08)60052-7.
- Smith, S. A., S. B. Vosper, and P. R. Field, 2015: Sensitivity of orographic precipitation enhancement to horizontal resolution in the operational Met Office Weather forecasts. *Meteorol. Appl.*, **22**, 14–24, doi:10.1002/met.1352.
- Sokol, Z., and D. Řezáčová, 2000: Improvement of local categorical precipitation forecasts from an NWP model by various statistical postprocessing methods. *Stud. Geophys. Geod.*, **44**, 38–56. <https://doi.org/10.1023/A:1022057807597>.
- Stoelinga, M. T., and Coauthors, 2003: Improvement of microphysical parameterization through observational verification experiment. *Bull. Am. Meteorol. Soc.*, **84**, 1807–1826, doi:10.1175/BAMS-84-12-1807.
- Storelvmo, T., C. Hoose, and P. Eriksson, 2011: Global modeling of mixed-phase clouds: The albedo and lifetime effects of aerosols. *J. Geophys. Res. Atmos.*, **116**, 1–13, doi:10.1029/2010JD014724.
- Taylor, K. E., 2001: Summarizing multiple aspects of model performance in a single diagram. *J. Geophys. Res. Atmos.*, **106**, 7183–7192, doi:10.1029/2000JD900719. <http://doi.wiley.com/10.1029/2000JD900719>.
- Theobald, A., H. McGowan, J. Speirs, and N. Callow, 2015: A synoptic classification of inflow-generating precipitation in the Snowy Mountains, Australia. *J. Appl. Meteorol. Climatol.*, **54**, 1713–1732. <https://doi.org/10.1175/JAMC-D-14-0278.1>.
- Thompson, G., P. R. Field, R. M. Rasmussen, and W. D. Hall, 2008: Explicit Forecasts of Winter Precipitation Using an Improved Bulk Microphysics Scheme. Part II: Implementation of a New Snow Parameterization. *Mon. Weather Rev.*, **136**, 5095–5115. <https://doi.org/10.1175/2008MWR2387.1>.
- Timbal, B., and W. Drosowsky, 2013: The relationship between the decline of Southeastern Australian rainfall and the strengthening of the subtropical ridge. *Int. J. Climatol.*, **33**, 1021–1034, doi:10.1002/joc.3492.
- Wang, G., and H. H. Hendon, 2007: Sensitivity of Australian rainfall to inter-El Niño variations. *J. Clim.*, **20**, 4211–4226, doi:10.1175/JCLI4228.1.
- Wang, Z., D. Belusic, Y. Huang, S. T. Siems, and M. J. Manton, 2016: Understanding

- orographic effects on surface observations at Macquarie Island. *J. Appl. Meteorol. Climatol.*, **55**, 2377–2395, doi:10.1175/JAMC-D-15-0305.1.
- Watson, C. D., and T. Lane, 2012: Sensitivities of orographic precipitation to terrain geometry in idealized simulations. 2012.
- , and T. P. Lane, 2014: Further Sensitivities of Orographic Precipitation to Terrain Geometry and Upstream Conditions in Idealized Simulations. *J. Atmos. Sci.*, **69**, 3068–3088, doi:10.1175/JAS-D-11-0198.1.
- Van Weverberg, K., and Coauthors, 2013: The Role of Cloud Microphysics Parameterization in the Simulation of Mesoscale Convective System Clouds and Precipitation in the Tropical Western Pacific. *J. Atmos. Sci.*, **70**, 1104–1128. <http://journals.ametsoc.org/doi/abs/10.1175/JAS-D-12-0104.1>.
- White, B., E. Gryspeerdt, P. Stier, H. Morrison, G. Thompson, and Z. Kipling, 2017: Uncertainty from the choice of microphysics scheme in convection-permitting models significantly exceeds aerosol effects. *Atmos. Chem. Phys.*, **17**, 12145–12175. <https://doi.org/10.5194/acp-17-12145-2017>.
- Williams, A. A. J., and R. C. Stone, 2008: An assessment of relationships between the Australian subtropical ridge, rainfall variability, and high-latitude circulation patterns. *Int. J. Climatol.*, **29**, 691–709.
- Wilson, D. R., and S. P. Ballard, 1999: A microphysically based precipitation scheme for the UK Meteorological Office Unified Model. *Q. J. R. Meteorol. Soc.*, **125**, 1607–1636, doi:10.1256/smsqj.55706.
- Wilson, L., M. J. Manton, and S. T. Siems, 2013: Relationship between rainfall and weather regimes in south-eastern Queensland, Australia. *Int. J. Climatol.*, **33**, 979–991, doi:10.1002/joc.3484.
- Woods, C. P., M. T. Stoelinga, J. D. Locatelli, and P. V. Hobbs, 2005: Microphysical Processes and Synergistic Interaction between Frontal and Orographic Forcing of Precipitation during the 13 December 2001 IMPROVE-2 Event over the Oregon Cascades. *J. Atmos. Sci.*, **62**, 3493–3519. <https://doi.org/10.1175/JAS3550.1>.
- Worboys, G. L., and R. B. Good, 2011: *Caring For Our Australian Alps Catchments: Summary Report For Policy Makers*. 64 pp. <http://eprints3.cipd.esrc.unimelb.edu.au/547/>.
- Wright, W., 1989: A synoptic climatological classification of winter precipitation in

Victoria. Aust. Meteor. Mag., 37, 217–229

WWRP/WGNE, 2008: *Recommendations for the Verification and Intercomparison of QPFs and PQPFs from Operational NWP Models*. Geneva, Switzerland, 37 pp.  
[https://www.wmo.int/pages/prog/arep/wwrp/new/documents/WWRP2009\\_1.pdf](https://www.wmo.int/pages/prog/arep/wwrp/new/documents/WWRP2009_1.pdf).